Evaluation of Topography, Slopes, Illumination and Surface Roughness of Landing Sites near the Lunar South Pole using Laser Altimetry from the Lunar Reconnaissance Orbiter

vorgelegt von
Diplom-Ingenieur
Philipp Andreas Gläser
geb. in Ludwigsburg

Von der Fakultät VI - Planen Bauen Umwelt
der Technischen Universität Berlin
zur Erlangung des akademischen Grades
Doktor der Ingenieurwissenschaften
Dr.Ing.

genehmigte Dissertation

Promotionsausschuss:

Vorsitzender: Prof. Dr. Frank Flechtner
Gutachter: Prof. Dr. phil. nat. Jürgen Oberst
Gutachter: Dr. Gregory Neumann
Gutachter: Prof. Dr. Harald Hiesinger

Tag der wissenschaftlichen Aussprache: 26 November 2014

Berlin 2014

D83

Institute
Of
Planetary Research

Department for Geodesy
and Geoinformation
Science

PhD Thesis

Evaluation of Topography, Slopes, Illumination and Surface Roughness of Landing Sites near the Lunar South Pole using Laser Altimetry from the Lunar Reconnaissance Orbiter

Supervised by
Prof. Dr. phil. nat. Jürgen Oberst

—

Released by
Dipl. Ing. Philipp Andreas Gläser
Berlin, October 06, 2014

Eidesstattliche Erklärung

Ich erkläre an Eides Statt, dass ich meine Doktorarbeit mit dem Titel

"Evaluation of Topography, Slopes, Illumination and Surface Roughness of Landing Sites near the Lunar South Pole using Laser Altimetry from the Lunar Reconnaissance Orbiter"

selbständig und ohne Benutzung anderer als der angegebenen Hilfsmittel angefertigt habe und dass ich alle Stellen, die ich wörtlich oder sinngemäß aus Veröffentlichungen entnommen habe, als solche kenntlich gemacht habe.

Die Arbeit hat bisher in gleicher oder ähnlicher Form oder auszugsweise noch keiner Prüfungsbehörde vorgelegen.

Berlin, den 06.10.2014

(Philipp Gläser)

Acknowledgment

A big thank you to

Jürgen Oberst for giving me the opportunity to work in the field of planetary research and his consistent support and trust throughout the last five years, which enabled me to conduct research in a way that works best for me. Thank you for all the proof-reading you have done for me.

Isabel Haase for all her help, motivation, fun conference travels and also for sharing an office with me for so long. Best office mate ever!

Konrad Willner for his constant support on all levels, whether it was technical, motivational or scientific. A special thanks for proof-reading this thesis and making it readable.

Frank Scholten for his mentoring, guidance and many phone calls helping me solve problems. Toytanic forever!

All my TU Berlin colleagues for scientific exchange, fun lunches, travels, chats and good times. Anastasios Margonis, Ender Tasdelen, Steffi Burmeister, Sven Weisbrich for fruitful discussions. Special thanks to Rosi Kunkel for helping me out many times.

My DLR colleagues Hauke Hussmann, Sven Bauer, Marita Wählisch, Klaus-Dieter Matz, Alex Stark and Thomas Roatsch for support and helpful discussions.

Dave Smith, Maria Zuber, Mark Torrence, Kopal Jha, Erwan Mazarico, Dandan Mao, Frank Lemoine and the whole LOLA team for giving me the chance to work with them, and moreover for making my stay at Goddard Space Flight Center so unforgettable. Also to Mark Robinson and the LROC team for amazing data and fun conferences.
Special thanks to Gregory Neumann for his outstanding support, scientific guidance and dealing with all kinds of bureaucracy in order to help me.

The German Research Foundation DFG and the German Space Agency DLR for funding this work.

The best family in the world! Many claim to have the best, but I actually do. To my parents for encouraging me to pursue my dreams and reach for the stars..literally. Thanks for buying me that Aldi telescope that changed my life. To my siblings Stefanie and Dennis for being the mirror and compass in my life.

Martin Kempa, Armin Wolff, Şevket Dirican and Matias Majica for being the best friends one can ask for. Thanks for your constant support.

Monique Witt for everything. Thank you for all the fun you bring into my life and the incredible support I get from you every day. Thanks for proof-reading my thesis so patiently. You are my favorite!

Per aspera ad astra

Zusammenfassung

Diese Arbeit beschäftigt sich mit der Auswertung aktueller, wissenschaftlicher Messungen des Lunar Reconnaissance Orbiter (LRO), einer Mondsonde der National Aeronautics and Space Administration (NASA). Seit Juni 2009 vermisst LRO die Mondoberfläche kontinuierlich und in höchster Präzision. Diese Messungen, speziell die des LRO Lunar Orbiter Laser Altimeter (LOLA), sind in dieser Arbeit detailliert untersucht und ausgewertet worden, aber auch Bilddaten der LRO Lunar Reconnaissance Orbiter Camera (LROC), genauer der Narrow Angle Camera (NAC), wurden in die Auswertung mit einbezogen. Digitale Geländemodelle, die aus Laserdaten gerechnet wurden, weisen typischerweise Artefakte auf, die neben Ausreißern eindeutig auf Lageungenauigkeiten zwischen Laserspuren zurückzuführen sind. Dominant sind diese Artefakte insbesondere bei hoch aufgelösten Geländemodellen. Zur Beseitigung von relativen Lageungenauigkeiten zwischen einzelnen Laserspuren ist in dieser Arbeit ein Algortihmus zur Co-Registrierung entwickelt worden. Dazu wird ein NAC Geländemodell mit allen LOLA Laserspuren, die das Gebiet kreuzen co-registriert, was zu individuellen Translationsparametern für jede einzelne Laserspur führt. Standardabweichungen der Höhenresiduen zwischen NAC und LOLA nach der Co-Registrierung von bis ∼20 cm werden dabei erreicht.

Auf Grundlage des resultierenden, ausgeglichenen Geländemodells werden sekundäre Datenprodukte wie Hangneigungs- und Rauhigkeitskarten erstellt. Zwei unterschiedliche Methoden zur Ableitung von Rauhigkeitskarten aus Laserdaten werden vorgestellt, wobei eine Methode sich auf Standardabweichungen von Regressionsebenen und die andere sich auf die Analyse von Laserpulsbreiten stützt. Während die erste Methode zuverlässige Werte auf globaler sowie lokaler Ebene liefert, zeigt letztere Methode verwertbare Ergebnisse auf globaler Ebene wobei die Ergebnisse auf lokalen, hoch aufgelösten Gebieten sorgfältiger analysiert werden müssen. Das ist auf zahlreiche Faktoren, wie Rauschen und thermaler Einfluss, zurückzuführen, die in dieser Arbeit angesprochen werden, jedoch nicht abschließend behandelt werden konnten.

Eine detaillierte Beschreibung der Beleuchtungsverhältnisse des lunaren Südpols mit besonderer Betrachtung dreier potentieller Landeplätze, wird vorgestellt. Zwei dieser Landeplätze befinden sich auf dem Rand des Shackleton-Kraters und eine weitere auf einer Hügelkette, die den de Gerlache-Krater und den Shackleton-Krater verbindet, im weiteren Connecting Ridge genannt. Beleuchtungsverhältnisse wurden auf Bodenniveau aber auch 2 m und 10 m über der Mondoberfläche gerechnet und werden über einen Zeitraum von 1 Jahr sowie 19 Jahre untersucht. Der Zeitraum von 19 Jahren wurde untersucht, um den lunaren Präzessionszyklus von 18.6 Jahren abzudecken. Die Berechnungen über einen Zeitraum von 1 Jahr wurden angestellt, um mit Ergebnissen von vorherigen Veröffentlichungen verglichen werden zu können. Im Hinblick auf lange Beleuchtungsphasen, z.B. 10 m über der Mondoberfläche, stellt sich Connecting Ridge mit einer totalen Beleuchtung von bis zu 95.66% über einen Zeitraum von 19 Jahren als idealer Landeplatz heraus. Kontinuierliche Beleuchtungsperioden von bis zu 262.42 Tage, bei einer maximalen Dunkelpe-

riode von nur 3.17 Tage, machen diesen Landeplatz für Lander- oder Rovermissionen mit Solarpanelen äußerst attraktiv.

Auch die Sichtbarkeit von den Landeplätzen zu zehn European Space Agency (ESA) Radiostationen auf der Erde werden untersucht, wodurch gezeigt werden konnte, dass selbst für Landeplätze auf der Rückseite des Mondes nur relativ kurze Perioden (ca. 2 Wochen) in Funklöchern überbrückt werden müssen.

Abstract

This work deals with the evaluation of current scientific data collected by National Aeronautics and Space Administration (NASA)'s Lunar Reconnaissance Orbiter (LRO) mission. Since June 2009 LRO has been continuously surveying the lunar surface with high precision. The main focus is placed on data retrieved by the LRO Lunar Orbiter Laser Altimeter (LOLA) but also images acquired by the LRO Lunar Reconnaissance Orbiter Camera (LROC), more specifically the Narrow Angle Camera (NAC), will be discussed briefly. Digital Terrain Models (DTMs) derived from laser data typically show artifacts, which in addition to common outliers, are clearly induced by positional inaccuracies between tracks. These artifacts, especially in high resolution DTMs, become a prominent feature. A co-registration algorithm is introduced, which was developed in the course of this work and corrects the relative position between single laser tracks. For this purpose a NAC DTM is co-registered with all intersecting LOLA tracks allowing for a precise adjustment of each individual laser track position. A standard deviation of $\sim$20 cm in height residuals between LOLA and NAC profiles can be attained with this co-registration technique.

Secondary data products such as slope and roughness maps are created on the basis of the resulting, adjusted LOLA DTM. Two independent methods for roughness calculations based on laser data are introduced, one method is based on standard deviation values of plane fits and the other method is based on the analysis of the laser pulse width. While the former method delivers reliable results on a local and global scale, the latter shows reasonable results on a global scale but needs to be carefully analyzed on a local, high-resolution scale. Various effects on the laser pulse measurement such as noise and thermal influence are addressed in this work but are not further investigated.

A detailed description of illumination conditions at the lunar south pole is given, in particular of three possible landing sites. Two of these sites are located on the rim of Shackleton Crater and the third lies on a ridge connecting the de Gerlache and Shackleton craters, referred to as the Connecting Ridge. Illumination conditions at surface level, 2 m and 10 m above ground were simulated for a 1-year and a 19-year period. The 19-year time period was chosen to cover the lunar precessional cycle of 18.6 years and the 1-year period was chosen in accordance with previous studies. Connecting Ridge was found to be an ideal site concerning long illumination periods. For example, total illumination of up to 95.66% during the considered 19-year period is found 10 m above ground. This particular landing site has up to 262.42 continuous days of sunlight with a maximum of only 3.17 days of continuous darkness, making it an attractive location for future landing devices relying on solar power.

Visibility of Earth from each considered landing site to ten European Space Agency (ESA) tracking stations was simulated, proving that even landing sites on the farside of the Moon only have to overcome short periods (about 2 weeks) in radio dead zones.

Contents

List of Figures

List of Tables

1 Motivation

The goal of this work is to evaluate potential landing sites at the lunar south pole using data from the Lunar Orbiter Laser Altimeter (LOLA), an instrument on-board the Lunar Reconnaissance Orbiter (LRO) mission. Landing sites on the lunar south pole are of great interest due to the fact that locations in permanent shadow exist next to locations receiving almost constant illumination. A location in almost constant sunlight allows for continuous electric power supply for a lander or rover equipped with solar panels. In many Permanently Shadowed Areas (PSAs) water ice can be found and could be investigated from a landing site nearby.

Extensive shadowed areas at the poles exist due to the small tilt of the lunar axis of 1.54° with respect to the ecliptic plane. This circumstance heavily complicates the derivation of topographic maps when relying on imaging systems such as the Lunar Reconnaissance Orbiter Camera (LROC). In PSAs it is generally impossible to derive image-based data products at all. LOLA, however, can scan illuminated and shadowed terrain alike which is why it will be the main data source for this work and the ideal instrument for investigating landing sites at the lunar poles.

One main aspect is the derivation of illumination conditions for specific potential landing sites on the Moon. A large south polar Digital Terrain Model (DTM) with high resolution is required to meet the needs for this task. In a simulation of illumination conditions, not only the orientation of the Moon with respect to the Sun but more importantly the exact topography must be known. Small errors in derived surface morphology can lead to significant changes in received illumination. New techniques need to be developed to geometrically adjust LOLA DTMs to improve absolute and relative coordinate knowledge. Consequently, illumination conditions can only be simulated on such an adjusted high-resolution DTM.

Also the visibility of the Earth is a driving factor for landing site selection owing to communication purposes to a ground station. All past lunar surface missions landed on the nearside and close to the equator of the Moon. Constant communication links to the Earth are achieved for those landing sites. In this work, however, communication periods for landing sites on the near- and the farside close to the lunar south pole are investigated.

The structural design of landers and rovers launching for a lunar surface mission need to be prepared for the expected morphology of the landing site. In particular, the expected slope of the terrain is a crucial factor for engineering the legs of a lander or the wheels of a rover. Moreover, the roughness at the landing site, e.g. the expected rock sizes and abundance, is important to plan the rover's and lander's structural design. Maps to infer estimates for the aforementioned parameters will need to be generated in this work.

The following outline provides the chronological steps taken to attain the results found in this work. First, a general overview of the Moon is given including dynamics and topography. Then, past and future lunar missions, especially missions carrying laser

altimeters and the Apollo missions are introduced. Further the LRO mission is presented followed by a more in-depth description of the LOLA instrument and data processing. Subsequently, Narrow Angle Camera (NAC), the Wide Angle Camera (WAC) as well as DTM processing are briefly described.

Chapter 6 presents methods developed and implemented in the course of this work. The careful analysis of LOLA data is the most crucial step because LOLA data products will serve as the foundation for further calculations. Co-registration of LOLA and NAC data in section 6.1 is central to this work. Here, a technique to derive adjusted, high resolution LOLA DTMs is described and an example of the workflow is given. All subsequent steps will depend on the resulting DTM. In section 6.2 the horizon method is presented, which is used to derive illumination conditions for the lunar south pole. The technique is described and followed by an example. A similar section follows, calculating the times when a direct line-of-sight from a lunar landing site to Earth-based European Space Agency (ESA) radio telescopes is available. The last section in Chapter 6, presents the techniques used in this work to infer slope and roughness values from LOLA data.

In Chapter 7 all results are presented, which are retrieved by applying the aforementioned techniques. A summary of the insights gained throughout this work and an outlook for future work are given in the conclusions chapter.

2 Introduction

In this work potential lunar landing sites near the south pole are investigated in terms of illumination conditions, direct communication possibilities to Earth, slope and surface roughness. For simulations of illumination conditions over specific time periods in the future, a precise surface model is required. Further, the topography surrounding the investigated landing site also needs to be known in order to identify time periods for direct communication possibilities to Earth. Lastly, slope and roughness maps are created on basis of the single tracks composing the surface models. Due to the fact that large shadowed areas exist at the lunar poles, DTMs derived from stereo images heavily suffer from data gaps in these areas. Since measurements from active instruments, like LOLA, are independent from the actual illumination condition and hence are also available for shadowed areas, LOLA was chosen as the main data source in this study. However, after creating high-resolution LOLA DTMs it turned out that they could not be used as is. Small lateral and vertical offsets between single tracks create artifacts in the DTMs that can not be neglected. The foundation and key development of this study is the derivation of an adjusted, south polar LOLA DTM. For this purpose a co-registration technique was developed to adjust the single LOLA tracks to each other by comparing them to a NAC DTM. As described earlier, the resulting adjusted LOLA DTM serves as an input for the derivation of illumination conditions and direct communication possibilities to Earth. The single adjusted LOLA tracks are used to infer slope and roughness values.

The study is divided into two main parts, the 'Data Evaluation' and the 'Results' part. This way is chosen since the various methods introduced in the 'Data Evaluation' part are based on each other and shall be displayed next to each other. Only brief examples are given after each method section to clarify its purpose and to keep the readers' attention on the evolution of the developed tools. The reader will find the 'Results' part in the same chronological composition as the 'Data Evaluation' part and will by then already understand "why was done what in which order" and can hopefully enjoy it better.

A summary of all methods and results is given in Fig. 1. All results are displayed in blue squares and the corresponding methods are shown in black writing next to the arrows. Data sources and products like single LOLA tracks and the NAC DTM were available for this work.

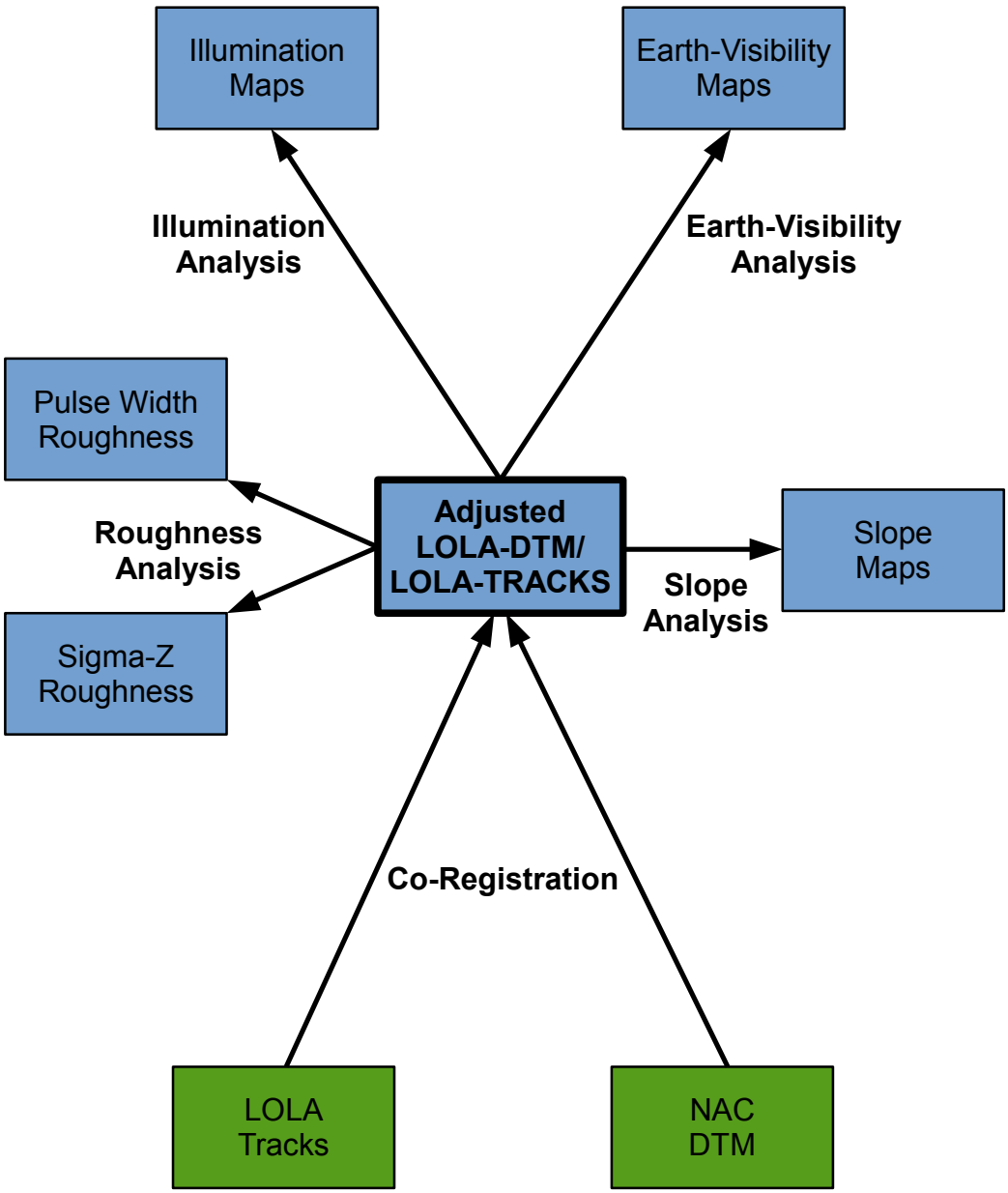

Figure 1: This figure gives an overview of the developed tools and the results obtained in this work. The blue squares represent the various results and the text next to the arrows represent methods developed in the course of this study. The arrows show the dependencies between results and data sources. The green squares represent data sources that were available or provided. It can be seen, that the adjusted LOLA DTM is the central part of this work.

3 The Moon

The Moon is the Earth's only natural satellite and is also the brightest celestial body in the night sky. The subject of our curiosity and imagination, the Moon, has driven humankind to reach beyond the Earth and explore other celestial bodies. Many cults, religions, calenders and traditions were and still are related to the Moon, which gives it a special place in human history. *Dies lunae* is the day dedicated to the Roman goddess of the Moon, Luna. In many languages the translation for 'Moon Day' can be found in our weekday calender: in English as Monday, in Spanish as lunes, in German as Montag, and in Italian as lunedi. The Islamic calender, for example, is purely based on the lunar cycle whereas the Jewish calender is a so called lunisolar calender. In the lunisolar calender, for instance, a year consists of 354 days based on the lunar cycle. However, a 13th month (30 days) is introduced seven times within the 19-year Metonic cycle (see 3.2). This takes place in leap years (3, 6, 8, 11, 14, 17 and 19) to align the calender to the solar cycle. Other prominent examples for lunisolar calenders are the traditional Chinese and Hindu calender, mainly used to determine the dates of traditional feasts.

3.1 Origin

The origin and evolution of the Moon is still being discussed. Different theories exist, that attempt to explain the origin of the Moon. One theory states, that the Earth and the Moon originated from the so called proto-Earth, a giant fluid planet. Centrifugal forces separated material from the outer layer of the proto-Earth forming a satellite system of which one was the Moon. All other satellites have been lost due to the decrease of gravity or explosive destruction by increasing the fluid pressure inside while consolidating rapidly from the outer layer [Marakushev and Chaplygin, 2002]. Another theory states that the Moon has evolved independently and has then been captured by Earth. Geochemical and geophysical details of the lunar lower mantle as well as the distribution of elements and their isotopes can be explained by this theory [Schmitt, 2000].

The most accepted theory, however, is that the Moon formed 4.5 Ga ago as the result of a giant impact on Earth by a Mars-sized body called Theia. This theory best explains the differentiation of the Moon into a small inner core ($\sim$280 km [Williams et al., 2014]) and a large silicate mantle and the formation of a global magma ocean due to a hot formation of the Moon. The ancient highlands of the Moon then formed by crystallization of the magma ocean [Spohn, 2000]. As well the almost identical isotopic composition of the Moon and the Earth is explained by the giant impact theory [Jacobson et al., 2014]. Exploring the Moon with either robotic sample return or manned missions will help to further adapt, exclude or rethink existing theories.

3.2 Lunar orbit and rotation

The Moon's orbit has always been a matter of interest for humans. The first recorded attempts to predict the lunar orbit dates back to the Babylonians in ∼500 BC. Their interests in establishing calendars, predicting new and full moons and eclipses lead to the discovery of the Metonic cycle, which is the 19 years cyclic relation of the lunar and the solar cycle. Aristotle, Hipparchus, Ptolemy and Ibn al-Shatir were some of the important astronomers in the history of defining the lunar orbit, who believed in a geocentric model where the Sun, Moon and all planets orbit around the Earth. Copernicus was the first to reject the geocentric model. His theory of the heliocentric model where the Sun is in the center and all planets and moons orbit around it was published in his book *De revolutionibus orbium coelestium* in 1543. Tycho Brahe combined the geocentric and heliocentric models in which the Earth is in the center and the Sun and the Moon orbit around it but all other planets orbit around the Sun. His assistant Johannes Kepler, however, firmly believed in the Copernican, heliocentric model. Kepler formulated his three famous laws in his book *Astronomia Nova* in 1609 describing the motion of planets.

- The orbit of every planet is an ellipse with the Sun at one of the two foci.
- A line joining a planet and the Sun sweeps out equal areas during equal intervals of time.
- The square of the orbital period of a planet is directly proportional to the cube of the semi-major axis of its orbit.

Although they are just valid for zero-mass objects orbiting the Sun, they still accurately describe planetary motions. Kepler also accomplished the important step to describe planetary motion in elliptical instead of circular orbits.

With the postulation of the universal law of gravitation,

$$F = G\frac{m_1 m_2}{r^2}$$

in which G is the gravitational constant, m_1, m_2 are the masses of the two bodies and r is the distance between them, it was Isaac Newton who could explain Kepler's laws of motion.

- First law: The velocity of a body remains constant unless the body is acted upon by an external force.
- Second law: The acceleration a of a body is parallel and directly proportional to the net force F and inversely proportional to the mass m, F = ma.
- Third law: The mutual forces of action and reaction between two bodies are equal, opposite and collinear.

His work was published in his book *Philosophiae Naturalis Principia Mathematica* in 1686 and is considered one of the most important works in science. Airy, Cowell and Brown observed and refined the lunar orbit in the 19th and early 20th century. Numerical integration of the lunar orbit became feasible with the invention of computers. Since the Apollo era the lunar ephemerides are precisely observed by means of Lunar Laser Ranging (LLR) (see Chapter 5.2.4) and are made available to the lunar science community via Internet by e.g. the Jet Propulsion Laboratory (JPL) [Folkner et al., 2009, 2014], the Institut de Mécanique Céleste et de Calcul des Éphémérides (IMCCE) [Fienga et al., 2010] and the Institute for Applied Astronomy of the Russian Academy of Sciences (IAA RAS) [Pitjeva, 2010]. The ephemerides for the solar system 'DE421' [Folkner et al., 2009], for instance, are provided by JPL in the form of a so-called kernel which can be read and interpreted by SPICE (see appendix A).

Important physical parameters of the Moon are summarized in Table 1.

Table 1: Physical parameters of the moon [Seidelmann et al., 2007], [U. S. Naval Observatory and Royal Greenwich Observatory, 2000], [Cox, 2000].

Parameter	**Value**
Mean radius	1737.4 ± 1 km
Equatorial radius a	1738.1 km
Polar radius b	1736.0 km
Flattening $f = (a - b)/a$	0.0012
GM	4900 km^3/s^2
Semimajor axis	384400 km
Perigee	363300 km
Apogee	405500 km
Revolution period	27.3217 days
Synodic period	29.53 days
Obliquity	6.68°
Orbit eccentricity	0.0549
Inclination to ecliptic	5.145°
Inclination to Earth's equator	18.28° - 28.58°
Recession rate from Earth	3.8 cm/yr

3.2.1 Cassini's laws and states

Tidal torques are responsible for the synchronization of the rotational period and orbit mean motion. After synchronization the obliquity is often reduced to zero, where the spin axis and the orbit normal vector are parallel. A nonzero obliquity can only persist if the planet is in a so-called Cassini State [Winn and Holman, 2005].

Giovanni Domenico Cassini published his three famous empirical laws on the Moon's rotational motion in 1693 [Colombo, 1966; Peale, 1969]:

- Law 1 - The lunar rotation rate is synchronous with the mean siderial period of its orbit around the Earth
- Law 2 - The inclination of the Moon's equator to the ecliptic is constant and approximately $\sim 1.5°$
- Law 3 - The lunar spin axis and normal vectors to the ecliptic and the orbit plane remain coplanar

Further there are two Cassini states, which are related to the third Cassini law:

- State 1 - The spin axis and the normal vector of the orbit plane are on the same side of the ecliptic normal vector
- State 2 - The spin axis and the normal vector of the orbit plane are on opposite sides of the ecliptic normal vector

The Moon is in Cassini State 2, where the ecliptic normal vector is always between the spin and the orbit normal vector. Owing to this fact, both, the spin axis and the normal to the orbital plane precess around the ecliptic normal vector with the same period of ~ 18.6 years in retrograde sense. The small inclination of $\sim 1.5°$ of the Moon's equator to the ecliptic allows for extreme illumination conditions near the lunar poles, which will be discussed in Chapter 6.2.

3.2.2 Libration

Due to tidal locking, one hemisphere of the Moon is always facing Earth, the so called nearside. Almost all moons of the solar system are in synchronous rotation, where the rotation around their axes takes about the same time it takes to orbit the central body. Lunar libration, however, permits an observer on Earth to see $\sim 59\%$ of the Moon as it rocks back and forth. This effect is caused by optical and physical libration. Physical libration of the Moon is the departure of the lunar rotational motion from the one described by the laws of Cassini.

There are three different types of optical libration:

- Libration in longitude describes a sideways rotation of up to $7.9°$ and is mainly caused by the eccentricity of the Moon's orbit. The angular velocity of the Moon in its orbit changes due to this elliptical orbit while the rotation of the Moon is constant. The lunar angular velocity is at its maximum at the pericenter, the closest approach, whereas it is at its minimum at the apocenter, the farthest excursion. Hence, the apparent rotation of the Moon seems slower when it is closer and faster when it is farther from an Earth-based observer.

- Libration in latitude is caused by the inclination of the Moon's rotational axis and the orbital plane. The angle is 6.68° and causes an effect similar to the seasons on Earth. It allows us to see the Moon's north- and south pole at different time periods.

- Parallactic or diurnal libration is an effect caused by the Earth's rotation. From moonrise to moonset the Earth rotates 180° and permits an observer to see the Moon from different angles. The angular difference amounts to 1°.

Physical libration is the actual movement due to tidal forces acting on the Moon caused by the gravitation of the Earth. This effect is rather small compared to optical libration and lies in the order of a few arc-seconds [Rambaux and Williams, 2011].

3.2.3 Lunar phases

An observer looking at the Moon can see different lunar phases which are the result of observing the illuminated part of the Moon from different viewing geometries (see Fig. 2). In general, half of the Moon is always illuminated but depending on the orbital constellation of the Earth, Sun and Moon an observer can see all stages from new moon to full moon. New moon, therefore, always appears when the Moon is located between the Sun and the Earth and full moon occurs when the Earth is between the Sun and the Moon. When full moon coincides with the ascending or descending node of the lunar orbit a lunar eclipse occurs. Consequently, when the new moon coincides with the ascending or descending node of the lunar orbit a solar eclipse occurs.

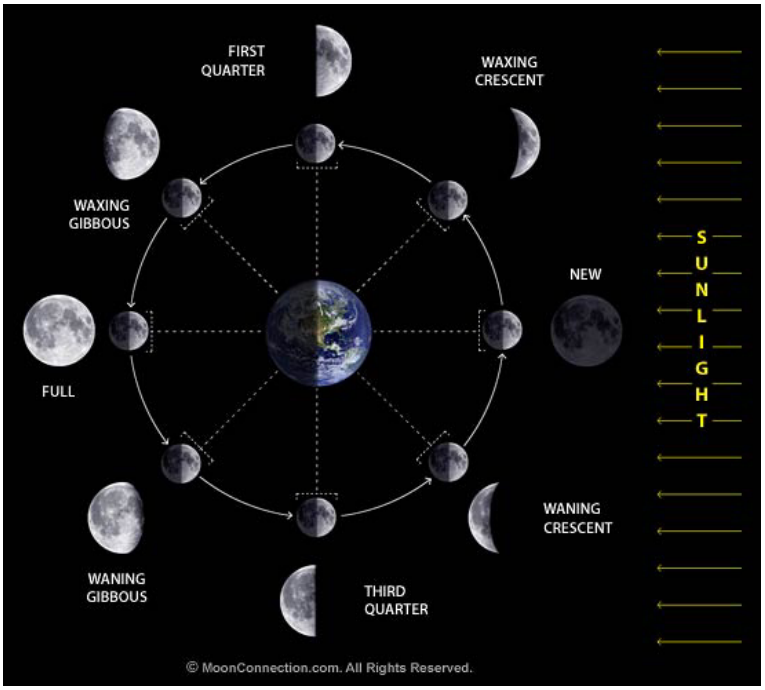

Figure 2: Lunar phases over the course of one Moon day. ©MoonConnection.com

3.3 Lunar reference systems

There are two lunar reference systems mainly used in planetary science. The Principal Axis (PA) reference system is a lunar body-fixed rotating frame whose axes are defined by the principal axes of the lunar moment of inertia matrix [LRO Project, 2008; Williams et al., 2008]. The PA system is mostly used for dynamical studies of the lunar gravity field but also as the reference system for lunar laser ranging [LRO Project, 2008]. Laser measurements from the Earth to the Moon are fundamental for the realization of such a physical reference system. In total there are five laser reflectors on the lunar surface, three of which were left by the astronauts of the Apollo missions 11, 14, 15 and two of which that were mounted on the Lunokhod rovers 1 and 2.

Another reference system is the Mean Earth/Polar Axis (ME) or Mean Earth/Mean Rotation Axis reference system. Here, the prime meridian, X axis, is defined by the mean direction towards Earth and the Z axis is the mean rotational pole. Y complements the right-handed system. The Moon, however, is not a synchronously rotating triaxial ellipsoid, and therefore the PA and ME rotation axes do not coincide. At the lunar surface, the axes of the two systems differ by about 1 km [LRO Project, 2008].

There is a constant three angle rotation matrix relating the ME to the PA system. Assume M is a Cartesian vector in the ME frame and P in the PA frame, then the transformation in both directions are given by

$$M = R_x(-0.30")R_y(-78.56")R_z(-67.92")P \quad (1)$$

$$P = R_z(67.92")R_y(78.56")R_z(0.30")M \quad (2)$$

R stands for a rotation matrix and R_x, R_y, R_z denote rotations about the x, y, z-axis. Since the rotations are dependent on the gravity field used, equations 1-2 only apply using the DE421 ephemeris.

3.4 Surface Morphology

The appearance of the lunar topography (Fig. 3) on the nearside is quite different to the one on the farside. The nearside's most prominent features are maria (Latin for seas, singular is mare), which early astronomers believed to be lunar seas. Maria are huge plains that contain dark, basaltic material erupted from volcanic activities. As a result of the iron-rich composition of this material it is less reflective than other parts of the lunar surface and appears relatively darker. Famous lunar mare on the nearside are Imbrium, Serenitatis, Tranquillitatis, Crisium, Fecunditatis, Nectaris, Nubium, Humorum and Oceanus Procellarum. Together with a few prominent impact craters like, Tycho, Copernicus, Aristarchus and Kepler these are the main topographic features. Due to resurfacing processes by lava flows, the nearside appears rather smooth in comparison to the farside, although both hemispheres are believed to have received a similar number of impacts. This is explained by the thinner crust of the nearside, allowing volcanoes to

erupt and fill large impact craters and basins. These lava flows covered older craters and let the nearside appear smoother. The difference in crustal thickness can be explained by the Earthshine on the Moon of the hot, post-giant impact Earth, preferentially depositing crust-forming refractories on the cooler farside [Roy et al., 2014]. Garrick-Bethell et al. [2010] suggested that the primordial shape of the Moon was symmetric and controlled by early tidal heating, which influenced the global crustal thickness pattern. The apparent lack of a nearside bulge manifested as a result of large-scale internal mass reorganizations due to density differences between late crystallizing products of the magma ocean. Jutzi and Asphaug [2011] suggested that a moonlet, left over from the giant impact that created the Moon, slowly accreted onto the farside, resulting in higher topography and thickened crust.

As a result the topography of the farside is very distinct to the one of the nearside, and appears much rougher. There are just a few and small maria, namely Mare Moscoviense, Ingenii, Orientale and Mare Australe which is shared with the nearside. The farside, however, is laced with impact craters and appears much rougher. With the South Pole Aitken basin, the farside is home of the largest, deepest and oldest impact basin of the Moon and one of the largest in the solar system. The lowest elevation on the Moon is -9.117 km and is located within the South Pole Aitken basin at 187.5074°E, 70.360°S in the Antoniadi crater and the highest elevation of 10.7834 km is located just north of South Pole Aitken at 201.378°E, 5.401°N [Smith et al., 2010b].

The entire Moon is covered by a debris blanket, the so-called regolith, which is produced by meteorite impacts and the interaction of the surface with the solar wind. Regolith is rocky material ranging from dust to meter-size rocks, whereas it is mainly composed by very fine dust. Due to the intense cratering on the farside, the thickness of the regolith layer can reach up to a few kilometers, referred to as mega-regolith.

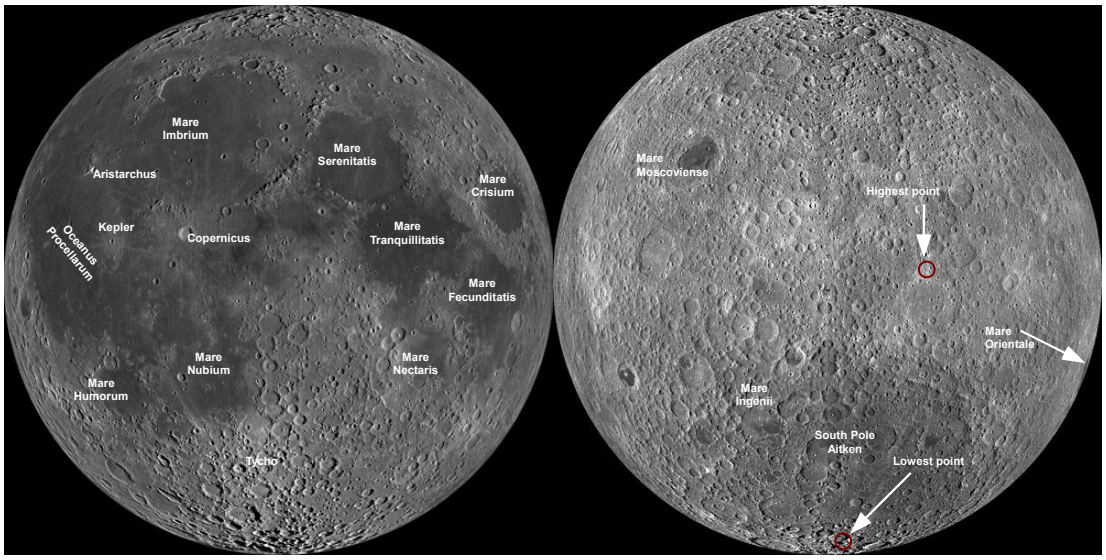

Figure 3: Lunar near- (left) and farside (right) with maria, craters, lowest and highest elevation. These mosaics contain over 15,000 LROC WAC images (see Chapter 5.3) acquired between November 2009 and February 2011. ©[NASA/GSFC/ASU]

4 Missions to the Moon

The very first attempt to fly to the Moon was made by the United States of America (USA) on August 17, 1958. The Pioneer 0 mission, however, exploded just 77 seconds after liftoff. A month later the Soviet Union launched its first mission to the Moon called Luna 1958A, which also exploded just after liftoff. The years of the Cold War saw many attempts to reach the Moon on both sides, the Soviet Union and the USA. It took seven attempts all together until the Soviet Union made a first flyby at the Moon with Luna 1 in early 1959. Although it was planned to be a lunar impactor, it was the first spacecraft to reach the Moon's orbit.

The USA performed the first successful flyby just two months later with Pioneer 4. The Soviet Luna spacecrafts became a complete success story: Luna 2 was the first spacecraft to impact on the Moon, Luna 3 took the first images of the farside of the Moon, Luna 9 was the first spacecraft to make a controlled landing on the surface and Luna 10 was the first spacecraft to go into orbit at the Moon. Although the USA had very successful programs like Ranger and Surveyor, the Soviet Union was always a step ahead.

Information on any planetary mission can be obtained from NASA's National Space Science Data Center (NSSDC) master catalog[1].

4.1 Apollo Missions

On May 25, 1961 President John F. Kennedy gave his famous speech in front of Congress:

> "I believe that this nation should commit itself to achieving the goal, before this decade is out, of landing a man on the moon and returning him safely to the Earth. No single space project in this period will be more impressive to mankind, or more important for the long-range exploration of space; and none will be so difficult or expensive to accomplish."

To accomplish this goal, the largest rocket ever built was developed by the rocket engineer team around Wernher von Braun.

Saturn V Between the two world wars a small group of German engineers around Wernher von Braun dreamt of reaching high altitudes and even the lunar orbit by experimenting with liquid-propellant rockets. After Von Brauns' dissertation in Berlin his *Aggregat 2* already reached 2200 m altitude. With the outbreak of World War II he became the director of the *Heeresversuchsanstalt Peenemünde* where his group was provided facilities and money for rocket testing and launching. Here, the *Aggregat 4* was developed, also called *V2*, which was the first rocket containing gyros for automatically stabilizing the trajectory. After the war many scientists went to the USA in the so called *Operation Overcast*, later *Operation Paperclip*. Von Braun and his team then continued the work of the deceased rocket pioneer Robert Goddard in White Sands, New Mexico. In 1959 he started working for NASA and became the director of the Marshall Space Flight Center (MSFC) which lead to the development of the Saturn V rocket. The Saturn V is one of the strongest rockets ever build and is the only one capable to have brought a total of 24 human beings to our Moon (Apollo 8,10-12,14-17 with each 3 astronauts).

[1] `http://nssdc.gsfc.nasa.gov/nmc/`

Apollo 8 At Christmas 1968 Apollo 8 was launched and became the first manned mission to the Moon, bringing Frank Bormann, James Lovell and William Anders as the first humans into a lunar orbit. The USA was on the brink of surpassing the Soviets' success of the last decade with Apollo 10, which tested procedures for the first lunar landing.

Apollo 11 Apollo 11, the first manned mission to our Moon set out to land on the Moon and return to Earth. On July 16, 1969 Neil Armstrong, Edwin 'Buzz' Aldrin (see Fig. 4) and Michael Collins were launched by a Saturn V rocket from Kennedy Space Center to the Moon. Three days later they reached the lunar orbit and after one day in orbit Commander Armstrong and Lunar Module Pilot Aldrin descended on board the Lunar Module *Eagle*. Command Module Pilot Michael Collins remained in orbit in the Command/Service Module *Columbia*. Due to computer problems at the lunar descent Armstrong switched to semi-automatic control and landed with just about 25 seconds of fuel left in Mare Tranquillitatis (see Fig. 3). On July 21, 1969, Armstrong started his descent from the Lunar Module saying his famous line:

> "That's one small step for man, one giant leap for mankind."

Figure 4: The bootprints of Edwin Aldrin in July 1969 marks one of the first steps on the Moon. ©NASA

The astronauts carried out some Extra-Vehicular Activity (EVA) including setting up the American flag, collecting 21.5 kg of rock samples for return, finding the best way to walk in low gravity wearing space suits, deploying a passive seismograph and a laser ranging reflector. The laser ranging reflector remains a valuable experiment up to date, helping to precisely determine the lunar orbit with Earth-based laser stations [Williams et al., 2013].

Apollo 12 - 17 All following Apollo missions were carried out successfully, except for Apollo 13, where an explosion of one of the two oxygen tanks in the Service Module forced the crew to return before landing on the Moon, all other five Apollo missions were a full success. Similar to the astronauts of Apollo 11, the crews of Apollo 14 and 15 also placed laser ranging reflectors on the lunar surface. Together with the two Soviet missions Luna 17 and Luna 21, which placed the laser reflector carrying Lunokhod 1 and Lunokhod 2 rovers on the Moon, the total number of precisely known surface points amounts to five. Apollo 15, 16 and 17 all used a Lunar Roving Vehicle (LRV), a small car which extended the mobility of the astronauts and helped carry equipment. A laser altimeter was mounted on the Command/Service Modules of these later missions, which took distance measurements to the lunar surface. Apollo 17 astronaut Harrison 'Jack' Schmitt was the only scientist ever selected for an Apollo mission and together with Eugene Cernan also the last human being to have walked on the lunar surface.

4.2 Lunar Missions with laser altimeters

Apollo 15, 16, 17 On the last three Apollo missions, 15-17, the Apollo Lunar Mapping Camera System was installed in the Scientific Instrumentation Module (SIM) which is part of the Command/Service Module. It consisted of two cameras, a mapping and a stellar camera, two film canisters and the first spaceborn laser altimeter [Kaula et al., 1973, 1974] (see Fig. 5). The altimeters flown on the Apollo missions were ruby flash lamp lasers with a beam width of 300 μrad resulting in a footprint of approximately 300 m in diameter. The along-track distance from point to point varied from 30 to 43 km owing to a firing rate of 16 to 32 seconds. The ranging accuracy was $\pm$2 m [Smith et al., 1997]. All together

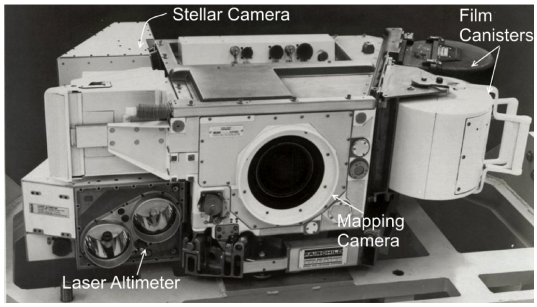

Figure 5: Apollo Lunar Mapping Camera System. ©NASA

7080 range measurements were taken and 5631 were used to study the lunar topography [Bills and Ferrari, 1977]. The vertical accuracy of $\sim$400 m was due to uncertainties in the spacecraft trajectory [Kaula et al., 1974]. Since the Command/Service Module operated from near-equatorial orbits, all laser tracks acquired from the Apollo missions only cover regions close to the equator. The tracks are shown in Fig. 6 [Smith et al., 1997].

Clementine In 1994 Clementine became the first U.S. mission to return to the Moon since the Apollo missions. From February to March it mapped the Moon in unprecedented

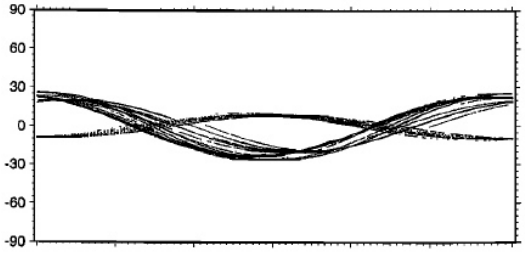

Figure 6: Laser tracks obtained from the Apollo 15, 16 and 17 mission.

detail. Among other the scientific instruments, Clementine was equipped with a laser altimeter called the Laser Image Detection and Ranging (LIDAR) system. LIDAR was a Neodymium-Doped Yttrium Aluminum Garnet (Nd:YAG) source emitting a laser beam with a wavelength of 1064 nm. The beam width of <500 μrad allowed for footprints of ∼200 m at the periselene (∼400 km). Approximately 650,000 shots were fired of which 72,300 shots could be geolocated with a vertical accuracy of ∼100 m whereas the ranging accuracy of the LIDAR was ∼40 m [Smith et al., 1997]. LIDAR was a Nd:YAG source emitting a laser beam with a wavelength of 1064 nm. The beam width of <500 μrad allowed for footprints of ∼200 m at the periselene (∼400 km). Approximately 650,000 shots were fired of which 72,300 shots could be geolocated with a vertical accuracy of ∼100 m whereas the ranging accuracy of the LIDAR was ∼40 m [Smith et al., 1997]. Fig. 7 shows a color coded, shaded, global topographic map of the Moon from gridded LIDAR tracks.

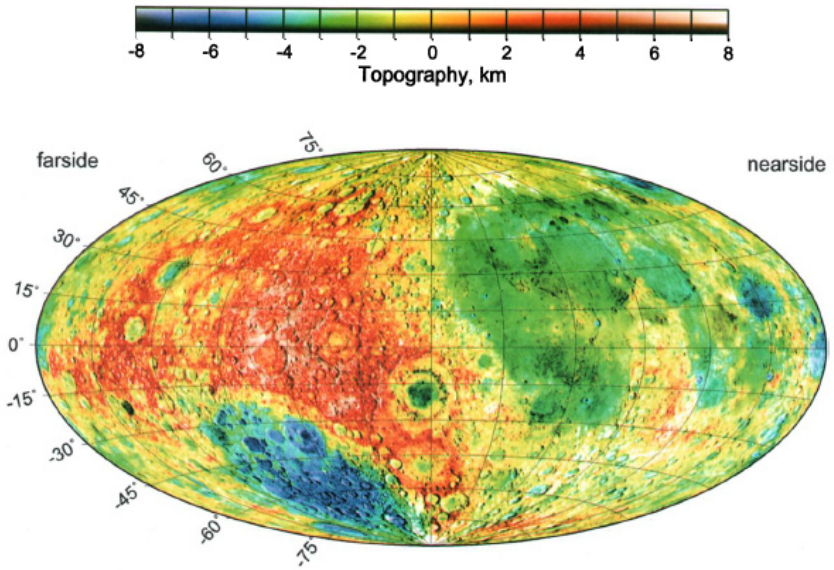

Figure 7: The topography of the Moon generated from Clementine laser tracks shown in a Hammer equal-area projection [Smith et al., 1997]. The farside is located on the left hemisphere and the nearside on the right.

Kaguya (Selene-1) The Japanese lunar satellite Kaguya (Selene-1) was launched on September 14, 2007 from the Tanegashima Space Center. Kaguya carried a Laser Altimeter (LALT) which was designed to map the Moon from the nominal orbit altitude of 100 km [Araki et al., 2009](see Fig. 8). LALT fired at 1 Hz resulting in an along-track spacing of 1.6 km from spot to spot, with a spot size on the lunar surface of 40 m. The radial topographic error is estimated to be 4 m and the horizontal topographic error is estimated to be 77 m [Araki et al., 2009; Bussey et al., 2009]. On February 1, 2009 Kaguya descended to a 50 km orbit and on April 16, 2009 to a 10-30 km orbit before impacting on the south-east of the nearside on June 10, 2009 (80.4°E, 65.5°S[2]). At the end of the mission more than 20 million points had been obtained by LALT [Sasaki et al., 2012].

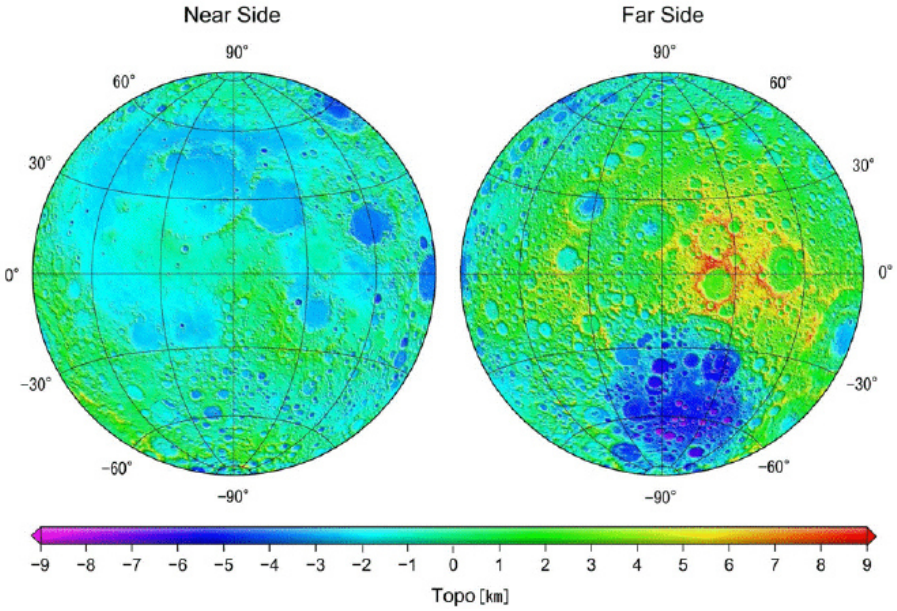

Figure 8: Lambert equal area projection topographic map of the near- and farside of the Moon using LALT data [Araki et al., 2009].

Chang'E-1 The Chang'E-1 mission was China's first lunar exploration mission. It was launched on October 24, 2007 from the Xichang Satellite Launch Center and was placed in a 200 km orbit around the Moon. The Laser Altimeter (LAM) had a spot size of 120 m, a ranging accuracy of ∼5 m and a repetition rate of 1 Hz. The repetition rate leads to a 1.4 km along-track spacing assuming 100% laser ranging probability [Ping et al., 2009]. In total, LAM recorded over 8 million ranges during the mission. The Chang'E-1 Lunar Topography Model s01 (CLTM-s01), a 360th degree and order spherical harmonic expansion of the Moon, is derived from approximately 3 million range measurements (see Fig. 9). On March 1, 2009, at the end of the mission Chang'E-1 impacted on the Moon [Huang et al., 2010].

[2] http://www.kaguya.jaxa.jp/en/communication/KAGUYA_Lunar_Impact_e.htm

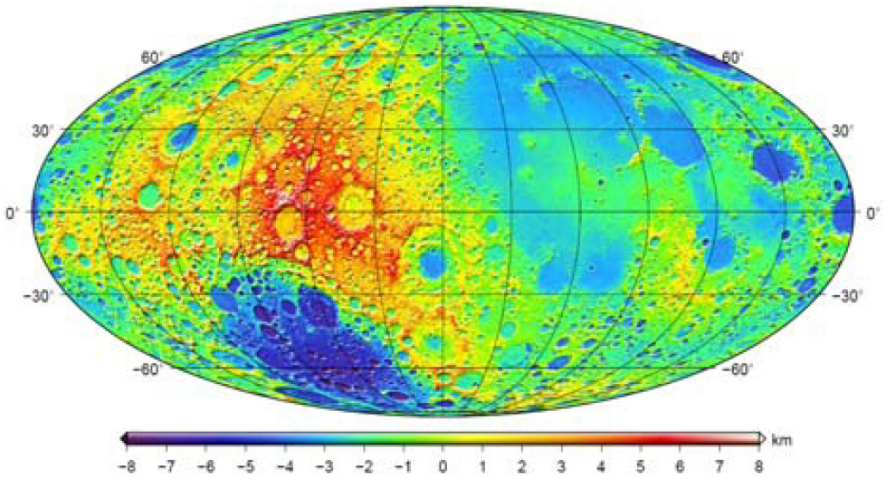

Figure 9: CLTM-s01, 360th degree and order spherical harmonic expansion of the topography of the Moon [Huang et al., 2010].

Chandrayaan 1 Chandrayaan 1 (in Hindi *Chandra* means Moon and *Yaan* means ship) was the first planetary mission from the Indian Space Research Organization (ISRO). On October 22, 2008 it was launched from Shriharikota Space Center in India. The primary scientific objective of this mission was to improve the understanding of the origin and evolution of the Moon. Among a variety of scientific payload the Terrain Mapping Camera (TMC) and the Lunar Laser Ranging Instrument (LLRI) provided topographic maps with a ground resolution of up to 5 m [Goswami and Annadurai, 2009; Goswami et al., 2006]. LLRI is a 10 mJ Nd-YAG laser emitting 5 ns laser pulses at 10 Hz pulse repetition rate and 1064 nm wavelength [Goswami and Annadurai, 2009; Goswami et al., 2006]. The reflected laser pulse from the lunar surface is received by a 20 cm Ritchey-Chrétien telescope and focused on a silicon Avalanche Photodiode (APD). The Lunar poles were mapped by LLRI and are shown in Fig. 10.

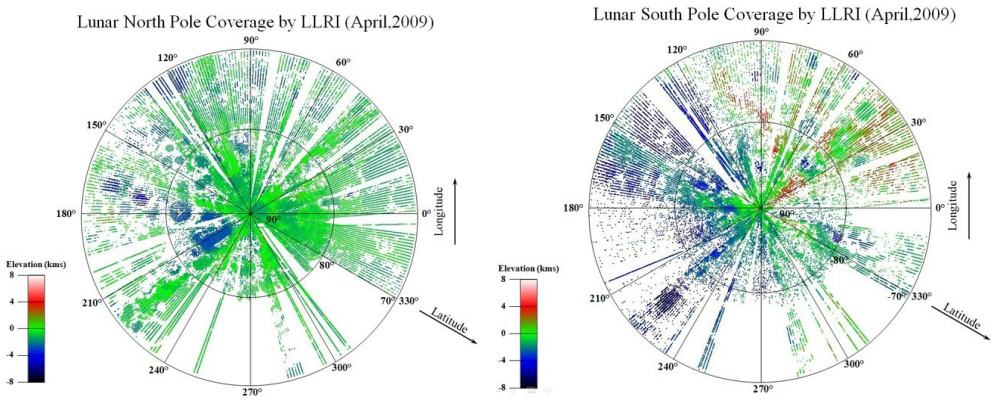

Figure 10: The topography of the lunar poles mapped by LLRI of the Chandrayaan-1 spacecraft. ©ISRO

4.3 Recent and future Lunar Missions

Chang'E-2 Just about one and a half years after the end of the Chang'E-1 mission China launched its second probe, Chang'E-2, on October 1, 2010. The design of the spacecraft is very similar to the first probe, due to the fact that it was built as a backup to Chang'E-1. Better cameras and a lower orbit of only 100 km in contrast to 200 km for Chang'E-1 made it possible to map the Moon in a much higher resolution. One of the main goals of this mission was to assist the landing site selection process for the next mission, Chang'E-3. On June 8, 2011 the spacecraft left the lunar orbit and headed for L2 of the Earth-Sun system, one of the five Lagrangian points in the Earth-Sun system. Here, the gravitational pull of the Earth and the Sun acting on a third body with negligible mass acts in such a way that the third object is relatively stationary with respect to the Earth and Sun. On April 15, 2012 Chang'E-2 departed from L2 for the asteroid 4179 Toutatis to make a flyby, which was successfully performed on December 13, 2012.

Chang'E-3 Chang'E-3 launched on December 2, 2013, and reached lunar orbit on December 4, 2013. After landing on December 14, 2013 the rover, named Yutu, descended from its lander platform. Chang'E-3 is the first Chinese lander and will help the Chinese Space Program to gather experience in soft landing techniques as well as rover surface operations. It is the first spacecraft Luna 24 in 1976 to land softly on the lunar surface (Luna 24 was an unmanned Soviet return sample mission). Sinus Iridium (44.1° N, 31.5° W) was chosen as the landing site for this mission, which is closely located to the former Russian landing site of Lunokhod 1 (Lunokhod 1 was the first rover on another planet).

Chang'E-4 and Chang'E-5 With 3 missions to the Moon in just 6 years, China's ambitious lunar exploration is planning for another 2 missions in the near future. Chang'E-4 is a backup spacecraft for Chang'E-3 and is intended to launch in 2015 and Chang'E-5 is expected to land on the Moon in 2020. Its purpose is to collect lunar soil and rocks and return it to Earth. This will be China's first sample return mission and help pave the way for future exploration mission, especially for a planned manned lunar mission until 2025.

Chandrayaan 2 The Indian space agency ISRO is planning to go back to the Moon in 2016. After the orbiter mission of Chandrayaan 1, the mission scenario for Chandrayaan 2 will not only contain an orbiter but also a landing unit equipped with a rover. Its purpose is to carry out chemical analysis of lunar rocks. The lander was originally planned to be designed by the Russian Federal Space Agency (ROSCOSMOS) [Mitrofanov et al., 2011]. Due to production delays for the lander, however, ISRO decided to carry out the mission on its own.

Selene-2 Selene-2 will be the follow-up mission of Kaguya (Selene-1). It will consist of a relay satellite, a lander and a rover and is intended to land near the south pole of the

Moon. One of the main goals of this mission will be the testing of landing technology. The launch is planned to be around 2017.

International Lunar Network The International Lunar Network (ILN) will be realized by joint efforts of several countries. Each node will have at least two tasks, such as seismic sensing, carrying a laser retro-reflector or heat flow sensing. The first two nodes ILN-1 and ILN-2 are scheduled to launch in 2018.

Luna-Glob, Lunar-Resurs, Luna-Grunt Ambitious plans to revisit the Moon with a series of missions were laid out by ROSCOSMOS. The first mission is Luna-Glob (Luna-25), consisting of an orbiter and a lander, however, current plans indicate that the Luna-Glob lander will launch in 2016 and the Luna-Glob orbiter will launch 2018 as an independent mission. Luna-Resurs 0 (Luna-26), was a planned landing mission, which carried the aforementioned Indian mini-rover [Mitrofanov et al., 2011]. Current plans call for a polar orbiting spacecraft, providing communications relay capabilities for missions to follow. The launch is scheduled for 2018 [Mitrofanov et al., 2014]. Luna-Resurs 1 (Luna-27) is planned to be a larger lander than Luna-Glob with enhanced payload capabilities, for instance a drilling element to take samples of the lunar sub-surface of down to two meters; the expected launch date is in 2019 [Mitrofanov et al., 2014]. Landing sites near the lunar south pole are being discussed. The Luna-Grunt-1 and Luna-Grunt-2 missions are intended to be launched in 2020 and 2021. The first lander will deploy a long-range rover, which is capable to drive long distances, collects and stores lunar samples. Once the second lander will have landed in the vicinity of Luna-Grunt-1, the rover will upload the samples in it and the return stage of Luna-Grunt-2 will return them to the Earth.

Google Lunar X Prize The Google Lunar X Prize (GLXP)[3] was initiated by Google as an international, competitive prize over US$30 million. The first team, which requires to be funded privately by at least 90%, that lands safely on the lunar surface and manages to travel 500 m with its rover, sends videos, images and data back to Earth will win the competition. Currently 26 teams worldwide compete on winning this endeavor.

ESA Lunar Lander The ESA Lunar Lander was planned as an unmanned precursor mission to future human exploration, which was put on hold in December, 2012. The designated landing site areas were chosen to be locations receiving long illumination periods near the lunar south pole. Parts of this study contributed scientifically to the characterization of these landing sites.

[3] http://www.googlelunarxprize.org/

5 LRO - Lunar Reconnaissance Orbiter

In January 2004, the former President of the United States, George W. Bush, announced the new *Vision for Space Exploration* Program [NASA, 2004].

> "...Our third goal is to return to the moon by 2020, as the launching point for missions beyond. Beginning no later than 2008, we will send a series of robotic missions to the lunar surface to research and prepare for future human exploration. Using the Crew Exploration Vehicle, we will undertake extended human missions to the moon as early as 2015, with the goal of living and working there for increasingly extended periods. Eugene Cernan, who is with us today – the last man to set foot on the lunar surface – said this as he left: "We leave as we came, and God willing as we shall return, with peace and hope for all mankind." America will make those words come true. Returning to the moon is an important step for our space program. Establishing an extended human presence on the moon could vastly reduce the costs of further space exploration, making possible ever more ambitious missions. Lifting heavy spacecraft and fuel out of the Earth's gravity is expensive. Spacecraft assembled and provisioned on the moon could escape its far lower gravity using far less energy, and thus, far less cost. Also, the moon is home to abundant resources. Its soil contains raw materials that might be harvested and processed into rocket fuel or breathable air. We can use our time on the moon to develop and test new approaches and technologies and systems that will allow us to function in other, more challenging environments. The moon is a logical step toward further progress and achievement..."

The required steps to achieve the new goals for *The President's Vision for US Space Exploration* (January 2004) were elaborated in the NASA response document *Vision For Space Exploration* (February 2004).

- Undertake lunar exploration activities to enable sustained human and robotic exploration of Mars and more distant destinations in the solar system
- Starting no later than 2008, initiate a series of robotic missions to the Moon to prepare for and support future human exploration activities
- Conduct the first extended human expedition to the lunar surface as early as 2015, but no later than the year 2020
- Use lunar exploration activities to further science, and to develop and test new approaches, technologies, and systems, including use of lunar and other space resources, to support sustained human space exploration to Mars and other destinations

NASA released an Announcement of Opportunity (AO) listing a set of high priority measurements which are to be carried out by LRO [Chin et al., 2007]. Topics that are related to this works' goal to precisely map potential landing sites at the lunar south pole are shown in bold letters:

- Characterization of the deep space radiation environment in lunar orbit, including neutron albedo, especially at energies in excess of 10 MeV, as well as:
  - Characterization of biological effects caused by exposure to the lunar orbital radiation environment
  - Characterization of changes in the properties of multifunctional radiation shielding materials caused by extended exposure to the lunar orbital environment
- **Geodetic lunar global topography (at landing-site relevant scales)**
- High spatial resolution hydrogen mapping of the Moon's surface
- Temperature mapping of the Moon's polar shadowed regions
- Landform-scale imaging of lunar surfaces in permanently shadowed regions
- Identification of putative deposits of appreciable near-surface water ice in the Moon's polar cold traps
- **Assessment of meter and smaller-scale features to facilitate safety analysis for potential lunar landing sites**
- **Characterization of the illumination environment at the Moon's polar regions at relevant temporal scales (i.e., in terms of hours)**

NASA's Lunar Precursor Robotic Program (LPRP) was initiated to execute a series of robotic missions to the Moon. The Lunar Reconnaissance Orbiter is the first mission in this series.

In total six scientific instruments and one technology demonstration were selected (see Fig. 11). The instruments include the Cosmic Ray Telescope for the Effects of Radiation (CRaTER), the Diviner Lunar Radiometer Experiment (DLRE), the Lunar Exploration Neutron Detector (LEND), the Lyman-Alpha Mapping Project (LAMP). The instrument central to this study is the Lunar Orbiter Laser Altimeter (LOLA) and secondly the Lunar Reconnaissance Orbiter Camera (LROC). The Mini Radio Frequency (Mini-RF) was added as the technology demonstration package.

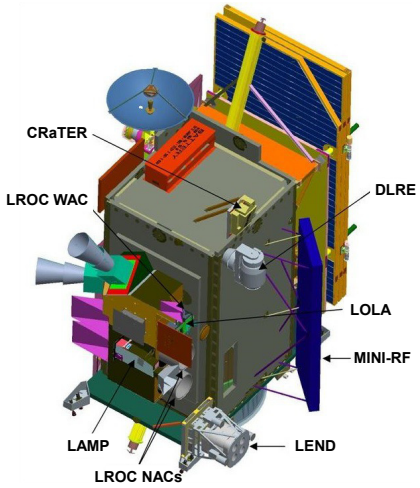

Figure 11: Design concept of LRO, showing all instruments. ©NASA

5.1 Mission overview

LRO was set to launch from Cape Canaveral in October 2008 [Chin et al., 2007] but was postponed to June 18, 2009 [Tooley et al., 2010]. LRO's launch window was mainly driven by the seasonal lighting of the lunar poles which limited the possible launch window to 2-3 day periods every two weeks. To investigate whether there are PSAs or permanently lit regions around the poles the spacecraft orbit had to be orientated such that it was at 0° beta-Sun angle during the lunar solstice periods. After four and a half days LRO reached the vicinity of the Moon and successfully executed a Lunar Orbit Insertion (LOI) maneuver which resulted in a low-maintenance, elliptical, quasi-frozen 30 x 216 km orbit. This event marked the beginning of the 60 days Commissioning Orbit (CO) phase where instruments were turned on and tested. On September 15, 2009 LRO transitioned to its Nominal Exploration Mission (NO) orbit, a 50 km polar mapping orbit. A year later on September 16, 2010 the Science Mission (SM) started but the orbit remained the same [Tooley et al., 2010]. After two years, LRO was again placed in a ∼200 x 30 km polar orbit with the periselene near the lunar south pole. This mission phase is called First Extended Science Mission (ESM1) and will end in September 2014, when LRO will start its Second Extended Science Mission (ESM2) [Keller et al., 2014]. In this low-maintenance orbit LRO's fuel reserve would last for another 11 years [Keller et al., 2014].

5.2 LOLA - Lunar Orbiter Laser Altimeter

The Lunar Orbiter Laser Altimeter (LOLA) is one of the six scientific instruments on LRO which was designed to globally map the Moon's topography at a high resolution and help identify possible landing sites for future robotic and human exploration. Before LOLA, the topography was not known precisely enough to ensure safe landing on any arbitrary point on the Moon except at the already visited Apollo landing sites [Smith et al., 2010a]. A list summarizing the objectives of LOLA is given by Chin et al. [2007]. All topics addressed

in this study are shown in bold letters:

1. **Global geodetic lunar topography**
2. **Characterize polar region illumination**
3. **Image permanently shadowed regions**
4. **Contribute to the assessment of meter-scale features to facilitate landing-site selection**
5. Identify surface polar ice, if present

5.2.1 Basic concept of laser altimetry

Space flown laser altimeters are designed to measure distances from a spacecraft to the surface of a planetary body, e.g. from a 50 km orbit around the Moon for LOLA and from 400 km orbit for the Mars Orbiter Laser Altimeter (MOLA). By continuously ranging to the planet at e.g. 10 Hz (10 measurements per second in the case of MOLA), thousands to billions of laser shots can be acquired over a mission life time. These measurements can be interpolated to a DTM, locally or globally, and serve as a source for further investigations. DTMs are necessary for a variety of scientific interests, e.g. calculating illumination conditions at specific times [Gläser et al., 2014; Mazarico et al., 2011a], deriving gravity fields from topography [Shi et al., 2012], mobility of rovers and landing site selection [De Rosa et al., 2012; Golombek et al., 2003a] etc.

A laser altimeter consists of a transmitter and a receiver, both of which point toward the planet's surface (see Fig. 12). The transmitter is the laser itself, sending pulsed

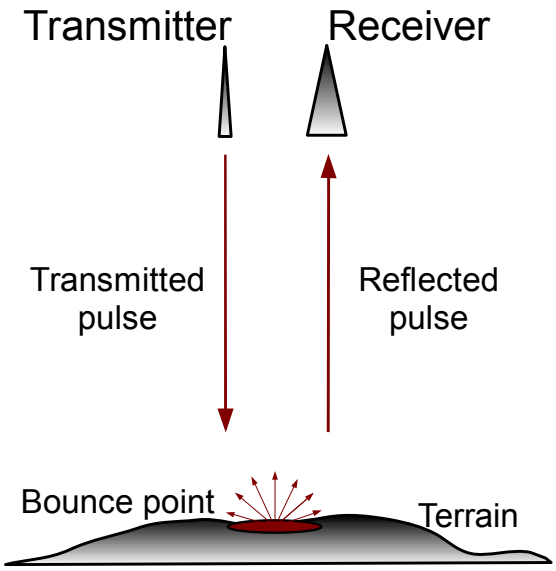

Figure 12: Basic concept of distance measurement with laser altimeters.

laser beams towards the observed surface. The receiver is a telescope where the reflected laser pulse is received and detected. When a laser pulse is emitted, a small fraction is redirected onto a detector, which triggers the start-time. The laser pulse travels to the surface, is reflected by it and a small fraction is received back at the telescope. The pulse is again focused onto a detector which triggers the stop-time. Distances between the spacecraft and the planet are usually well known from the predicted navigation orbits (see Chpapter 5.4). The receiving detectors, therefore, only trigger a distance measurement if the received pulse falls within this predefined range gate window, which is computed from the distance from the spacecraft to the planet (see Fig. 13). The distance measurement is only valid if an also predefined threshold level is exceeded (see Fig. 13). A threshold level ensures, that noise events do not cause a false distance measurement.

Distance measurements are, therefore, achieved by sending out a laser pulse and measuring its Time Of Flight (TOF) until it is received back at the receiver telescope. The TOF, Δt, is then related to a distance s, which is half the travel time multiplied by the speed of light c

$$s = \frac{c \cdot \Delta t}{2} \tag{3}$$

The spacecraft motion within the traveling time of the laser pulse, effects of relativity and atmospheric refraction are neglected here.

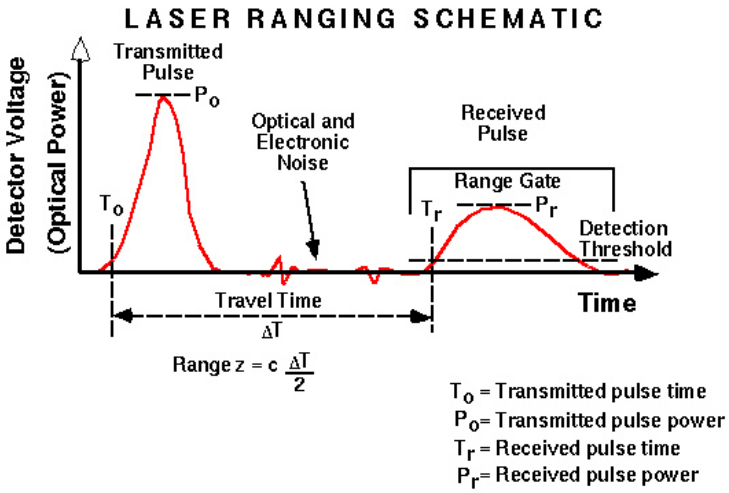

Figure 13: The time T_0 is recorded when a laser pulse is transmitted. During the travel time background noise can be seen on the detectors. Only pulses that fall within a predefined range gate window and are strong enough to exceed a preset detection threshold are considered valid ground shots with an arrival time of T_r. ©NASA

To derive a global height map of the central body, however, this distance measurement must be transformed into a height value, for which some additional information has to be available, compare Eq. 4 (see also Fig. 14).

$$h = \sqrt{d^2 + s^2 - 2 \cdot d \cdot s \cdot \cos\alpha} - R \tag{4}$$

In Eq. 4 d denotes the distance of the spacecraft to the Center of Mass (COM), s is the range measurement, α is the off-nadir angle and h is the height of the topography over the reference sphere of radius R. The distance d of the spacecraft to the COM is a crucial

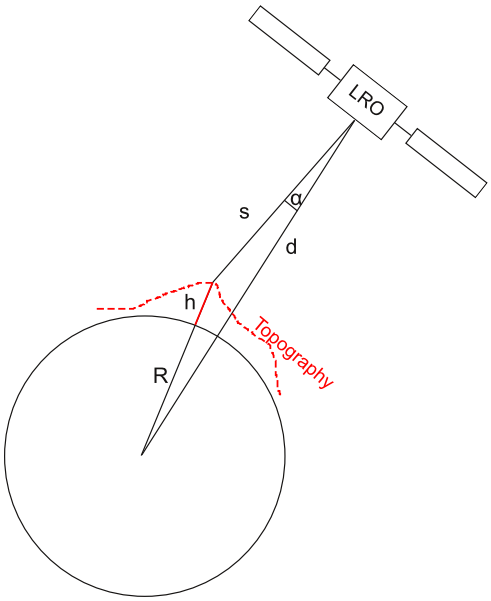

Figure 14: Geometric constellation of a laser measurement from orbit.

parameter in order to provide accurate measurements. Therefore, good knowledge of the planet's orbit and precise tracking of the spacecraft's trajectory are required to derive a good estimate. For the LRO mission tracking is accomplished via S-band Doppler for approximately 20 h per day with an accuracy on the order of 1 mm/s [Smith et al., 2010a]. The off-nadir angle α is carefully monitored by the attitude control of the spacecraft, e.g. by star cameras [Bae and Schutz, 2002; Lee et al., 2005]. The distance s is directly measured by the laser altimeter, e.g. LOLA measures this distance with a 10 cm ranging accuracy [Smith et al., 2010a]. The unknown distance $R + h$ can be determined with the law of cosines whereas R is the radius of the Moon, $R = 1737.4$ km [Seidelmann et al., 2007]. Solving the law of cosines for h leads to Eq. 4. By collecting distance measurements over the entire surface a global DTM of the body can be derived (see Fig. 21).

Laser Link Equation The laser link equation (Eq. 5) describes the relationship between the received signal pulse energy E_r and the transmitted laser pulse energy E_{tr}. The ratio of the two energies depend on the receiver's optic transmission τ_r, the receiver telescope aperture area A_r, the distance to the surface R, atmospheric transmission (one way) τ_a and the surface diffusive reflectivity r_s. This equation is of importance, for instance, when designing laser altimeters for planetary missions regarding required laser energy or deriving reflectance values of the observed surface within the laser footprint.

$$E_r = E_{tr} \cdot \tau_r \cdot \frac{A_r}{R^2} \cdot \frac{r_s}{\pi} \cdot \tau_a^2 \tag{5}$$

To derive an estimate on how much energy is received back at the telescope one has to evaluate the laser link equation. The following parameters are typical values for the LOLA instrument, Table 2. Evaluating the laser link equation with the parameters from Table

Table 2: Important parameters of LOLA to evaluate the laser link equation.

Parameter	**Variable**	**Value**
Receiver aperture radius	r	0.07 m
Area of receiver telescope aperture	A_r	0.015 m^2
Nominal orbit altitude	R	50 km
Energy of transmitted pulse (5 spots)	E_{tr}	3.2 mJ
Average energy per spot	τ_{r1}	15.62%
Average receiver optics transmission	τ_{r2}	89.1%
Average optical fiber transmission	τ_{r3}	97.02%
Average transmission ($\tau_{r1} \cdot \tau_{r2} \cdot \tau_{r3}$)	τ_r	13.5%
Albedo (regolith)	r_s	0.2

2 but varying the spacecraft altitude R we get the following results, see Table 3. The

Table 3: Typical spacecraft altitudes of LRO are ∼20-200 km. LOLA is optimized for detection of energies from 0.1 fJ to 3.0 fJ, which corresponds to spacecraft altitudes of ∼20 km to 120 km.

R **[km]**	E_r **[fJ]**	**No. of Photons**
20	3.32	17754
40	0.83	4438
60	0.36	1925
80	0.20	1069
100	0.13	695
120	0.09	481
140	0.06	321
160	0.05	267
180	0.04	214
200	0.03	160

number of photons were calculated using $E = 1.87 \cdot 10^{-19}$ J according to

$$E = \frac{hc}{\lambda} \tag{6}$$

The wavelength of LOLA is denoted by $\lambda = 1064.4\ nm$, the Planck constant is $h = 6.62606957 \cdot 10^{-34}$ J · s and $c = 299.792.458\ m/s$ is the speed of light in vacuum. Dividing the received energy E_{tr} as measured by LOLA by the energy of an emitted photon gives an estimate of the number of received photons.

5.2.2 LOLA specifications

Instrument A schematic of the LOLA instrument is shown in Fig. 15. The transmitter is a Q-switched Nd:YAG laser emitting at a wavelength of 1064 nm. The wavelength lies in the near-infrared spectrum which aligns with the spectral sensitivity of the built-in Avalanche Photodiode (APD) and the reflectance of the lunar surface. A Diffractive Optical Element (DOE) with 500 μrad spacing is used to split the transmitted laser beam into five individual beams. The five reflected laser beams are received at the telescope, where they are focused into a fiber optic array with five fibers. Each of the five fibers is aligned with a laser spot on the lunar surface. The fibers are connected to five detectors, which record the arrival of the laser beams. A more detailed description can be found in

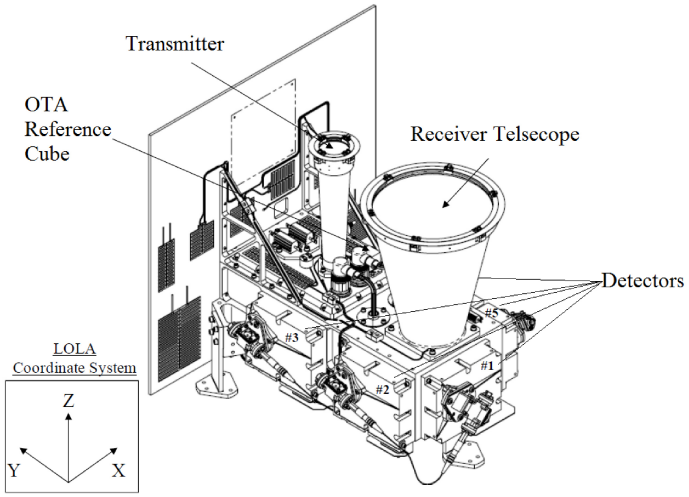

Figure 15: LOLA instrument and coordinate system. ©[NASA/GSFC]

the calibration document provided by Goddard Space Flight Center (GSFC) - NASA [Riris et al., 2010](Chapter 2 Page C-1).

Transmitter For redundancy reasons, LOLA is equipped with two identical Nd:YAG lasers referred to as laser 1 and laser 2, but only one laser operates at a time. The pulse repetition rate is 28 Hz for both lasers, while the pulse energy for laser 1 is ∼2.7 mJ and ∼3.2 mJ for laser 2. A x18 beam expander and the DOE transform the laser beam with originally 1.8 mrad divergence into five individual beams with 100 μrad divergence and 500 μrad beam separation. The laser beam pattern is also rotated by 26° relative to the spacecraft trajectory. From the nominal 50 km orbit this results in a X-shaped laser beam pattern with approximately 5 m diameter footprints of each laser spot and 10-12 m separation between successive laser spots and each profile (see Fig. 16). Table 4 and Fig. 17 show the performance of LOLA in comparison with other laser missions.
For more details see Riris et al. [2010](Chapter 2.1 Page C-3).

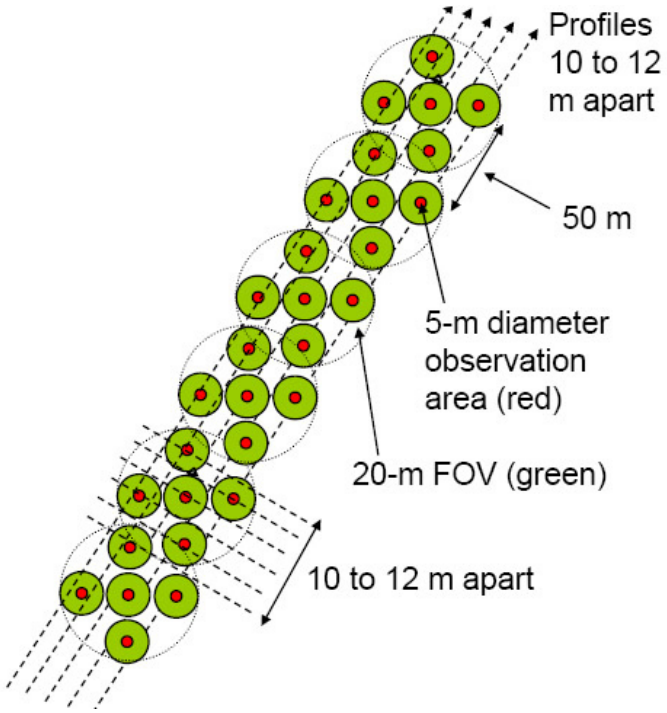

Figure 16: LOLA's X-shaped laser beam pattern on the lunar surface. ©[NASA/GSFC]

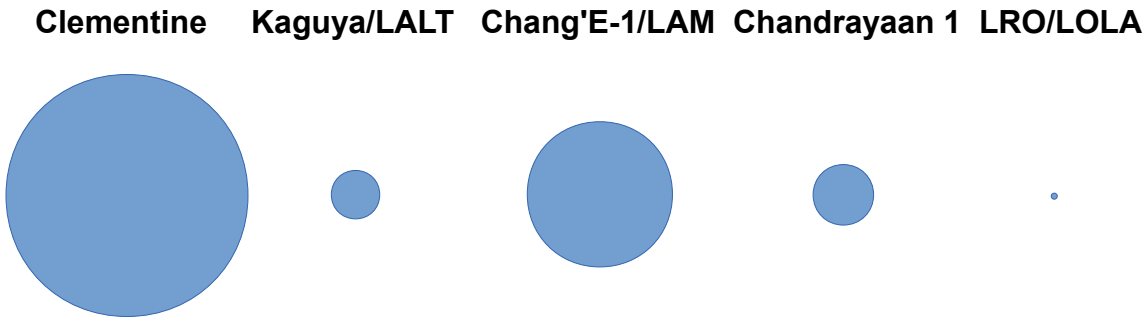

Figure 17: This plot shows a comparison of laser spot sizes from lunar missions, which carried a laser altimeter as described in Chapter 4.2, except Apollo.

Table 4: This list summarizes lunar missions carrying laser altimeters and their key parameters. LOLA already exceeds all previous missions by a factor of ∼200.

Mission / Instrument	Pulse Rate [Hz]	Spot size [m]	Orbit [km]	Surface points 10^6	Status
Clementine	0.6	200	400x8300	0.0723	ended 1994
Kaguya/LALT	1	40	100	20	ended 2009
Chang'E-1/LAM	1	120	200	8	ended 2009
Chandrayaan 1	10	50	100	?	ended 2009
LRO/LOLA	28	5	50	6000	ongoing

Receiver and Detectors The LOLA receiver is a 14 cm aperture refractive telescope. Its main purpose is to collect the maximum number of photons of the reflected laser pulses with few losses and a minimum of background radiation. For this reason a dielectric fold mirror, lucent for all wavelengths except for LOLA's 1064 nm wavelength, is installed in the aft-optics to minimize the incident of background solar radiation. The received laser beams are directed through ∼50 cm long fibers to the corresponding APD. Each of the five receivers (detectors) has a Field of View (FoV) of ∼400 μrad, which leads to a circle of 20 m in diameter on the ground as seen from a nominal orbit altitude of 50 km. The aft-optics for detectors 2-5 are identical while detector 1 also contains the laser ranging aft-optics (see 5.2.4).

The detectors are identical to the ones used for MOLA, and were designed to detect reflected laser beams from planetary surfaces and measure the TOF. Each detector has its own gain control and threshold settings. For more details see Riris et al. [2010](Chapter 2.2 Page C-4 and Chapter 2.3 Page C-6).

LOLA timing and range measurement The LRO spacecraft provides a 1 Hz timing signal. This 1 s interval is called a major frame, consisting of 28 approximately 35.71 ms long periods, which are called minor frames. LOLA operates at a pulse rate of 28 HZ and is phase locked to the 1 HZ timing signal of LRO. Therefore, each laser measurement (1 pulse per 35.7 ms) falls into a minor frame, and all 28 measurements occur within one major frame. The minor frames start at a time designated as T_0, followed by a 8 ms window dedicated for receiving laser signals from Earth at detector 1 (see 5.2.4 and Fig. 18). Approximately 9.66 ms after T_0 the laser is fired and the transmitted pulse is time stamped at detector 4 (see 5.2.1). An adjustable 0-5 ms range gate window follows the laser firing event, the range gate window therefore allows distance measurements from 0-750 km orbit altitude (see 5.2.1 and Fig. 18). Depending on the actual spacecraft orbit the range gate is set, e.g. from the nominal orbit altitude of 50 km a laser return is expected 0.33 ms ($t = 2 \cdot s/c$; s = 50 km, c = 299.792,458 km/s) after the fire command. Between the transmit and receive time of a laser measurement the detectors perform a noise count, which is used to set the threshold levels for the detectors. If a threshold crossing within the range gate window occurs on one of the detectors, the receive time of the actual detector is triggered. The remaining time of the minor frame is used to transfer the science data. For more details see Riris et al. [2010](Chapter 2.4 Page C-7 and Chapter 2.5 Page C-10).

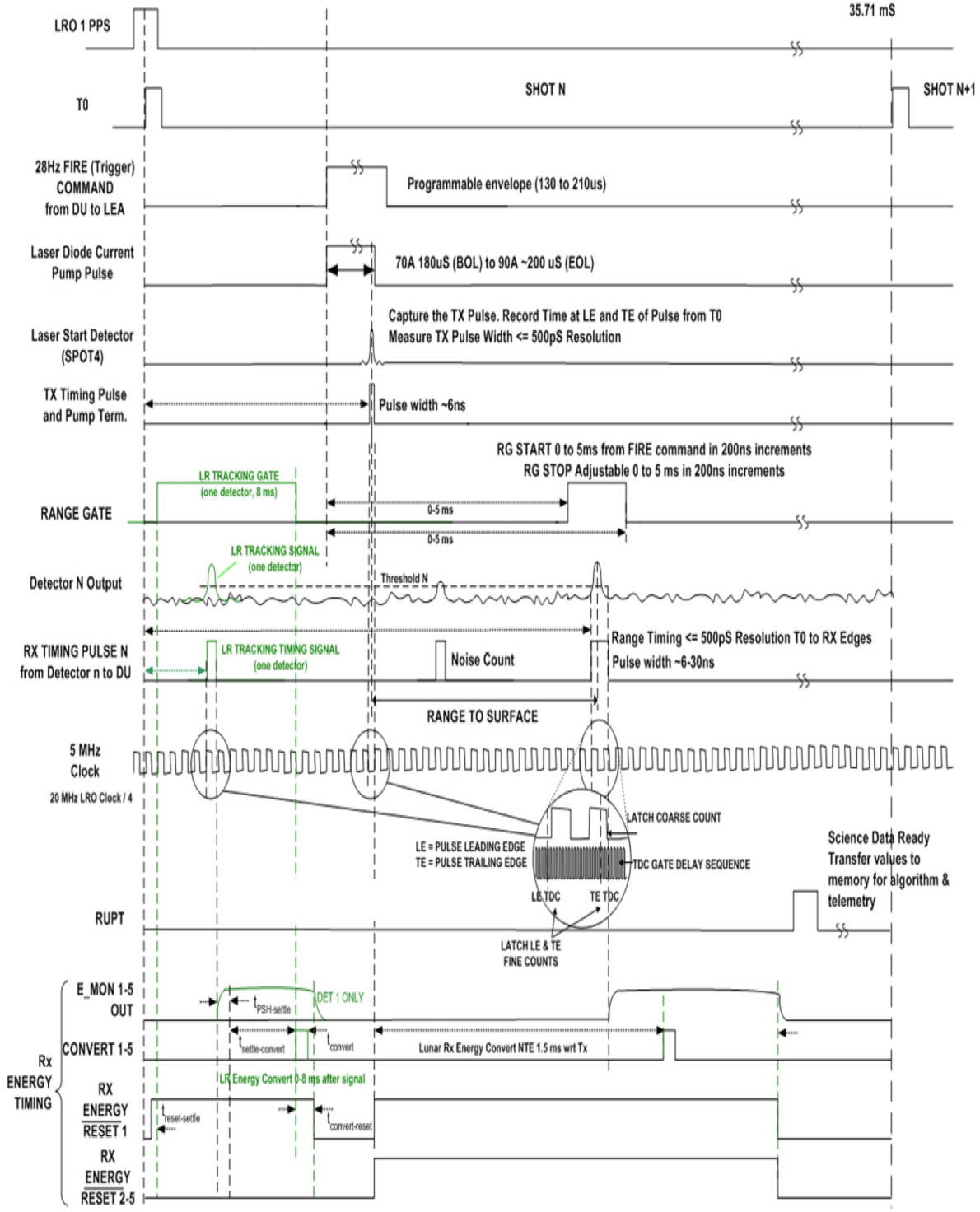

Figure 18: This diagram shows all events that occur within a minor frame of approximately 35.71 ms length. In each minor frame one pulse is sent out and 5 pulses are received, taken from GSFC - NASA [Riris et al., 2010].

5.2.3 LOLA anomaly

One orbit revolution of LRO at the nominal orbit altitude of ∼50 km lasts about 112-115 min (∼6800 s). The LOLA track from orbit 8537 (LOLARDR_111201131.DAT) is shown in Fig. 19, where the topography measured from each of the five spots is displayed individually over time. The two vertical black lines indicate the terminator, the location where LRO is crossing from the day to the night side of the Moon and vice versa. In one orbit revolution LRO is generally crossing the terminator twice and in Fig. 19 the central area bordered by the vertical lines represents the night part of the orbit. Only when the solar phase angle is 90°, LRO is orbiting exactly over the terminator. It clearly can be seen that detectors 1, 2 and 5 are not able to record laser bounces on the night side whereas all spots can be measured on the day side of the Moon. This effect is observed for all LOLA tracks and is most likely caused by contraction of a Multilayer Insulation (MLI) blanket which covers LRO and amongst others is attached between the LOLA transmitter optics and the receiver telescope [Chakraborty, 2011; Smith et al., 2010b]. The contraction of the MLI blanket pulls on the instrument in a way that the five spot pattern moves out of the focus of the receiver. However, as can be seen in Fig. 19, spot 3 and 4 can almost constantly be recorded throughout the entire orbit. This can be attributed to the fact that the mechanic pull of the MLI blanket is 600 μrad in the Y-direction of the LOLA-frame, allowing the receiver to record laser pulses from spot 2 and 5 at detector 3 and 4 [Mazarico et al., 2012b]. After crossing from the night side to the day side nominal operations with five measuring detectors is restored.

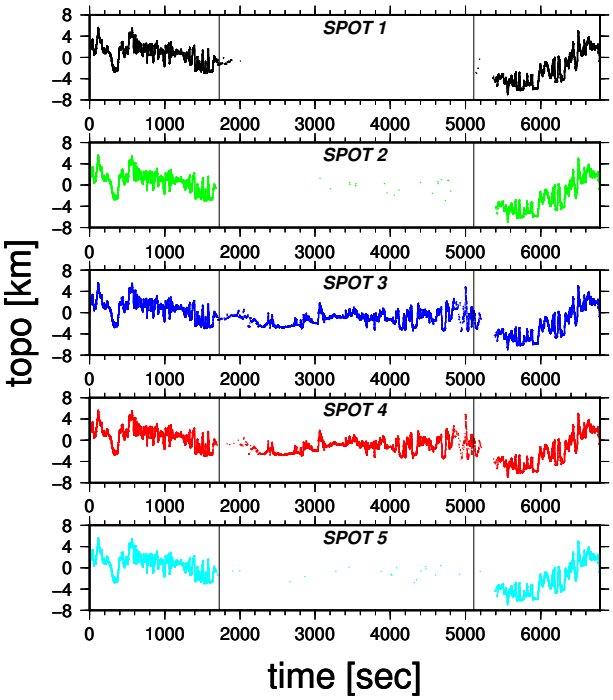

Figure 19: Profiles for each of the five spots of orbit 8537 are displayed. The two vertical black lines indicate the terminator, in between which LRO is above the night side. Only detector 3 and 4 record lunar returns on the night side.

5.2.4 LRO Laser Ranging

The LRO Laser Ranging (LRO-LR) system can precisely measure LRO's distance from Earth and helps achieve the orbit determination requirements of the mission. Unlike LOLA, which makes two-way range measurements from orbit to the Moon and back, the LRO-LR makes one-way range measurements from Earth to LRO. From an Earth-based laser facility, e.g. GSFC's Next Generation Satellite Laser Ranging System (NGSLR), a laser pulse is sent to LRO and the arrival time is recorded at detector 1 of the LOLA instrument (see Fig. 20). Since LOLA is always pointing towards the Moon, the laser pulse cannot be directly received by the LOLA receiver telescope. The High Gain Antenna (HGA), however, is always pointing towards Earth and makes the receiving of laser pulses possible when LRO is visible and in the line of sight from the laser station. For this purpose a receiver telescope was mounted on the LRO HGA and connected over a fiber cable, which routes the signal to detector 1 of LOLA.

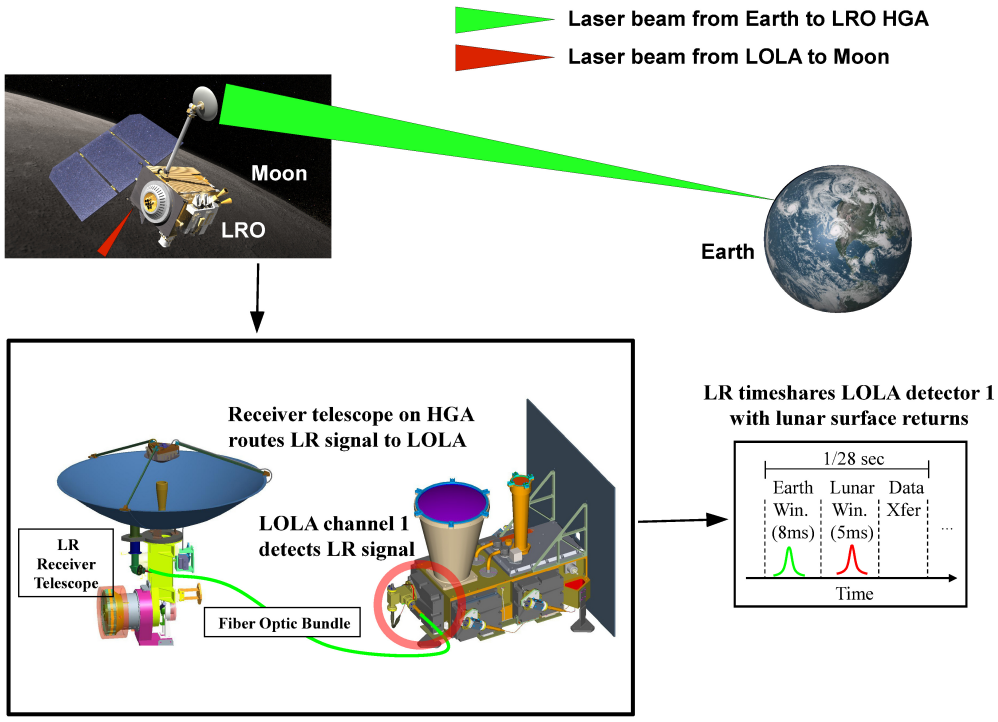

Figure 20: Schematics of Lunar Laser Ranging to LRO. The Earth based laser station sends out a laser beam which is received by LRO through the High Gain Antenna. From there it is directed over a fiber to detector 1 of LOLA. ©[NASA/GSFC]

5.2.5 LOLA data processing

The LRO spacecraft's nominal orbit period of 112-115 minutes allows for about 12.7 orbits per day. LOLA performs 140 measurements per second (28 Hz combined with 5 individual beams), which in total amounts to ∼1 million individual shots per orbit (compare LOLA performance with other laser missions in Table 4 and Fig. 17). Typically, data from each new orbit are stored on-board the spacecraft data recorder in a separate file. The down-linked files are transferred from the LRO Mission Operations Center (LRO-MOC) to the LRO Science Operations Center (LRO-SOC), where the raw data stream is automatically processed. Several times a year LRO's entire processed data stream since the last upload is transferred to NASA's Planetary Data System (PDS). PDS is an online archive system for data from planetary missions, astronomical observations, and laboratory measurements. All files are stored in a common data description, made available to the public and are updated if necessary.

Similar to any other planetary data set, there are likewise a number of processing levels for the LOLA data set (see Table 5). The first stage, Level 1, is referred to as the raw data stream from LRO. The Experiment Data Record (EDR) is the first edited level, referred to as Level 2 [Neumann, 2009a]. Although all entries are still raw data, they are now chronologically organized and free of duplicates. A data record as well as a detached PDS label exists for each orbit including the following information: location, record size, producer name and production time. The Reduced Data Record (RDR), Level 3, is time-ordered, calibrated to physical units and geolocated [Neumann, 2009b]. The file naming of this data record is in one-to-one correspondence to the EDR product. The Gridded Data Record (GDR) or Level 4 data are binned and interpolated data, such as gridded DTMs [Neumann, 2009c] (see Fig. 21). Transformed spherical harmonic coefficients are referred to as the Spherical Harmonic Analysis Data Record (SHADR) or Level 5 data products [Neumann, 2009d].

Within the scope of this work software tools were developed to read the binary EDR and binary RDR data records. Usually only data from the RDR records are used, however. GDR records are derived directly from the RDR products using the Generic Mapping Tool (GMT) (see Appendix A).

Table 5: Table of data processing levels of LOLA [Neumann, 2009a], [Neumann, 2009b], [Neumann, 2009c], [Neumann, 2009d].

Level	Description
EDR	The data set consists of uncalibrated observations. It is a time series collection of science and housekeeping data from LOLA, aggregated exactly as they are stored on the LRO spacecraft before being downlinked. Except where noted, they are complete and free from duplicates or errors.
RDR	The RDR data set is a time-ordered collection of measurement data from LOLA, calibrated, geolocated, and aggregated by orbit. Each topographic return is located with respect to the lunar center of mass in a body-fixed (rotating) coordinate frame.
GDR	The LOLA GDR data products consists primarily of raster DTMs formatted as binary images with detached labels. Ancillary gridded (binned, averaged) datasets consist of sample density, slope, roughness, geoid height, 1064-nm surface reflectance, and footprint-scale roughness from return pulse spreading that has been corrected for regional slope effects [Neumann et al., 2003].
SHADR	This data set contains spherical harmonic topographic (shape) and gravity potential models from the LOLA instrument, LRO Laser Ranging, and radio tracking.

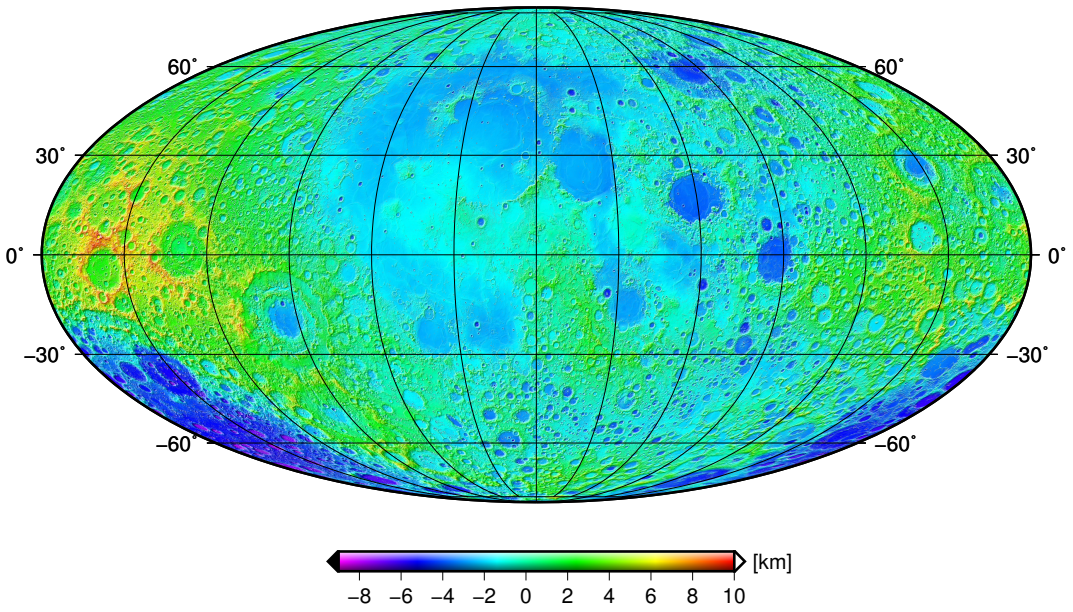

Figure 21: A global lunar LOLA DTM at 480 m/pixel resolution using a Mollweide map projection centered at the nearside of the Moon. Height values are color coded.

5.3 LROC - Lunar Reconnaissance Orbiter Camera

The LRO Camera LROC consists of three cameras, two Narrow Angle Cameras (NACs) and a Wide Angle Camera (WAC). Two of the primary LRO measurement requirements [Chin et al., 2007; Robinson et al., 2010] are directly addressed by LROC:

- Assessment of meter and smaller-scale features in order to facilitate safety analysis for potential lunar landing sites near polar resources and elsewhere on the Moon.
- Acquire multi-temporal synoptic 100 m/pixel imaging of the poles during every orbit to unambiguously identify regions of permanent shadow and permanent or near-permanent illumination.

5.3.1 NAC Instrument

The two NACs [Robinson et al., 2010], NAC-Left (NAC-L) and NAC-Right (NAC-R), are identical cameras with 700-mm focal-length telescopes mounted side by side on-board LRO, Fig. 22. Each camera uses a 5000-pixel Charged-Coupled Device (CCD) line-array with an Instantaneous Field Of View (IFoV) of 10 μrad yielding to a 2.85° across-track field-of-view. From the nominal orbit altitude of ∼50 km a total ground track swath-width of 5 km can be achieved when combining both cameras. NAC is a line-scanner or also called push-broom camera, which continuously obtains image lines while orbiting the Moon. Each NAC internal buffer holds 256 MB of uncompressed data, enough for a full-swath images of 25-104 km in length (depending on the compression being used).

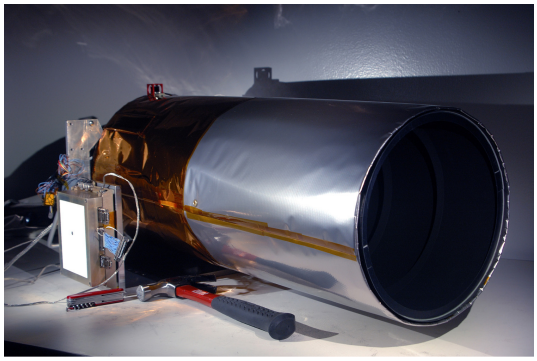

Figure 22: One of the two identical 700-mm focal-length NAC telescopes. See hammer for size comparisons. ©[NASA/GSFC/ASU]

The NAC-L is mounted ∼2.85° off the NAC-R camera, which is approximately the field-of-view of each camera. This way the footprints of the two images overlap by only ∼135 pixels in across-track direction at a nominal orbit altitude of ∼50 km. The NAC-R camera also points 0.106° forward compared to NAC-L, which correspond to ∼185 pixels downtrack.

5.3.2 WAC Instrument

The WAC uses a 1000 x 1000 pixels CCD chip imaging the Moon at a scale of ∼75 m/pixel (nadir) to ∼100 m/pixel (far-field) from the nominal 50 km orbit [Robinson et al., 2010], Fig. 23. WAC is a so-called push-frame or frame camera, where similar to most commercial cameras a whole image is taken at a time in contrast to line-scanners like NAC, where only single lines of pixels are recorded. Seven narrow-band interference filters are attached to the CCD, two for Ultraviolet (UV) light and five for Visible (VIS) light. In monochrome mode, WAC images over a 105 km swath and 60 km in color mode. In UV mode WAC images over a 57 km swath with a nadir resolution of 384 m/pixel.

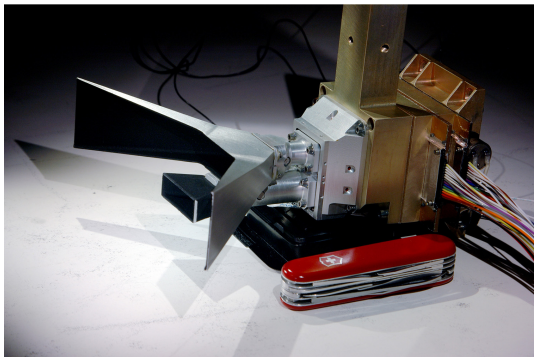

Figure 23: The WAC camera. See clasp-knife for size comparisons. ©[NASA/GSFC/ASU]

.

5.3.3 Digital Terrain Model processing

The production of DTMs from image data is a standard technique in planetary science [Oberst et al., 2010; Preusker et al., 2010; Scholten et al., 2012]. The relationship between a pixel in the image coordinate system and the corresponding 3D point on the surface is given in Eq. 7. These equations are the so-called collinearity equations which are elementary for photogrammetry. Here, X_0, Y_0, Z_0 and x_0, y_0 correspond to the projection center and image center, respectively. The entries of the rotation matrix between the 2D image coordinate system and the 3D coordinate system (e.g. body-fixed) are given as r_{rc} and the camera constant is c. If a point is found in 2 images this leads to 4 equations (2 for X and 2 for Y) and 3 unknowns (X, Y, Z), which has a unique solution.

$$\begin{aligned} X &= X_0 + (Z - Z_0)\frac{r_{11}(x - x_0) + r_{12}(y - y_0) - r_{13}c}{r_{31}(x - x_0) + r_{32}(y - y_0) - r_{33}c} \\ Y &= Y_0 + (Z - Z_0)\frac{r_{21}(x - x_0) + r_{22}(y - y_0) - r_{23}c}{r_{31}(x - x_0) + r_{32}(y - y_0) - r_{33}c} \end{aligned} \tag{7}$$

In general a DTM can be derived from image data when a surface patch has been recorded at least two times from different viewpoints, see Fig. 24. For LRO this is achieved, for instance, by rotating the spacecraft across-track by an angle of $\alpha = \sim 30°$ from nadir

to image a surface patch that was seen by the previous orbit in nadir orientation. This angle originates from the geometry of the nominal orbit where the baseline between two successive orbits at the equator is 30 km and the orbit altitude is 50 km. As a rule of thumb it can be noted that the larger the angle α ($0 < \alpha < 90°$) the higher the vertical accuracy of the DTM. On the other hand, mountains and craters seen from a high angle α will cause large occlusions in the image. The quality of the DTM, however, strongly depends on orbit geometry, lighting conditions and image quality. LRO's orbit duration of ∼2 h will ensure the same lighting conditions for the two images since the lunar rotation is negligible in such a short period. Similar lighting conditions in the two images are favorable for the matching process, in which corresponding pixels are automatically determined using the 2D image coordinate system (x,y). The matching process works best when the pixel gray values and shadow regions are almost identical since most of the commonly used routines for planetary data evaluation are based on gray value comparison methods like Normalized Cross Correlation (NCC) and least-squares matching. However, no 3D information can be derived for regions of dark shadows or very homogeneous texture as the matching algorithm fails to reliably find corresponding matches. The derivation of 3D surface points (X,Y,Z) requires the position and attitude of LRO, at the times of image acquisition.

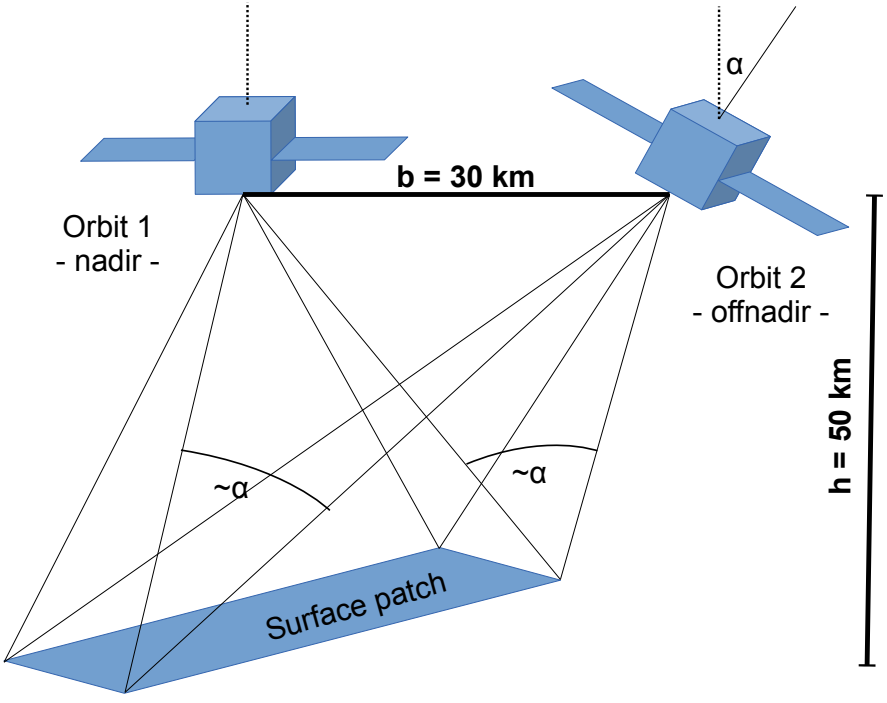

Figure 24: The principle of stereo imaging from orbit.

.

5.4 LRO orbit and gravity field

LRO is orbiting deep within the lunar gravity field, which is in turn greatly influencing LRO's orbit trajectory. For planning and targeting reasons, e.g. imaging the Apollo landing sites, orbits with ∼500 m navigation position and prediction knowledge are required. The Flight Dynamics Facility (FDF) at GSFC releases such orbits for the instrument teams to plan their observations [Mazarico et al., 2011b]. However, a total position knowledge of 50-100 m and 1 m radially is needed to ensure a precise geolocation of the various LRO instrument data [Vondrak et al., 2010]. Hence, a near-continuous tracking of the spacecraft is carried out to obtain more precise post-processed orbit trajectories. The radiometric tracking of LRO is done by the LRO-dedicated NASA station in White Sands and by commercial tracking stations of the Universal Space Network (USN). All stations produce Doppler and range data, with White Sands achieving a tracking performance of ∼0.3 mm s^{-}1, ∼0.2 m in Doppler and range measurements and USN ∼0.4-0.8 mm s^{-}1 and ∼0.4 m, respectively [Mazarico et al., 2012b, 2011b]. As a first step, post-processed orbits incorporating the radiometric tracking data are derived by the Precise Orbit Determination (POD) team using the GEODYN software [Pavlis et al., 2006]. The underlying, a priori gravity field is the co-called GLGM-3 of degree and order 150, derived from previous lunar missions (Lunar Orbiters, Apollo, Clementine and Lunar Prospector) [Mazarico et al., 2010]. Short arcs of 2.5 days are integrated to minimize the buildup of errors occurring from mismodeling of forces and measurement corrections. These arcs typically overlap by ∼10 h, where Root Mean Square (RMS) position differences can be calculated and serve as a measure of precision. For the considered period from July 13, 2009 to January 31, 2011 a total overlap difference of ∼70 m RMS is observed for the post-processed orbits using radiometric tracking [Mazarico et al., 2012b]. The resulting 'radio orbits' already meet the position knowledge requirements of 50-100 m RMS.

Further improvements can be gained, however, by incorporating the so-called crossover locations of laser tracks into the orbit reconstruction process. A crossover location is the intersection between two altimetric tracks, e.g. LOLA tracks, where the observed surface height of each track must be the same by definition. Generally, the observed surface heights will not be identical and the difference can be used to constrain the spacecraft orbits. Since the small-amplitude tides of the Moon are in the order of ∼5-10 cm, they are within the LOLA noise level and observed surface height differences can be directly related to orbit inaccuracies [Mazarico et al., 2012b; Smith et al., 2010a; Williams et al., 2008]. Due to the 5 spot LOLA pattern, crossover locations can not only be determined in along-track direction but, for the first time, also in cross-track direction. These are now called swath-crossovers, because they are not limited to a single position but an extended area, and can create km-long swaths when intersection angles are shallow. For single spot lasers like MOLA, exact crossover locations at shallow intersection angles are difficult to be identified, however they are preferably locations for multi-spot lasers like LOLA [Mazarico et al., 2009, 2011b]. Almost all crossovers occur near the lunar poles due to LRO's near-polar orbit and the slow rotation of the Moon. For the considered period from July 13,

2009 to January 31, 2011 a total of ∼159,000 crossover locations were added into the POD together with the prior derived 'radio orbits'. Radiometric tracking data along with crossover locations further improve orbit precision, from measured orbit overlaps of ∼70 m RMS for only using radiometric data to a total of ∼23 m RMS using both [Mazarico et al., 2012b].

Based on these high precision orbits, a new gravity field can be derived by using the remaining signal in the measurement residuals. Normal equations from the GLGM-3 gravity field are combined with LRO normal equations and a combined gravity inversion is performed. The resulting degree and order 150 LLGM gravity field can again be used to improve the orbit accuracy of LRO. The same analysis as described before is performed again but this time based on the newly derived LLGM gravity field. Using radiometric tracking data alone, the average overlap difference in total position is ∼24 m RMS and ∼14 m RMS, when adding the crossover locations.

With the launch of the twin GRAIL spacecraft Ebb and Flow in September 2011 [Zuber et al., 2013], the recovery of the lunar gravity field in unprecedented accuracy was feasible. Based on a GRAIL gravity field of degree and order 420, truncated to degree and order 270, a significant improvement of the LRO orbit determination is achieved. For various mission periods, a total position difference at orbit overlaps of ∼6-11 m RMS can be observed [Mazarico et al., 2013].

6 Data Evaluation

The goal of this study is to evaluate landing sites near the lunar south pole including topography, Earth visibility, illumination, slopes and roughness. As already mentioned in Chapter 2, an accurate DTM is required to accomplish the goal. The following chapters describe the derivation of a precise south polar DTM and the further analysis necessary to characterize a landing site on the Moon regarding illumination, Earth visibility, slope and roughness.

6.1 Co-Registration of LOLA and NAC

The LRO mission and two of its instruments, LOLA and LROC NAC, primarily used in this work, are described in the previous Chapter 5.2, 5.3. While LOLA is directly measuring the lunar topography in 3D space along the LRO ground track [Smith and Zuber, 2000; Smith et al., 2000, 2011a], NAC is imaging the surface in 2D [Haase et al., 2012; Oberst et al., 2010; Robinson et al., 2010; Scholten et al., 2012]. Photogrammetric techniques to derive DTMs from NAC images are described in Chapter 5.3.3. In this study NAC DTMs were provided by Deutsches Zentrum für Luft- und Raumfahrt (DLR). NAC and LOLA are mounted on LRO in a way that both are pointing in nadir direction, with LOLA acquiring a profile just between the left and right NAC image. As a result each NAC DTM will be intersected by at least one LOLA profile. Although highly dependent on the extent and latitude of the NAC DTM, usually a larger number of LOLA tracks is found per DTM, ranging from a few tracks to several hundreds of tracks. The number of tracks intersecting a NAC DTM increases towards the poles since LRO is in a polar orbit and all LOLA tracks are converging at high latitudes (polar regions). When comparing a LOLA profile with a profile extracted at the same location in the NAC DTM, differences are noticeable. The profiles generally have a slightly different shape and also often have a height offset to each other. These typical displacements occur if the DTM and the LOLA profiles are offset to each other in lateral and vertical direction. This chapter describes how to co-register the two data sets making use of their individual advantages [Gläser et al., 2013a, 2010]. The LOLA profiles for instance have a highly accurate relative and absolute height measurement, implying that the shape of the profile and the height above the sphere are accurate whereas the relative lateral positions of laser profiles are less accurate. A NAC DTM covers a comparably large area with respect to a single LOLA profile, and therefore, can precisely relate lateral positions of individual profiles, while the overall height accuracy is less accurate than for LOLA.

In summary it is feasible to first co-register all LOLA tracks to a NAC DTM and derive a constant shift between the two datasets. By applying this constant offset to the NAC DTM, it will be rigorously tied to the LOLA point cloud and hence increase its absolute positional accuracy. The remaining residual offsets between each LOLA profile and the NAC DTM can be applied to the individual profiles to constrain their relative position to

each other.

6.1.1 Previous work

The Mars Orbiter Camera (MOC) together with MOLA, both flown on-board the Mars Global Surveyor (MGS), scanned the Martian surface with images and laser. In order to co-register MOLA tracks with MOC but also VIKING images, Kim et al. [2000] used visible edges of surface features such as craters to tie the data sets together. This approach, however, only registers the data in 2D space and only finds a solution if the surface feature can be detected in both data sets. The resulting accuracy of the co-registration therefore highly depends on the hierarchical and heuristic edge detection method, which is used in their work. A combined adjustment of MOC stereo images and MOLA data is shown in Yoon and Shan [2005]. MOLA ranges and surface points, trajectory data and tie points of the images are adjusted simultaneously using least-squares techniques. While the ground location of MOLA surface points is improved, no additional condition to minimize the displacement between the MOLA profile and the corresponding MOC DTM profile is introduced in the algorithm. Kolb and Okubo [2009] introduced a software tool for co-registering MOLA tracks with images obtained by MOC, the High Resolution Imaging Science Experiment (HiRISE) and the Context Camera (CTX). A lateral shift between the images and MOLA tracks is manually applied by the user, but the two data sets cannot be co-registered in 3D space. Another approach is to register laser derived DTMs with stereo DTMs instead of only using a single laser track. Di et al. [2012] and Lin et al. [2010] for instance make use of surface matching techniques. While Di et al. [2012] co-register Chang'E-1 stereo DTMs and crossover corrected LAM DTMs, Lin et al. [2010] match MOLA DTMs with High Resolution Stereo Camera (HRSC) and HiRISE DTMs. In both cases, however, the laser DTMs will contain large interpolated data gaps and tracks suffering from positional errors.

6.1.2 Bilinear Interpolation

This chapter describes the bilinear interpolation used in the co-registration algorithm. When comparing profiles from LOLA and NAC DTMs, the gridded NAC DTM needs to be interpolated at the LOLA spot positions. An interpolation allows for the calculation of meaningful height values at each arbitrary point in the DTM, although position and height values are usually only available at the grid points of the DTM. A typical example of a LOLA spot on a DTM grid is shown in Fig. 25. To retrieve a height value in the DTM at the position of the LOLA spot, the four DTM heights (center of each pixel) will be used. A linear interpolation is first performed in the x-direction and then in the y-direction. As indicated in Fig. 25 the height value of interest at the position of the LOLA spot, $l = (x, y)$, is surrounded by the known height values of the DTM at each pixel center, described by $h_{11} = (x_1, y_1)$, $h_{21} = (x_2, y_1)$, $h_{12} = (x_1, y_2)$ and $h_{22} = (x_2, y_2)$. Performing a

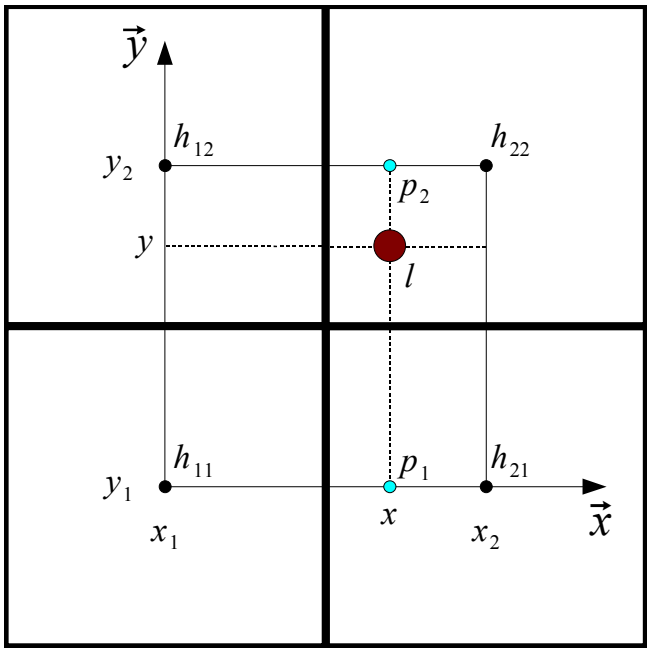

Figure 25: To calculate a height value at the position l of the LOLA spot (red) the four surrounding DTM points (black) are needed.

linear interpolation in the x-direction leads to

$$\begin{aligned} f(p_1) &= \frac{x_2 - x}{x_2 - x_1} f(h_{11}) + \frac{x - x_1}{x_2 - x_1} f(h_{21}) \\ f(p_2) &= \frac{x_2 - x}{x_2 - x_1} f(h_{12}) + \frac{x - x_1}{x_2 - x_1} f(h_{22}) \end{aligned} \tag{8}$$

with $p_1 = (x, y_1)$ and $p_2 = (x, y_2)$.

For the interpolation in the y-direction

$$f(l) = \frac{y_2 - y}{y_2 - y_1} f(p_1) + \frac{y - y_1}{y_2 - y_1} f(p_2) \tag{9}$$

is found. Inserting Eq. 8 into 9 yields to the estimate of $f(x, y)$

$$\begin{aligned} f(x,y) &= \frac{h_{11}}{(x_2 - x_1)(y_2 - y_1)}(x_2 - x)(y_2 - y) \\ &+ \frac{h_{21}}{(x_2 - x_1)(y_2 - y_1)}(x - x_1)(y_2 - y) \\ &+ \frac{h_{12}}{(x_2 - x_1)(y_2 - y_1)}(x_2 - x)(y - y_1) \\ &+ \frac{h_{22}}{(x_2 - x_1)(y_2 - y_1)}(x - x_1)(y - y_1) \end{aligned} \tag{10}$$

6.1.3 Co-Registration Algorithm

The goal is to co-register LOLA profiles and NAC DTMs. This is achieved by minimizing the height differences of the LOLA profile, consisting of n laser spots, and the profile extracted from the NAC DTM,

$$\sum_{i=0}^{n}(h_{dtm_i} - h_{laser_i})^2 \rightarrow min \tag{11}$$

with h_{laser_i} being the *i-th* laser spot height value and h_{dtm_i} the corresponding interpolated height in the DTM. The laser profile is then shifted from its nominal lateral location in a predefined window, pixelwise in sample and line, over the NAC DTM. This so-called grid search approach extracts a profile in the DTM at each position in the search window using a bilinear interpolation (see Chapter 6.1.2). According to Eq. 11 the standard deviation of the height residuals, $\sigma_{h_{l,s}}$, between the two profiles is determined at each position in the search window, denoted by line l and sample s:

$$\sigma_{h_{l,s}} = \sqrt{\frac{\sum_{i=0}^{n}((h_{dtm_{i,l,s}} - h_{laser_i}) - \mu)^2}{n-1}} \tag{12}$$

The mean height offset is given by μ and the number of laser spots and interpolated DTM heights is denoted by n. The minimum of Eq. 12 defines the best match between the two profiles at pixel-level accuracy. In order to retrieve sub-pixel accuracy, a one-pixel area centered around the found position is divided in a sub-pixel grid, e.g. in cells of 1/30 of a pixel. At each sub-pixel position Eq. 12 is evaluated and the minimum will lead to the refined position of the best match.

$$\sigma_{h_{l+sub_l,s+sub_s}} = \sqrt{\frac{\sum_{i=0}^{n}((h_{dtm_{i,l+sub_l,s+sub_s}} - h_{laser_i}) - \mu)^2}{n-1}} \tag{13}$$

The sub-pixel position that is found directly leads to the translational parameters x, y, z in sample, line, h direction between the LOLA and the NAC DTM profile. To derive accuracies for these parameters a least-squares adjustment is performed. The functional model is

$$\boldsymbol{F}(\boldsymbol{L}, \boldsymbol{X_0}) = \boldsymbol{H} - \boldsymbol{f}(x + \Delta x_0, y + \Delta y_0) - (z + \Delta z_0) = \boldsymbol{0} \tag{14}$$

The vector $\boldsymbol{H}$ contains the laser heights, $\boldsymbol{f}(x + \Delta x_0, y + \Delta y_0)$ is the vector of height values retrieved by the bilinear interpolation of the DTM at the laser spot positions and $z + \Delta z_0$ is the scalar, vertical offset between the two data sets. The so-called vector of unknowns $\boldsymbol{X_0}$, represented by the initial values $(\Delta x_0, \Delta y_0, \Delta z_0)$, is added to the positions of the laser spots (x, y, z), which were previously derived by the grid search algorithm. The initial values are all set to 0, assuming, that the positions that are found by the grid search algorithm already satisfy Eq. 14. If that assumption holds, the difference between each laser height and the interpolated DTM height at the laser spot positions corrected for a constant offset should be 0.

In order to derive accuracies for the translational parameters, the variance-covariance matrix of the adjusted unknowns, $\boldsymbol{S}_{\hat{\boldsymbol{x}}\hat{\boldsymbol{x}}}$, has to be evaluated.

$$\boldsymbol{S}_{\hat{\boldsymbol{x}}\hat{\boldsymbol{x}}} = s_0^2 \boldsymbol{Q}_{\hat{\boldsymbol{x}}\hat{\boldsymbol{x}}} \tag{15}$$

The main diagonal holds the squares of $(\sigma_{\Delta x_0}, \sigma_{\Delta y_0}, \sigma_{\Delta z_0})$ pointing in sample, line and h direction (longitude, latitude, h). If the parameters found by the grid search are valid then the resulting $\Delta x_0, \Delta y_0, \Delta z_0$ should not be significant, resulting in numerically smaller values than their corresponding accuracy levels $\sigma_{\Delta x_0}, \sigma_{\Delta y_0}, \sigma_{\Delta z_0}$.
For a more detailed description of the least-squares approach, see Appendix B.

6.1.4 Example

To demonstrate the workflow of the algorithm a NAC DTM of the Apollo 14 landing site with 2 m/pixel resolution and the intersecting LOLA track from orbit 3508 were chosen. The LOLA profile, consisting of 242 laser spots on the DTM, is shown at its nominal position together with the corresponding NAC DTM profile (Fig. 26). While the shapes

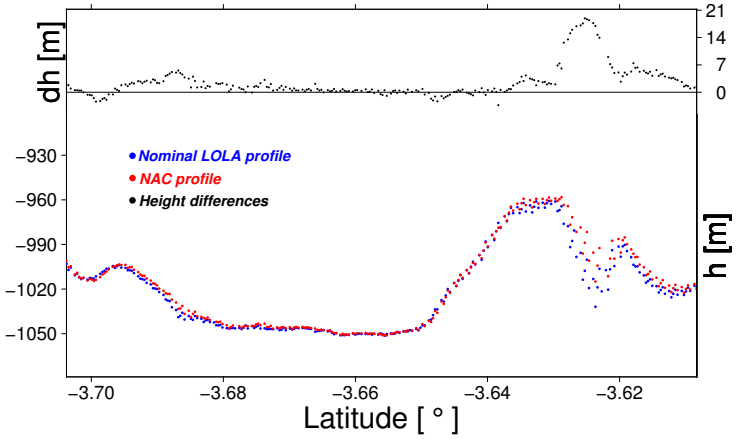

Figure 26: The LOLA profile at its nominal position together with the corresponding NAC DTM profile. Height differences between the two profiles are shown at the top of the plot. Height values are given in meters with respect to the sphere 1737.4 km.

of the two profiles are in good agreement, significant height differences are noted at the crater on the right hand side of the plot (standard deviation of residuals: approximately 4 m). Craters and other pronounced topographic signatures easily reveal lateral offsets and are crucial to precisely co-register the two data sets. This is explained by the fact that a laser track that is shifted in lateral direction from its correct position on a DTM, will result in substantial height differences with the DTM if the profile passes through rough terrain. If the terrain would be perfectly smooth only an offset in a vertical direction could be found. However, the differences are systematic (probably due to pointing or orbit errors) and can be corrected. Evaluating Eq. 12 leads to a residual field where the integer pixel shift between the two data sets is found at the minimum, see Fig. 27, left plot. In order to retrieve more accurate estimates for the offsets, a small area around

this integer pixel position is divided into a sub-pixel grid. Applying Eq. 13 will lead to refined offset parameters, see Fig. 27 right plot. After adding the determined offsets to

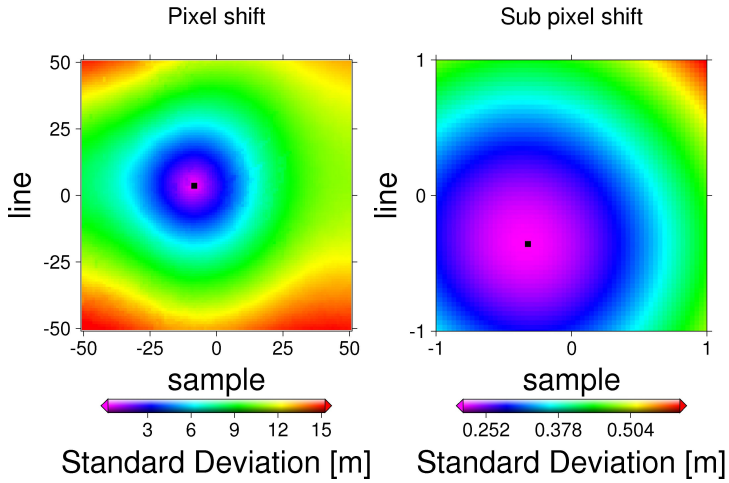

Figure 27: Left: Residual field of integer shifts of the grid search algorithm. Right: The result of sub-pixel grid search.

the nominal LOLA track and comparing the two profiles again, the standard deviation of the height differences drops to 21.12 cm (Fig. 28). The remaining height differences vary within the range of only ±50 cm, which are believed to originate mostly from differences in the effective height resolution of the DTM and the laser profile. The positions found

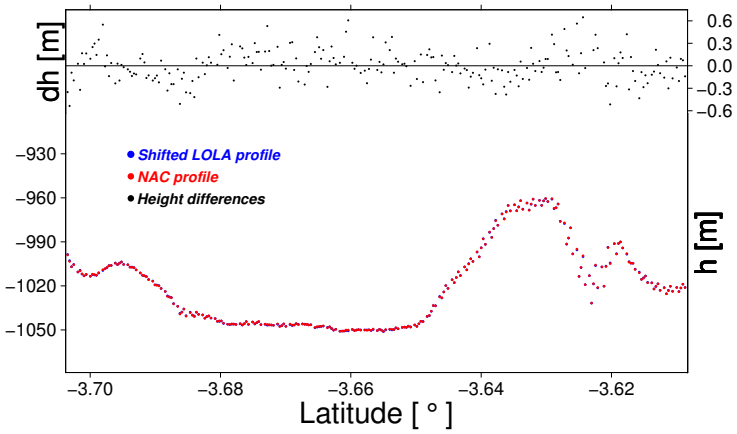

Figure 28: DTM heights and corresponding LOLA profile after applying the final translation parameters. The misplacement between the two data sets is minimal.

by the grid search, x, y, z, are then introduced in the least-squares algorithm (see Eqs. 14 and 47). The resulting standard deviations of the adjusted unknowns are $\sigma_{\Delta x_0} = 9.08$ cm, $\sigma_{\Delta y_0} = 8.68$ cm and $\sigma_{\Delta z_0} = 1.61$ cm, which attests to the robustness of the fit.

In total 12 LOLA tracks intersect the Apollo-14 DTM. Repeating the process for the remaining 11 tracks, as exemplarily described above, enabled the estimation of a mean offset between the two datasets. Generally, the more LOLA tracks intersect the NAC DTM

the stronger the statistical significance of the overall determined offset. In Fig. 29 the lateral displacements of each LOLA track to the NAC DTM are displayed. Lateral shifts of ∼-25 to ∼-14 m in x- and ∼-28 to ∼-13 m in y-direction can be observed leading to a mean offset of -18.5 m and -19.8 m respectively (red cross in Fig. 29). Standard deviations for the mean offset are calculated to be 3.7 m in x- and 4.9 m in y-direction, which are well within the expected accuracies of the LRO orbit reconstruction (see Chapter 5.4). Also, a mean total height offset between the two datasets of ∼1.8 cm is derived, revealing that the absolute height of the NAC DTM is practically identical to LOLA.

As mentioned before, standard deviations for each LOLA track are derived describing how accurate the track can be located on the NAC DTM. These parameters are typically within the order of 1/10th of a NAC DTM pixel in x- and y-direction and 1/100th of a NAC DTM pixel for the height component, for the given example above ∼20 cm and ∼2 cm respectively. In order to estimate the mean offset between the LOLA tracks and the NAC DTM, only results that are within an ellipse derived from the 3σ values of the standard deviations of the offset (3 x 3.7 m and 3 x 4.9 m) will be considered. LOLA profiles with large localization uncertainties are also excluded from the analysis. The final constant offset is determined to be -19.0 m in x- and -20.5 m in y-direction (green dot in Fig. 29). Shifting the NAC DTM according to the derived constant offsets leaves little remaining residual shifts for each individual LOLA track, which reflect the error of the LRO orbit reconstruction. The final products are a NAC DTM registered to the LOLA point cloud and LOLA tracks that are positioned accurately to each other.

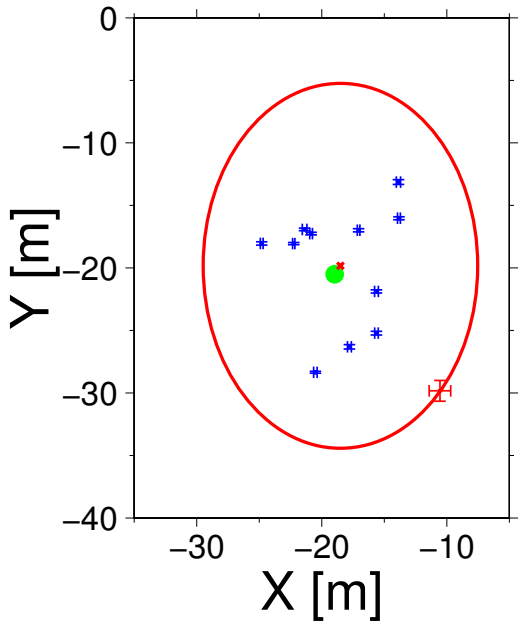

Figure 29: Displacements of the 12 LOLA tracks intersecting the Apollo-14 DTM. Error bars describe how precise the position of the LOLA profile could be located on the NAC DTM. Only LOLA tracks with displacements within a 3σ ellipse and small errors bars (blue) are used to derive a constant offset between the two datasets. Data points outside the ellipse or with large uncertainties are excluded (red error bars). The mean of all displacements is shown as a red cross, whereas the green dot is the derived offset between the two datasets.

6.2 Illumination conditions

The Moon's rotational axis forms an angle of ±1.54° with respect to the normal vector of the ecliptic plane which allows for extreme illumination conditions near the lunar poles. Only separated by short distances (order of km), areas of permanent shadow can exist next to areas with long illumination periods exceeding the biweekly day and night cycle. Both locations are of great interest for scientific missions. Permanently Shadowed Areas (PSAs) can harbor water ice, which could be harvested as a natural resource for drinking water and fuel production during future missions. Areas with long illumination periods are ideal for permanent base stations with large solar arrays providing almost continuous electrical power.

There are various programs at different space agencies for landing missions at the lunar south pole. The European Space Agency (ESA) planned a mission called Lunar Lander [De Rosa et al., 2012] and ROSCOSMOS plans two polar missions, Luna-Glob and Luna-Resource [Mitrofanov et al., 2011], see Chapter 4.3. In order to find such locations, two different approaches exist. For instance, polar images can be used to find areas of high, low and no illumination. Since the illumination conditions are changing over time due to the lunar precessional cycle of 18.6 years, the amount of image data necessary to cover the poles completely and also under different illumination conditions is difficult to accomplish. Another approach is to simulate illumination conditions using a DTM in combination with information about the lunar orbit and geometry with respect to the Sun. This chapter describes how illumination conditions are simulated using LOLA data.

6.2.1 Previous work

The existence of areas in permanent shadow as well as points of eternal light were discussed in several publications, e.g. [Bussey et al., 1999; Watson et al., 1961]. As described earlier, the most intuitive approach is to look at orbital images in order to describe illumination conditions for certain locations. The Clementine mission [Shoemaker et al., 1994] acquired many images of the lunar poles. The short mission lifetime of 71 days limited the investigation to just 2.5 lunar days during northern summer [Bussey et al., 1999]. In a more recent study Speyerer and Robinson [2013] used ∼7800 LROC WAC images to investigate lunar illumination conditions for a period from February 15, 2010 to February 5, 2011. Binary illumination maps were created from these images and resulted in a 100 m/pixel illumination map for a 1° area around each pole. For reliable long term results, however, the entire lunar precessional cycle of 18.6 years needs to observed.

In order to detect water ice at the lunar poles Stacy et al. [1997] analyzed polarization properties of the reflected Arecibo radar signal, an Earth based radar observatory. Due to the poor viewing geometry from Earth to the lunar poles, the incidence angle of the radar beam was 85.9° at the north pole and 83.9° at the south pole. The combination of the high incidence angles with topography resulted in extensive radar shadows and only occasionally areas of the farside of the Moon could be observed.

The second approach as mentioned before is to simulate illumination conditions using a DTM, from which illumination levels can be computed using geometric relationships for any time span of interest. Margot et al. [1999] used Earth based radar observation to derive polar DTMs with 150 m spatial and 50 m height resolution. Like the radar images, the radar DTMs suffer from data gaps on the farside, which introduce uncertainties in the topography and therefore also in the derived illumination conditions. The Japanese Moon mission Kaguya (Selene) delivered a complete direct measurement of lunar topography. Noda et al. [2008] used a LALT derived DTM with a resolution of 470 m and simulated illumination conditions over one lunar precessional cycle for both poles. Illumination conditions may change significantly within short distances due to the rough topography at the poles, therefore DTMs with higher resolution are needed for precise studies of illumination conditions at specific landing sites. LOLA is ideally suited for this study, owing to its high data resolution and geodetic control [Chin et al., 2007; Smith et al., 2010a]. Using a LOLA DTM with a resolution of 240 m, Mazarico et al. [2011a] simulated polar illumination conditions at twice the resolution as Noda et al. [2008]. A LOLA DTM of only 40 m resolution was used in a study carried out by De Rosa et al. [2012] to simulate illumination conditions for specific sites at the lunar south pole that are known to be highly illuminated. Those specific sites are currently under investigation by ESA for its Lunar Lander Project [Carpenter et al., 2012; De Rosa et al., 2012].

6.2.2 Horizon method

There are two different ways to simulate illumination conditions using DTMs, the so-called ray-tracing and the horizon method. Margot et al. [1999] and Noda et al. [2008], for instance, used a ray-tracing algorithm whereas Mazarico et al. [2011a] and De Rosa et al. [2012] used the horizon method. There can be substantial differences in computational times depending on the desired result. The ray-tracing approach starts with light rays emitted by the Sun at a certain time intersecting with each pixel in the DTM. If the ray can reach the pixel without being blocked, it will be in sunlight and vice versa. Illumination condition is calculated rather quickly for a single or a few time steps although the entire process has to be repeated for each time step. When simulating illumination conditions over 20 years with a sampling rate of 1 h, however, this approach is not efficient.

The horizon method starts in the DTM and first derives the horizon for each pixel in the DTM. Once the horizon is retrieved, the azimuth and elevation of the Sun at a certain time only needs to be compared with the corresponding elevation value of each pixels' horizon in order to decide whether it is illuminated or not. This approach requires a lot of computation time to set up the horizon maps, but once they are set up, any time span with any time step can be calculated very quickly. In this work the horizon method was chosen in order to evaluate long periods of time with less computational effort.

The steps in order to derive the illumination condition for a certain region at a certain time are as follows:

1. These steps have to be done only once for each DTM (very time consuming computation)

   (a) The horizon map of each pixel in the DTM sampled at a set of different azimuths has to be created. This is the most time consuming part of the analysis.

   (b) A slope map of the DTM is calculated using a 3 x 3 pixels plane fit and assigning the local slope to the central pixel, compare Chapter 6.5.1

2. These steps have to be done at every time step (fast computation)

   (a) For each time step t and each pixel in the area of interest, the azimuth and elevation of the Sun is calculated using the DE421 ephemeris [Folkner et al., 2009] and SPICE routines [Acton, 1996].

   (b) The elevation of the horizon is compared to the elevation of the Sun in order to calculate the percentage of the visible solar disk. If necessary, the elevation of the horizon is computed through interpolation in the horizon maps.

   (c) By comparing the slope map (local normal vector) with the Sun vector the solar incidence angle can be calculated which is used for photo-realistic rendering of the scene.

Since the goal is to investigate landing sites near the lunar south pole in high-resolution, a DTM covering the south polar area is required. Although the area of interest might only cover a few kilometers close to the lunar south pole, the furthest point on the visible horizon from a random point on the Moon can be as far away as ∼200 km. A DTM in gnomonic projection is chosen for computational convenience, where straight lines in the map projection correspond to great-circle arcs on the sphere [Snyder, 1987]. The creation of the horizon maps in gnomonic space is then straightforward since lines originating at each pixel are great-circle arcs, hence the shortest distance between two points.

The elevation as seen from each pixel in a set of azimuthal directions is then calculated with the simple relation $arctan(\Delta h/s)$. Thereby, Δh is the height difference of a pixel on the line of sight to the observer pixel and s is the distance between the two. Obviously, distances measured in the map need to be corrected for the map distortion (gnomonic projection does not conserve distances). Also, the height differences need to be corrected for the curvature of the sphere. Introducing Cartesian coordinates and vector algebra, the elevation angle can easily be derived by the dot product between the position vector of the observer pixel and the vector from the observer to the observed pixel (Fig. 30).

A total of 720 horizon maps from 0°-360° in 0.5° steps are calculated. The step size of 0.5° is chosen because the solar disk has an diameter of ∼0.53° as seen from the lunar surface. This ensures that at least one azimuth direction of the 720 horizon maps lies within the Sun's angular diameter. Horizon maps for any azimuth angle can be derived by linear interpolation of two neighboring horizon maps.

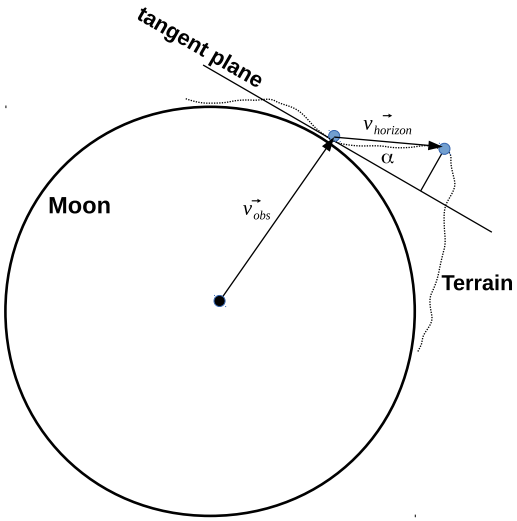

Figure 30: In this plot the elevation angle to the horizon as seen from an observer on the Moon is displayed. By using vector algebra, the distance distortion by the map projection as well as the height difference due to curvature is considered. $\vec{v}_{obs}$ is the vector from the center of the Moon to the observer, $\vec{v}_{horizon}$ is the vector from the observer to a location on the horizon and α is the corresponding elevation angle.

From the two horizon maps enclosing the solar azimuth, the fraction of the visible solar disk can be derived. A straight line connecting the two elevation angles at those horizon maps is drawn and the fraction of the solar disk above this line, which is the visible fraction of the Sun, is calculated. In Fig. 31 the calculation of the solar disk fraction is shown. Although the visible sun fraction is estimated assuming a linear horizon, the introduced error is negligible [De Rosa et al., 2012].

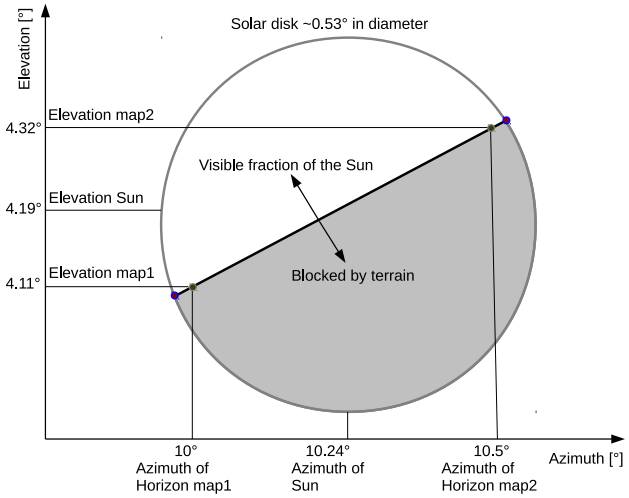

Figure 31: Calculation of the fraction of the visible solar disk.

To simulate available sunlight at a certain height above ground, e.g. a solar panel of a rover or a stationary lander, a height offset can be introduced in the analysis. Although realistic values for the height offsets might be small (e.g. 1-10 m) they can make a substantial

difference in Sun visibility. The Mars Science Laboratory (MSL) rover *Curiosity*, for instance, is equipped with the Mastcam imaging system operating ∼2 m above ground [Bell et al., 2012].

To evaluate illumination over time, a calculation step size of 1 h was chosen, during which the Moon rotates ∼0.5°, which corresponds to the azimuthal grid size. Thereby, it is ensured that no azimuth gaps occur where the Sun could be completely blocked or completely visible (Fig. 32). Accurate estimates of incoming sunlight, even just from a fraction of the Sun, may be of interest as this, for instance, will have an impact on the electrical output of a solar panel.

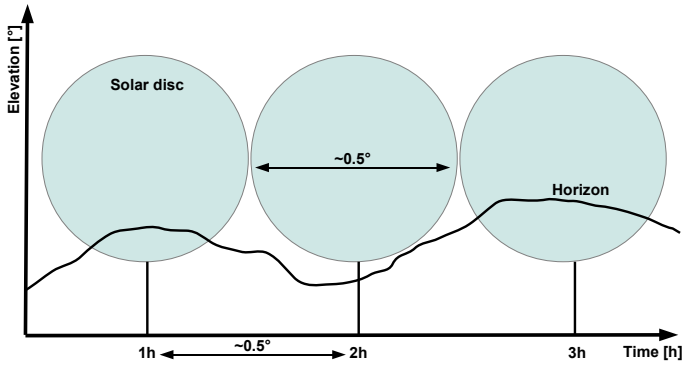

Figure 32: This sketch shows an example where the Sun is completely visible at t=2h whereas it was partly blocked 1 h before and after (t=1h and t=3h).

Temporal variations of illumination for each pixel in the area of interest can be derived by stacking the illumination maps created for each time step. Plots showing the illumination over time can be created, from which the longest continuous periods in light and darkness can be extracted. The beginning and the end date of these periods are also available and of interest for mission planning, e.g. when is the best time for a mission concerning illumination conditions. Further average illumination maps can be created, where points of maximum and minimum illumination can easily be found. Points of maximum illumination, for instance, are of interest for lunar landing sites and can be found and evaluated with help of these average illumination maps.

For comparisons with image data, we compute synthetic images. For simplicity, we adopt Lambertian shading, where surface brightness is proportional to the cosine of the incidence angle only (angle between the Sun vector and the surface normal vector). The computed surface brightness is then scaled by the fraction of the visible solar disk. For comparison, the NAC image is re-projected to match the geometry of the shaded DTM. This approach was used to render realistic scenes for validation purposes with NAC images (Chapter 7.2.4).

6.2.3 Example

Along the profiles originating from each pixel in the considered area and pointing in all 720 azimuthal directions, the maximum elevation angle is found as shown in Fig. 33. For

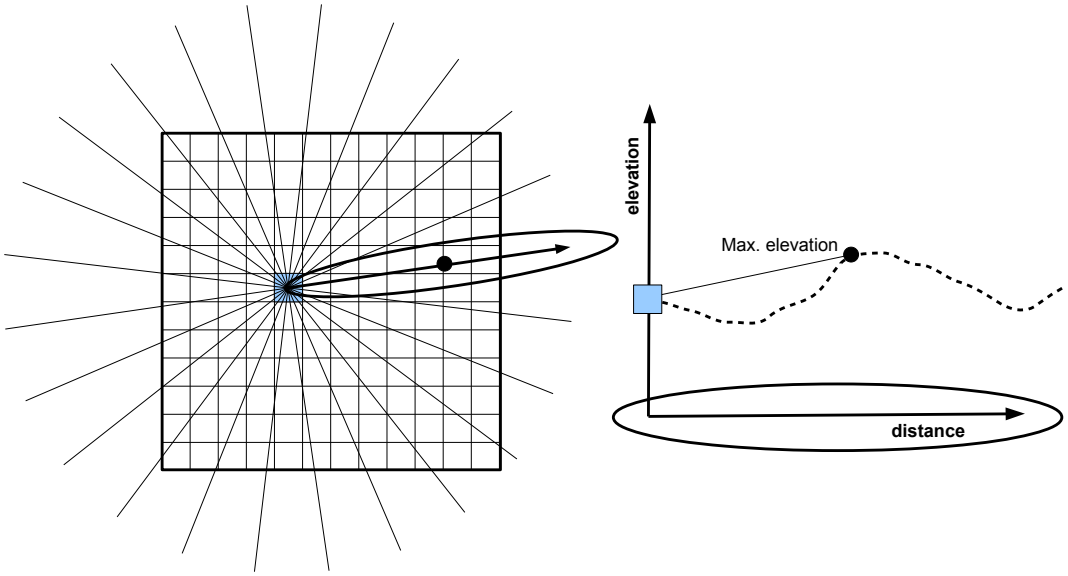

Figure 33: Left: From each pixel the maximum elevation in all 720 azimuthal directions is found. Right: Blow-up of the profile along one azimuthal direction and the location of the maximum elevation.

each azimuthal direction a data array is stored containing the maximum elevation in this very direction, see Fig. 34. Knowing the path and size of the solar disk, any point in time

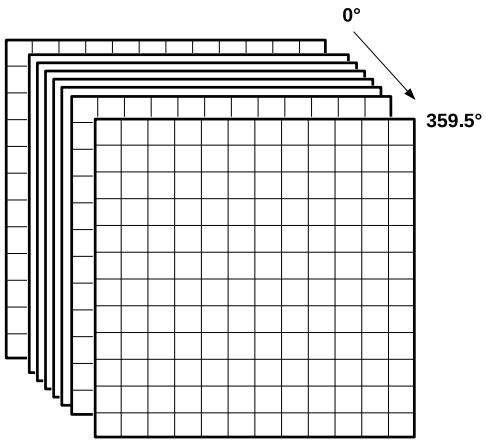

Figure 34: Each map only contains the maximum elevations for each pixel along the same azimuthal direction.

can be chosen to render a realistic image of the considered area, see Fig. 35.

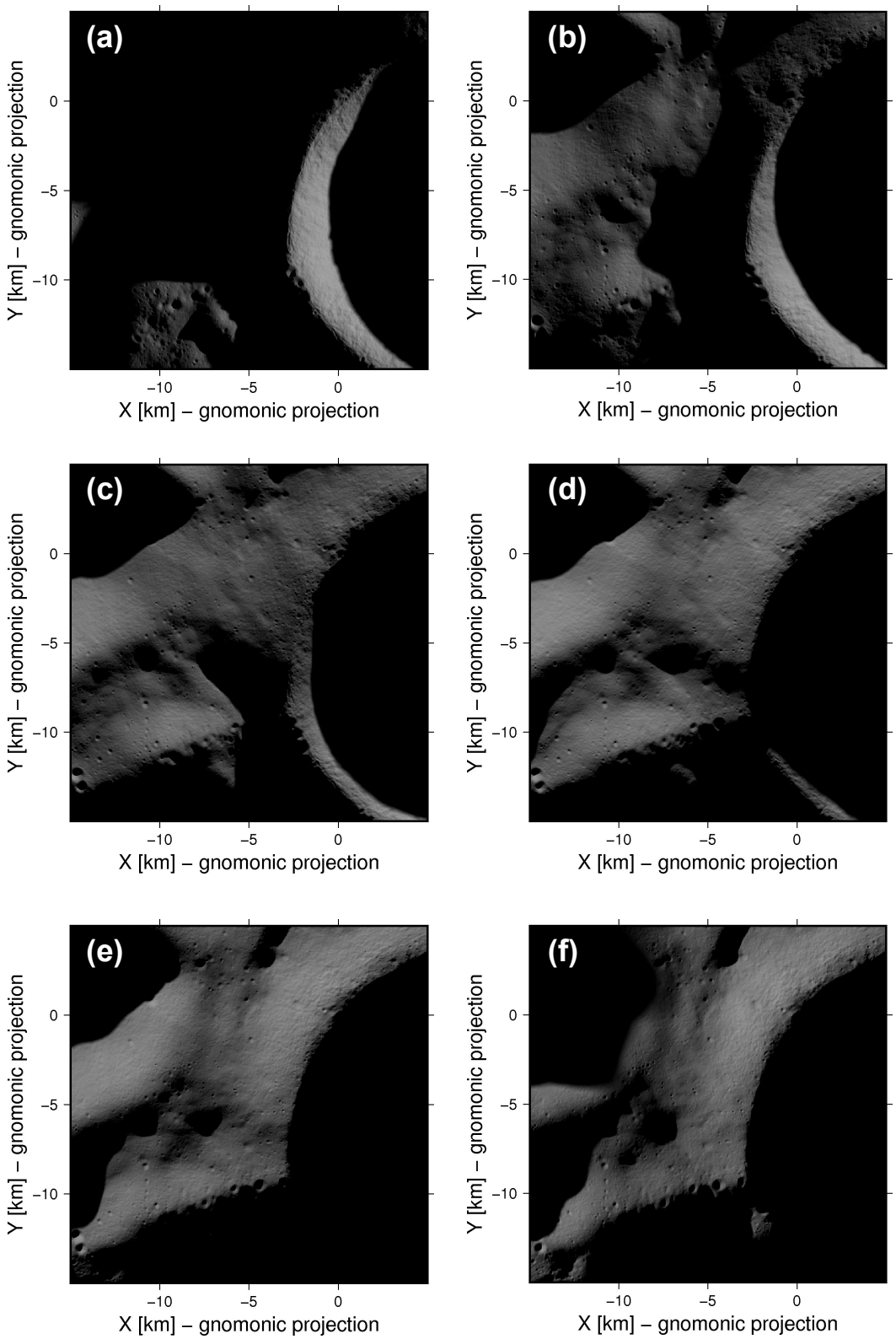

Figure 35: A sequence of rendered images (a)-(f) in gnomonic projection of an area around the lunar south pole is displayed. The time between successive synthetic images is 2 days, whereas the first image shows illumination conditions of May 9, 2019. Units are in kilometer.

6.3 Earth-visibility

An important parameter to determine whether a landing site is favorable regarding communication purposes, is the visibility of the Earth. In order to communicate from an Earth-based ground control center to a lander or rover at a south polar landing site, a direct line-of-sight between the two needs to be available. Since the Moon is in a synchronous orbit, and hence the same side is always facing Earth, a theoretical constant radio link of ∼12 h (<50% of an Earth day) for an observer on the nearside to a station on the Earth is feasible owing the rotation period of ∼24 h (neglecting the influence of the latitude of the lunar observer, the latitude of the Earth station and the season). However, observing a station on the Earth from a location near the lunar south pole, an overall visibility of <50% is expected due to the optical lunar libration in latitude of ∼6.68° (see Chapter 3.2).

In principle, the problem can be solved according to the method developed to determine illumination conditions as described in Chapter 6.2. Although the lunar local horizon is incorporated in the analysis (Earth's topography is neglected here), the effect on the result is rather small compared to the same analysis carried out for the Sun visibility (see Chapter 6.2). The reason is that the elevation of the Sun, as seen by an observer located close to the lunar south pole, is very low. The apparent up and down movement of the Sun has a 1-year period and approximately only varies due to the axis tilt with respect to the ecliptic plane of ∼1.54° (compare Fig. 59 but also the widths of the Sun's trajectory in Figs. 63 and 66). Hence, due to the glancing intersection of the Sun's trajectory with the local horizon, elevating a solar panel above ground will lead to longer illumination periods, compare Chapter 7.2.

The elevation of the Earth as seen from the lunar south pole, however, varies with a period of a lunar day and has an amplitude of ∼6.68° (see Chapter 3.2). As already mentioned earlier, this effect is called the optical lunar libration in latitude and consists of the sum of the axis tilt of ∼1.54° and the inclination of the lunar orbit plane with respect to the ecliptic of ∼5.145°. The resulting intersection angle between the Earth's trajectory and the local horizon is steep, and therefore, the lunar topography and the elevation of an observer above ground level will not have a large impact on the length of the Earth visibility period.

6.3.1 Example

Different orbital positions during a lunar revolution are investigated to demonstrate the changing scene for an observer close to the lunar south pole. In Fig. 36 the Moon is shown at its maximum height above the ecliptic (position I) and at its maximum height below the ecliptic (position II). Note, that the normal vector of the ecliptic (E) spans a plane with the lunar orbit normal vector (O) and the lunar rotational axis (R). For any time and position (E), (O) and (R) will span a plane and (E) will be between (O) and (R). This circumstance follows from Cassini's third law (Chapter 3.2.1). At position I

an observer near the lunar south pole sees the Earth at its highest possible elevation of 6.68° and at position II at its lowest elevation of -6.68°, where the Earth is now below the horizon and cannot be observed.

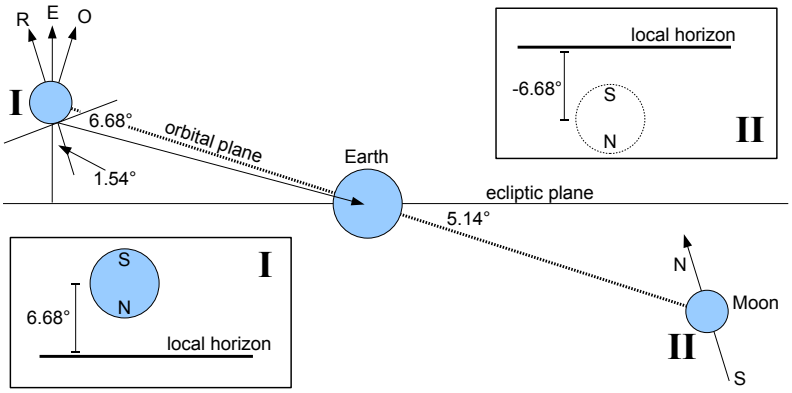

Figure 36: An observer at the lunar south pole observes the center of the Earth to be 6.68° (maximum) above the local horizon when the Moon is at position I. Similar, at position II, the Earth would be -6.68° (minimum) below the local horizon of an observer at the south pole and could not be observed.

In Fig. 37, the Moon and the Earth are in such a geometric constellation, that the Earth is just above or just below the local horizon of an observer at the lunar south pole. Assuming a circular orbit of the Moon around the Earth at a distance of 380.000 km, Earth's radius of 6.370 km always appears to be ∼1° for an observer on the Moon. Position III is found when the Moon is ∼1° above the ecliptic as seen from Earth and position IV accordingly ∼1° below the ecliptic.

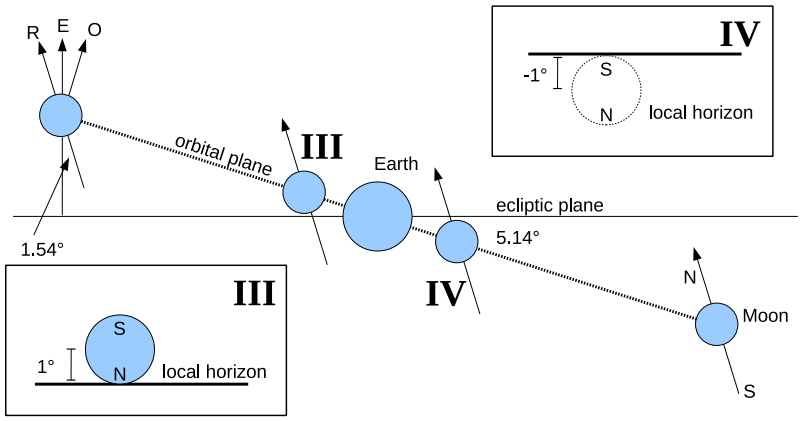

Figure 37: When the Moon is at position III the Earth is just above the local horizon as seen from an observer at the lunar south pole. Approximately 20° later in the lunar orbit, at position IV, the Earth is just below the local horizon.

This approximately occurs 10° before and after the line of nodes, see Fig 38. Between position III' - I - III (counting counterclockwise) the Earth is fully visible for an observer standing at the lunar south pole while between IV - II - IV' (counterclockwise) the Earth cannot be observed. In total the Earth is partially or completely seen for ∼200° of the

full circle, which is about 55.5%.

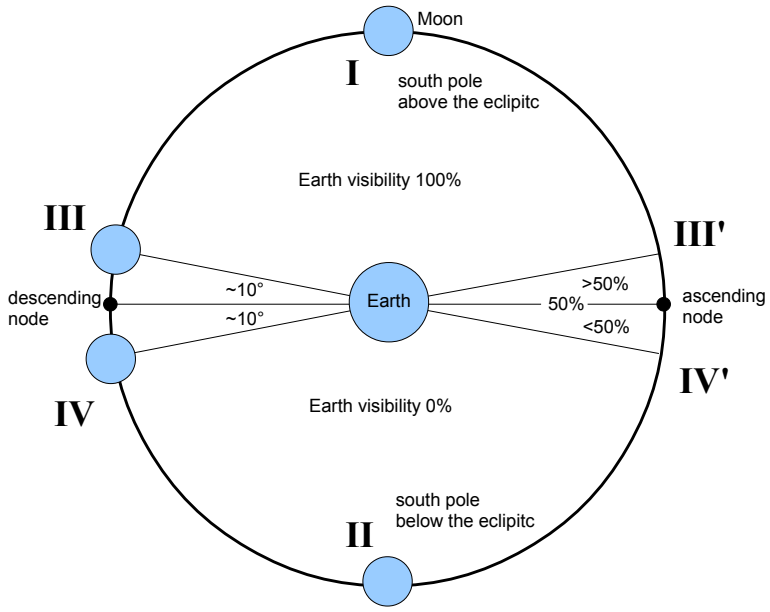

Figure 38: This plot shows the approximate positions of the Moon in its orbit around the Earth at positions I-IV.

In Fig. 39 the visibility of the Earth over one year, evaluated in 1 hour time steps is displayed. At locations that are not blocked by terrain the Earth is visible for up to ∼203 days of the year, which is 55.6% and was expected from conclusions drawn from the orbit geometry (see Figs. 36 - 38).

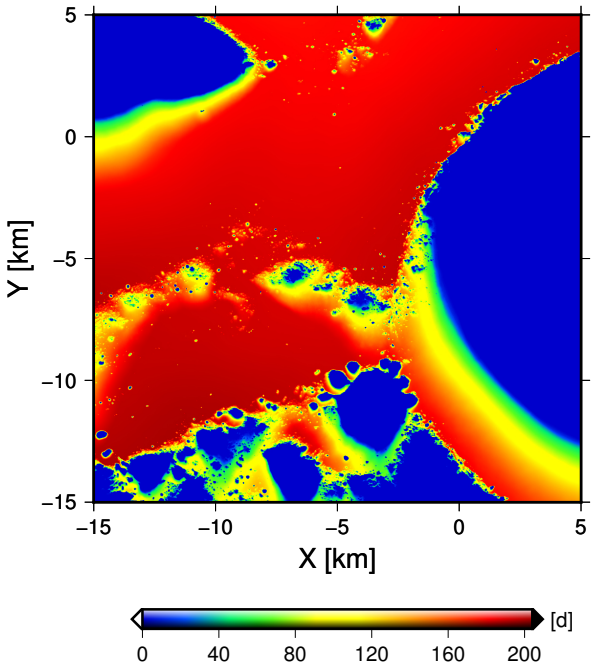

Figure 39: Earth-visibility over one year evaluated every hour is displayed for a region near the lunar south pole.

6.4 Slope and Roughness from LOLA data

In addition to Earth-visibility and illumination conditions at the landing site, parameters like slope and surface roughness are of great importance. These parameters help characterizing the full potential of a landing site regarding accessibility and exploration by a rover. One of the formulated objectives of LOLA is the *contribution to the assessment of meter-scale features to facilitate landing-site selection* (see Chapter 4.2, Chin et al. [2007]). Although LOLA is not measuring these parameters directly, there are methods to infer them from the primary measurements. Slopes, for instance, can be derived from either a gridded DTM or from individual LOLA spots (at least two) directly. Roughness values, for instance, can also be derived from gridded DTMs or individual LOLA spots (at least four) but also from pulse analysis of a single laser spot as well.

6.5 Previous work

Various techniques exist to measure surface roughness using different instrument data. For instance, images can be evaluated visually and rock statistics can be performed as a measure for roughness [Golombek et al., 2003b]. Thermal data can also be used to detect boulders and to infer roughness through rock statistics [Bauch and Hiesinger, 2012; Hayne et al., 2012]. Further, radar measurements can be related to surface characteristics by evaluating the so-called Circular Polarization Ratio (CPR) [Bussey et al., 2014; Patterson et al., 2014]. In this study, however, the focus is on roughness derived from laser altimeter data.

Kreslavsky and Head [2000] proposed the so-called median absolute value of differential slope or median differential slope as a measure of roughness for their study on Mars using MOLA data. Here, two points a half baseline ahead and half baseline behind the considered data point are selected and their signed elevation difference is calculated. Then, the signed elevation difference for two points located one baseline ahead and behind is calculated. The difference of the height differences of the smaller baseline and half the height difference of the larger baseline divided by the baseline itself is the differential slope. Let l be the chosen baseline, $h_{-l/2}, h_{l/2}$ and h_{-l}, h_l the height values at the given position with relation to the considered data point, then the equation for the differential slope is given by

$$\tan\alpha = \frac{(h_{l/2} - h_{-l/2}) - 0.5 \cdot (h_l - h_{-l})}{l} \tag{16}$$

In this approach larger-scale tilts related to height differences at twice the baseline are removed and only a corrected height difference at the basline l remains. The shortest possible baseline with MOLA data is ∼600 m since the along-track resolution of MOLA ground shots is ∼300 m [Smith and Zuber, 2000]. In their study Kreslavsky and Head [2000] evaluated baselines from 600 m to 20 km and found that different geological units have distinct roughness characteristics.

Rosenburg et al. [2011] showed global slope and roughness maps of the Moon derived from LOLA data. Besides one- and two-dimensional slope calculations, they also use the median differential slope proposed by Kreslavsky and Head [2000] to derive roughness maps at baselines ranging from 57 m to 1.4 km. A distinctive roughness value was found for the maria and the highlands, where the youngest flows like Oceanus Procellarum and Mare Imbrium only show roughness at smallest scales with increasing roughness at larger scales at older flows. The older lunar highlands are predominately rough at larger scales. Young craters, such as Copernicus are rough at all scales. Similar work regarding roughness on the Moon has been published by Kreslavsky et al. [2013].

The aforementioned techniques produce maps which are very useful in planetary geology in order to distinguish geological units, ages and processes. However, the baselines over which roughness is typically evaluated is on the range of the desired landing site ellipse of a future mission and does not satisfy required roughness constraints over lander-sized baselines. As previously shown by Neumann et al. [2003] for Mars using MOLA data, roughness within the laser footprint can be derived making use of the fact that rough terrain is spreading the laser pulse width. First results for footprint-sized roughness on the Moon derived from LOLA data were shown and discussed by Neumann et al. [2011, 2009] and Smith et al. [2011b, 2012].

6.5.1 Slope

Slopes describe the height difference of the terrain over a certain distance. The parameter *slope* is therefore always dependent on the baseline used, which in general is the distance over which the slope is measured. In a one-dimensional example, where Δh is the height difference over the baseline d, the slope α is

$$\alpha = \arctan \frac{\Delta h}{d}. \tag{17}$$

For a one-dimensional slope calculation LOLA offers a variety of options owing to the x-shaped pattern of the five spots for each shot. Both directions, along-track and cross-track, can be calculated separately. In Fig. 40, several possibilities to calculate a slope value for spot 5 are shown. Where previous laser missions only allowed for the derivation of a one-dimensional slope value in along-track direction, LOLA is offering a wide range of possible slope calculations. In a similar manner, slopes between any two pixels can be derived from a gridded LOLA DTM. Since two-dimensional slopes can be derived using LOLA and are of higher interest for this study, the approach to calculate one-dimensional slopes is not used further on.

A two-dimensional slope estimate can be derived by spanning a plane through several LOLA spots (at least three) and retrieving the inclination of that plane to the local tangential plane. Also, a preferably square patch of pixels from a gridded LOLA DTM can be used to infer slopes through plane fitting. In practice, the slope α is calculated by the dot product of the normal vector of the plane, $\boldsymbol{n_p}$, with the normal vector of the tangential

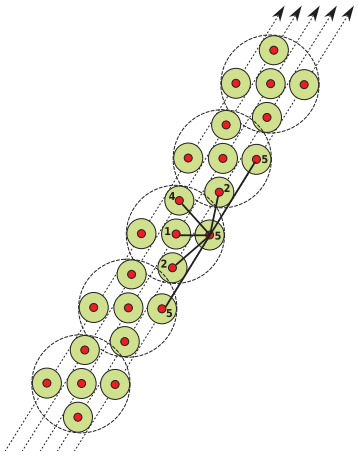

Figure 40: Possible slope calculations for spot 5 from surrounding laser spots

plane, $\boldsymbol{n_t}$, see Eq. 23. The analysis using multiple regression and least-squares techniques is shown exemplarily for three LOLA spots $P_1(x_1, y_1, z_1)$, $P_2(x_2, y_2, z_2)$, $P_3(x_3, y_3, z_3)$ in Eqs. 18 - 23. Vectors and matrices are shown in bold letters.

$$\begin{aligned} z_1 &= a + b \cdot x_1 + c \cdot y_1 \\ z_2 &= a + b \cdot x_2 + c \cdot y_2 \\ z_3 &= a + b \cdot x_3 + c \cdot y_3 \end{aligned} \tag{18}$$

$$\boldsymbol{l} = \begin{pmatrix} z_1 \\ z_2 \\ z_3 \end{pmatrix} \tag{19}$$

$$\boldsymbol{A} = \begin{pmatrix} 1 & x_1 & y_1 \\ 1 & x_2 & y_2 \\ 1 & x_3 & y_3 \end{pmatrix} \tag{20}$$

$$\boldsymbol{x} = (\boldsymbol{A^T} \cdot \boldsymbol{A})^{-1} \cdot \boldsymbol{A^T} \cdot \boldsymbol{l} = \begin{pmatrix} a \\ b \\ c \end{pmatrix} \tag{21}$$

$$\boldsymbol{n_p} = \begin{pmatrix} b \\ c \\ -1 \end{pmatrix} \tag{22}$$

$$\alpha = 90 - \arccos \frac{\boldsymbol{n_p} \cdot \boldsymbol{n_t}}{|\boldsymbol{n_p}| \cdot |\boldsymbol{n_t}|} \tag{23}$$

Eq. 18 shows three equations of the plane that must be satisfied. Each equation is made up by one of the three LOLA spots P_1, P_2, P_3 and contains three unknowns a, b, c. The z-component of the plane's normal vector $\boldsymbol{n_p}$ is set to -1. The x- and y-component of $\boldsymbol{n_p}$ are represented by the unknowns b, c. The observation vector $\boldsymbol{l}$ contains the z-components of the LOLA spots and the Jacobi matrix $\boldsymbol{A}$ is calculated by taking the partial derivatives of Eq. 18 to the unknown parameters. The vector of the adjusted unknowns $\boldsymbol{x}$ contains the estimates for a, b, c.

Due to the anomaly, which occurs when LRO crosses the terminator and stays effective over the entire night side (see Chapter 5.2.3), only spot 3 and 4 will be monitored. Here, one LOLA shot will only deliver two valid spots, but at least three spots are needed for the slope calculation. To derive a two-dimensional slope for the LOLA tracks on the night side, at least two successive shots are needed to calculate a plane. However, to automatically calculate slopes for the entire LOLA dataset, three successive shots are selected to infer a local plane and the derived slope is then attached to the 5 shots of the middle spot (Fig. 41). This approach ensures ∼6 spots on the night side and up to ∼15 spots on the day side of the LOLA tracks and also allows for the derivation of a standard deviation (possible if more than three spots span a plane). Hence, the resulting slope values are related to a baseline of ∼150 m.

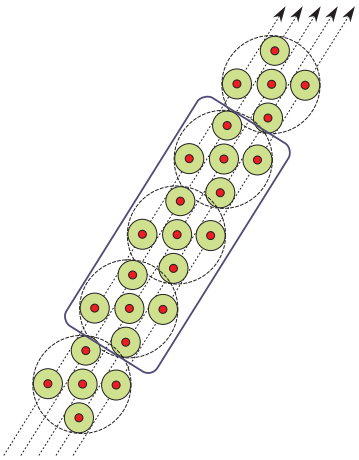

Figure 41: Plane fit over 3 successive shots

6.5.2 Roughness

Surface roughness can be described over a wide range of scales. Similar to slopes, however, it is directly dependent on the baseline used and meaningless without it being mentioned. Any deviation from a reference surface, e.g. a plane, can be interpreted as roughness. This value can be derived from the plane fits as described in Chapter 6.5.1. Another approach leads to an estimate for roughness within a single laser spot. This is feasible since LOLA is not only measuring distances but also records pulse widths of incoming laser pulses, which can be related to surface roughness. These measurements provide information within footprint (5 m) scales, crucial for safe landing and surface mobility.

Sigma-Z approach One approach to determine roughness is the calculation of the standard deviation σ of the plane fits as mentioned in Chapter 6.5.1. Here, x_i are the

single LOLA spots, $\overline{x}$ represents the plane and n is the number of spots.

$$\sigma = \sqrt{\frac{1}{n-3} \cdot \sum_{i=1}^{n} (x_i - \overline{x})^2}. \tag{24}$$

This parameter describes the deviation of the LOLA spots to the fitted plane, see Fig. 42.

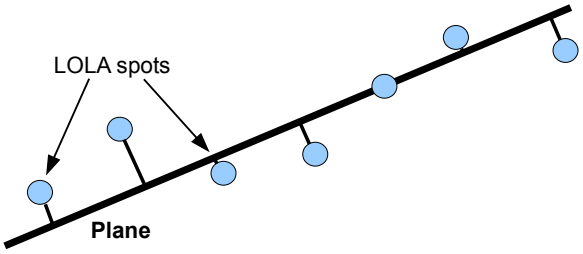

Figure 42: The standard deviation describes the deviation of the single LOLA spots to the plane and serves as an estimate for surface roughness.

Pulse width approach This paragraph explains the evolution of a laser pulse and the measured parameters needed to derive roughness estimates from laser pulse width measurements. As previously shown by Neumann et al. [2003] for MOLA data, the recorded laser pulse width can be used to infer a roughness value of the terrain within footprint scales. The general concept behind this idea is that when a pulse bounces off a surface its shape changes. This change in shape is correlated to the tilt and roughness of the reflecting terrain. A pulse, however, reflected on a flat and not sloped surface preserves its shape (Fig. 43 - top). By tilting the flat surface, the pulse shape of the reflected pulse will have a wider pulse width than the original pulse (Fig. 43 - middle). Furthermore, any surface that is not flat over the baseline of the laser footprint (LOLA ∼5 m), is referred to as a rough surface and will spread the pulse width in the same manner as a flat but sloped surface (Fig. 43 - bottom). For typical laser footprints of several meters any surface will most likely be rough or sloped or both at the same time.

A transmitted and then reflected LOLA pulse is eventually received back at the telescope where it is then amplified by a Variable Gain Amplifier (VGA). The amplification is done in a way that ensures that the receiver electronics will not be saturated, and therefore artificially alter the waveform. For instance, the MOLA altimeter on-board MGS had a fixed gain amplifier and lead to 400 million saturated returns which represent two third of all successfully returned 600 million range measurements [Neumann et al., 2003].

To distinguish the laser pulse from background noise, a variable detection threshold is automatically selected by an on-board algorithm to adapt to the actual situation, see also Fig. 13. Such variable thresholds are of high importance since background noise is not a constant quantity. Background noise is related to the reflection of sunlight from the lunar surface as well as the solar phase angle. The noise level varies within every orbit from

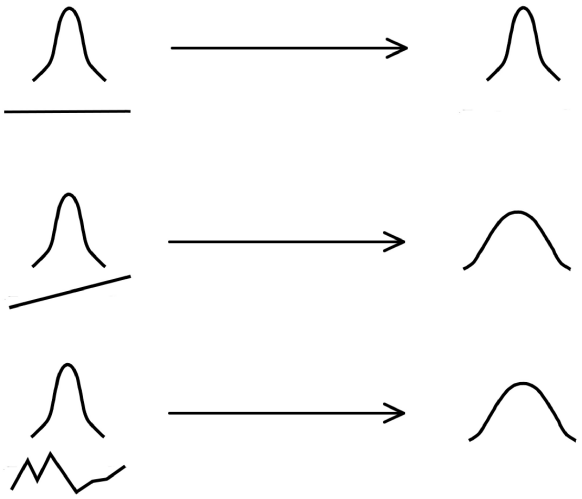

Figure 43: (top) A flat surface reflects the Gaussian packet without spreading. (middle) A sloped surface results in pulse spreading. (bottom) A rough surface also results in pulse spreading.

the day to night side, with the different surface reflectivity of e.g. mare and highlands as well as with the revolution of LRO's orbital plane around the Sun. The intersection of the rising pulse with the detection threshold level is referred to as leading edge and the dropping of the pulse below the threshold is referred to as trailing edge. The time interval between the two crossings is the pulse width at detection threshold level. An integrator is recording the energy of the pulse between the leading and trailing edge of the pulse and together with the pulse width at threshold level all parameters to constrain the shape of a Gaussian pulse are observed [Abshire et al., 2000; Neumann et al., 2003].

Nominal transmitted pulse At ground calibration tests the transmitted LOLA pulse was measured by a high speed photo detector and oscilloscope to investigate the actual transmitted pulse shape. It was found that the shape of a LOLA pulse can be approximated by a Gaussian function. The pulse width varies between 4.3 and 4.9 ns Full Width Half Maximum (FWHM) and can be best described with a pulse width at FWHM of 4.6 ns [Riris et al., 2010](Chapter 7.7 Page c-40).

The general mathematical description of a Gaussian pulse as a function of time is

$$f(x) \quad = \quad \frac{A}{\sigma \cdot \sqrt{2\pi}} \cdot e^{-\frac{t^2}{2 \cdot \sigma^2}} \tag{25}$$

in which A is the pulse area, σ is the pulse width in nanoseconds, e is the Euler number and t is time. The transmitted LOLA pulse is modeled with a pulse width of 4.6 ns at FWHM and a transmit pulse energy of ∼3 mJ (Fig. 44). The following equation relates FWHM to σ [Abshire et al., 2000]

$$FWHM \quad = \quad \sigma \cdot 2.3548 \tag{26}$$

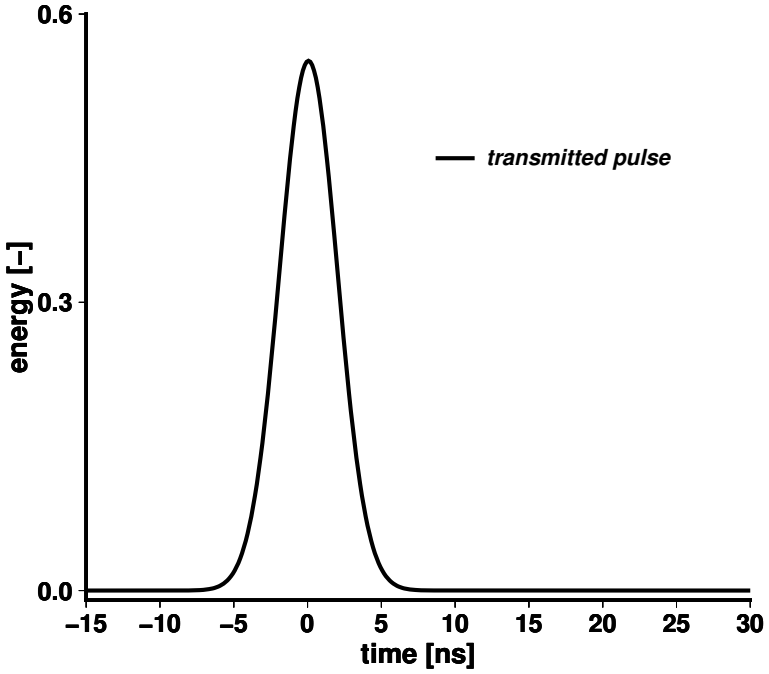

Figure 44: The outgoing laser pulse at the transmitter is assumed to be a Gaussian pulse

External effects - Surface interaction The parameter describing the laser beam divergence is referred to as angle γ. The laser beam full divergence angle γ_x is an angular measure in *rad* referenced to the $\frac{1}{e^2}$ ($\sim$13.5% of maximum irradiance) intensity point. For LOLA γ_x is $\sim$100 μrad which results in a 5 m footprint on the surface from a 50 km orbit [Riris et al., 2010](Chapter 7.1 Page c-34). The RMS laser beam divergence half angle (measured at $\frac{1}{\sqrt{e}}$), which will be used in the analysis, can be calculated as described in Abshire et al. [2000].

$$\gamma \quad = \frac{\gamma_x}{4} \tag{27}$$

For LOLA, γ is $\sim$25 μrad which represents a footprint of $\sim$1.25 m. To account for sloping terrain, the slope θ within the laser footprint has to be known. As described in Chapter 6.5.1, previous laser missions could only derive a one-dimensional slope in along-track direction due to a single spot laser. LOLA is the first planetary laser altimeter to measure a two dimensional area per shot and allows for the derivation of a two dimensional slope estimate.

The actual received laser pulse depends on various effects [Gardner, 1982]:

$$\sigma_{rx}^2 \quad = \quad \sigma_x^2 + \sigma_{resp}^2 + \sigma_{slope}^2 + \sigma_{curve}^2 + \sigma_{rough}^2 \tag{28}$$

The pulse spreading due to the surface slope is described by (Fig. 43 - middle)

$$\sigma_{slope} \quad = \quad \frac{2 \cdot R}{c} \tan\gamma \tan\theta \tag{29}$$

σ^2_{rx}	:	Received pulse width
σ^2_{x}	:	Transmitted pulse width
σ^2_{resp}	:	Impulse response
σ^2_{slope}	:	Slope effect on pulse width
σ^2_{curve}	:	Laser beam divergence effect on pulse width
σ^2_{rough}	:	Terrain effect (roughness within laser footprint) on pulse width

Measured, known values	σ^2_{rx}, σ^2_{x}, σ^2_{resp}
Calculated values	σ^2_{slope}, σ^2_{curve}
Unknown value	σ^2_{rough}

where R is the one-way laser range in meter and c is the speed of light, given in m/ns. The effect on the pulse width due to the laser beam curvature depends on the RMS laser beam divergence half angle γ and is given by

$$\sigma_{curve} = \frac{2 \cdot R}{c} \tan^2 \gamma \tag{30}$$

In the case of LOLA the influence of the laser beam curvature on the pulse width spread is on the order of 200 femto-seconds and can be neglected.

Rough terrain broadens the laser pulse due to surface height variations within the laser footprint (Fig. 43 - bottom). A variation of X meters within the laser footprint, e.g. a boulder, would cause a signal delay of $2 \cdot X/c$ ns. Consider a boulder with height $X =$ 0.3 m. Since the signal bounces back from the top of the boulder 0.3 m before the signal from the surrounding surface, a total path difference of $2 \cdot 0.3$ m = 0.6 m is measured. The effect is therefore modeled as

$$\sigma_{rough} = \frac{2 \cdot X}{c}. \tag{31}$$

Modeling all non-electronic, external effects on the laser pulse, the reflected pulse has a wider pulse width compared to the transmitted pulse. The σ_{ext} of the laser pulse with only external influences modeled is

$$\sigma^2_{ext} = \sigma^2_{x} + \sigma^2_{slope} + \sigma^2_{curve} + \sigma^2_{rough} \tag{32}$$

Using σ_{ext} in the Gaussian pulse (Eq. 33) pulse spreading as shown in Fig. 45 can be observed

$$f(x) = \frac{A}{\sigma_{ext} \cdot \sqrt{2\pi}} \cdot e^{-\frac{t^2}{2 \cdot \sigma^2_{ext}}} \tag{33}$$

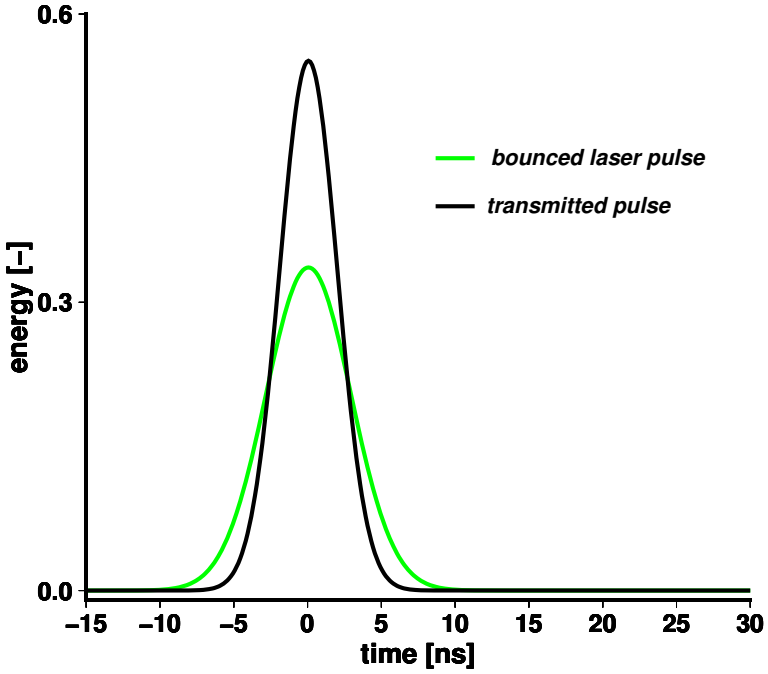

Figure 45: The reflected laser pulse has been spread by external effects

Internal effects - Impulse response As described in the LOLA calibration document [Riris et al., 2010](Chapter 4.1.2 Page c-19), the impulse response can be modeled as a low-pass filter or 5-pole Butterworth filter. It describes the response of the system to the incoming pulse. In this work a RC low pass filter (Fig. 46) with R = 50 Ohm (electrical resistance) and C = 68 pFarad (capacitance) and $\tau = R \cdot C$ was used [Riris et al., 2010]. h(x) is the Heaviside step function which is equal to zero for negative arguments and one for positive arguments, t is time and e is the Euler number.

$$h(x) = \begin{cases} 1, & x < 0 \\ 0, & x \geq 0 \end{cases} \tag{34}$$

$$g(x) = \frac{1}{\tau} \cdot e^{\frac{-1}{\tau}t} \cdot h(x) \tag{35}$$

In a mathematical sense, the result is the convolution of the incoming pulse with the exponential decaying function of the impulse response. This function can either be evaluated analytically or numerically using a discrete convolution.

Measured pulse width The convolution of the reflected pulse f(x), Eq. 33, and the exponentially decaying function describing the impulse response g(x), Eq. 35, yields to the function y(x), graphically displayed Fig. 46. The output y(x) is also dependent on the detector responsivity which is the product of the quantum efficiency of each individual detector, η_{APD}, the gain of the APD, G_{APD}, and the gain of the buffer, G_{Buffer}, and VGA, G_{VGA} [Riris et al., 2010](Chapter 8.3 Page c-46,c-47).

$$\text{Responsivity} = \eta_{APD} \cdot G_{APD} \cdot G_{Buffer} \cdot G_{VGA} \tag{36}$$

$$\eta_{APD} \cdot G_{APD}[1:5] = [3.1, 3.4, 3.1, 3.4, 3.2] \cdot 10^5 \frac{V}{W} \tag{37}$$

$$G_{Buffer} \cdot G_{VGA} \approx 50 \cdot 10^{-6} \tag{38}$$

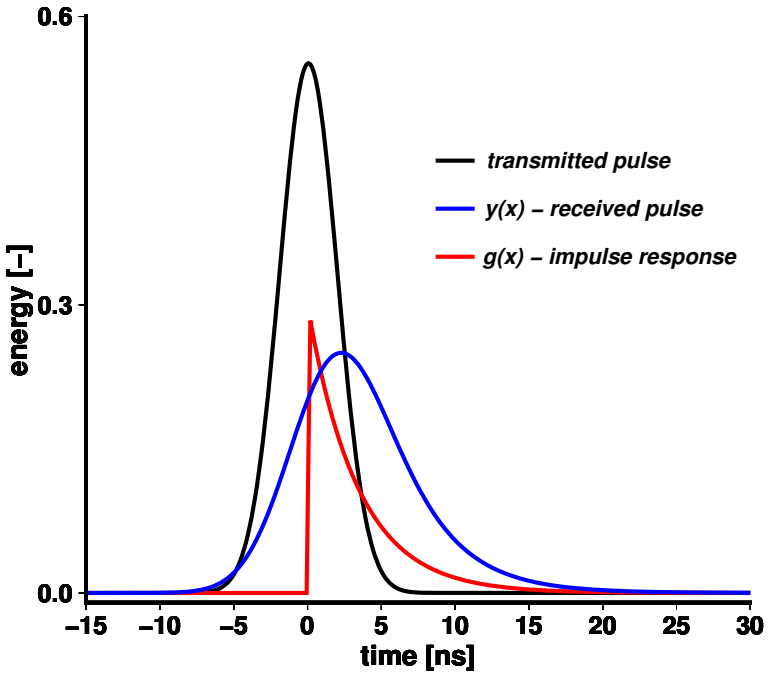

Figure 46: The final pulse output y(x), the received pulse. Note the substantial spread due to surface and electronic interactions of the received pulse to the transmitted pulse.

The width of a pulse is typically given at FWHM or σ but the measurement of the pulse in the electronics, however, is taken at threshold level. In the case of LOLA the threshold level is a variable parameter and has to be accounted for in the model (Fig. 47). The received pulse width can now be measured by taking the time difference between the two threshold crossings of the pulse. The effect of a hysteresis varies the threshold level from the crossing of the leading edge to the crossing of the trailing edge. The measurement of the received pulse width at threshold level can be transformed into a RMS pulse width

σ_{rx} by the relation

$$\sigma_{rx} = \frac{0.5 \cdot W_y}{\sqrt{2}} \cdot [z^{-1}(\frac{A_y}{y \cdot W_y})]^{-1} \quad (39)$$

$$x = \frac{A_y}{y \cdot W_y} \quad (40)$$

$$z^{-1} = 0.1716 + 4.9319 \cdot \log x - 11.693 \cdot (\log x)^2 + 18.886 \cdot (\log x)^3 - 16.696 \cdot (\log x)^4 + 7.4269 \cdot (\log x)^5 - 1.2997 \cdot (\log x)^6 \quad (41)$$

W_y is the pulse width in ns at the threshold level y. The area above y enclosed by the pulse is denoted by A_y, the energy above threshold level.

Solving Eq. 28 for σ_{rough} leads to

$$\sigma^2_{rough} = \sigma^2_{rx} - \sigma^2_x - \sigma^2_{resp} - \sigma^2_{slope} - \sigma^2_{curve} \quad (42)$$

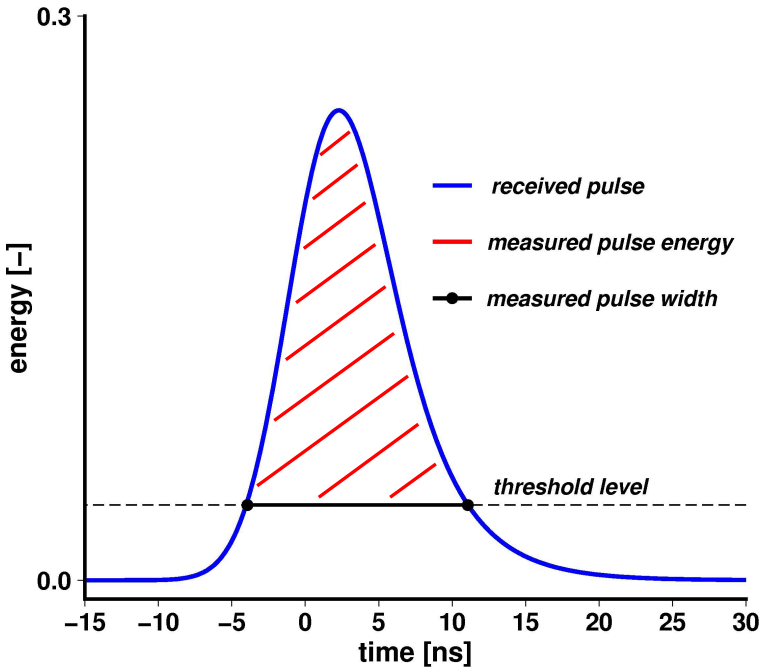

Figure 47: LOLA measures the pulse width W_y at threshold level y. The area above y is the pulse energy A_y.

7 Results

All results relevant for the characterization of lunar landing sites are summarized in the following sections. First, the derivation of an adjusted south polar DTM is shown using the method of co-registration as described in Chapter 6.1. Building upon the derived DTM, illumination conditions and Earth-visibility maps are derived following the techniques introduced in Chapters 6.2 and 6.3. Further, slope and roughness maps are shown, which are produced according to methods described in Chapters 6.5.1 and 6.5.2. Lastly, a section connecting all results derived in the scope of this work are displayed together.

7.1 Adjusted LOLA DTM

As mentioned in Chapters 1 and 6, the goal of this work is the evaluation and characterization of landing sites at the lunar south pole. The base for many scientific results attained in this work is a south polar DTM derived from LOLA data. Although the LOLA instrument measures distances with a ranging accuracy of 10 cm (see Chapter 5.2.1 and [Smith et al., 2010a]), the accuracy of the LRO spacecraft position is estimated to be ∼7-12 m RMS [Mazarico et al., 2013]. The resulting positional accuracy of a laser track on the lunar surface, however, can be less accurate than LRO's position, e.g. depending on the accuracy of the attitude of the spacecraft (see Chapter 5.2.1). When creating DTMs with pixel resolutions less than 25 m per pixel, artifacts due to orbit reconstructions are still visible [Mazarico et al., 2012a] and further refinement is necessary.

The co-registration method, as introduced in Chapter 6.1, was used to refine LOLA tracks and to create an adjusted 400 x 400 km DTM at the lunar south pole (see Fig. 53f). As a starting point, a NAC DTM at the Connecting Ridge, a ridge close to the south pole connecting de Gerlache crater and the Shackleton crater, is required [Gläser et al., 2013b]. The NAC DTM was produced and provided by DLR. The NAC DTM covers an area of about 2 x 2 km at a pixel resolution of 2 m and is displayed in Fig. 48. Due to large shadowed areas at the poles, especially in craters, no spatial information can be derived for these areas which results in data gaps within the DTM (see Chapter 5.3.3).

7.1.1 Step 1 - Co-registration of LOLA with NAC DTM

First, all LOLA tracks that intersect the area of the NAC DTM are selected (see Fig. 49a). Discrepancies between the tracks become visible as stripes and single offset LOLA spots occur as speckle, when a DTM is created with these nominal LOLA tracks (see Fig. 49b). Nevertheless, all data gaps appearing in the NAC DTM can be observed with LOLA due to the active sending and receiving of laser pulses, independent of sunlit or shadowed regions.

In total, 876 tracks containing ∼100,000 spots intersected the NAC DTM at the time of creation (August 2013). As described in Chapter 6.1, the co-registration algorithm

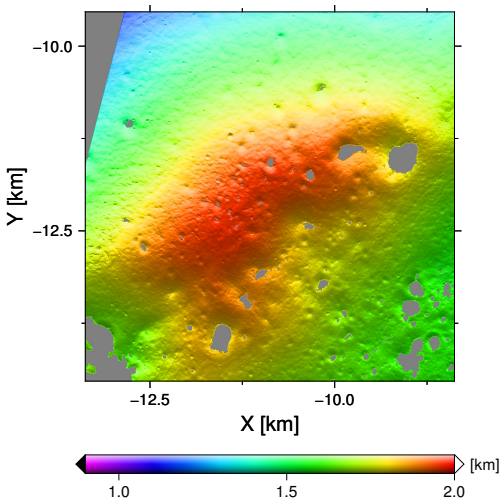

Figure 48: A 2 x 2 km NAC DTM at the Connecting Ridge with a 2 m per pixel resolution is shown. The data gaps are due to shadowed regions, mostly crater floors, where the derivation of spatial data with stereo techniques is impossible. ©DLR

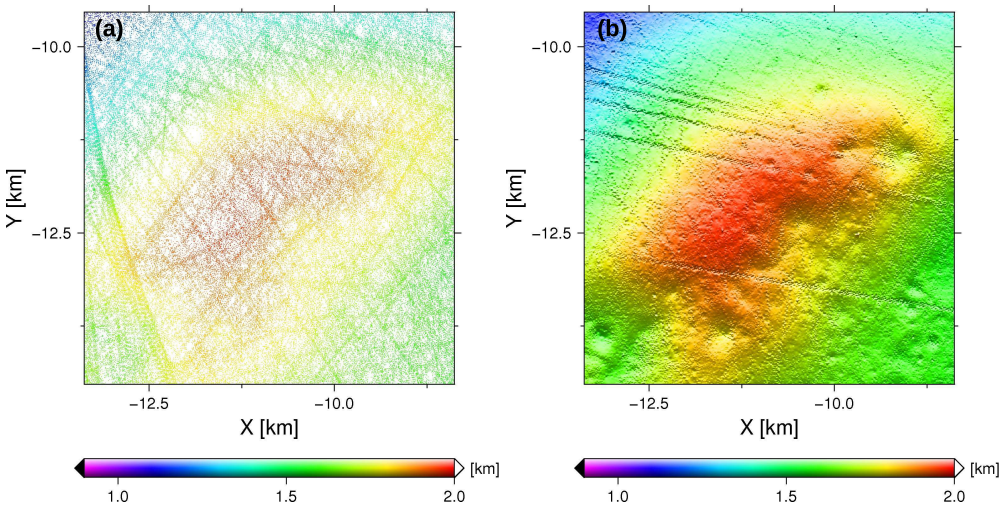

Figure 49: (a) All LOLA tracks that intersect the area covered by the NAC DTM are displayed. (b) A DTM (5 m per pixel) created from this LOLA data set is shown. The displacements between the LOLA tracks and speckle introduced by single offset spots are clearly visible.

estimates the correct position of LOLA tracks on the NAC DTM and also provides accuracy values for each fit. The resulting LOLA DTM, after the co-registration, is shown in Fig. 50a.

The standard deviations of the fit between the data sets in x, y, z-direction, can help detect outliers or erroneous tracks. Other parameters like the minimum amount of matched spots, maximum single height offset of a LOLA spot to the NAC DTM or the standard deviation of height residuals over the whole LOLA track compared to the NAC DTM can also be used as filter settings. Hence, a filtering of the co-registered data set is feasible which leads to the final, co-registered and filtered LOLA DTM as shown in Fig. 50b.

In total, 454 tracks containing ∼90,000 spots were co-registered and passed the filtering.

Although only 50% of the actual LOLA tracks, 454 out of 876 tracks, contribute to the final DTM, the percentage of final LOLA spots amounts to 90% of the original spots. The 50% loss in LOLA tracks (but only 10% in spot data) can partly be explained by the proximity to the lunar south pole, were all LOLA tracks converge due to LRO's polar orbit. Consequently, some tracks may only intersect the NAC DTM at the corners where too few spots can be used for co-registering. Another effect is the LOLA anomaly, see Chapter 5.2.3, resulting in many sparse tracks at the poles which are also discarded from the analysis if too few spots can be co-registered.

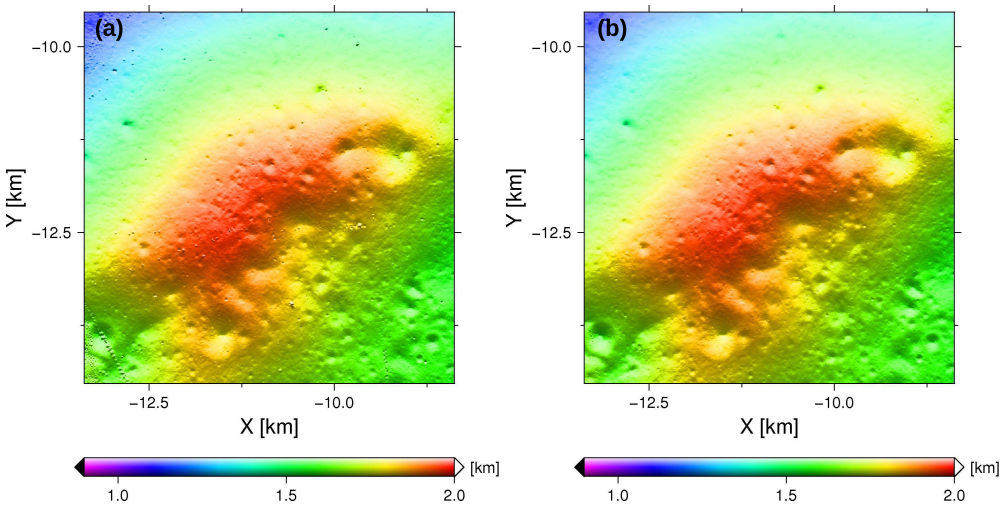

Figure 50: (a) A DTM with 5 m pixel resolution, created from co-registered LOLA tracks is displayed. (b) After filtering, the final LOLA DTM (5 m per pixel) is free of erroneous tracks and speckle.

7.1.2 Step 2 - Extending the area

An adjusted LOLA DTM covering the same area as the NAC DTM is now available. The co-registered and filtered LOLA tracks were originally cut to fit the extent of the NAC DTM (see Fig. 49a). Assuming though, that the applied shifts to each track are also valid for parts of the track that were not directly intersecting with the NAC DTM, the former area which was defined by the size of the NAC DTM can be extended.

Hence, all tracks are now plotted on an area about nine times bigger than the NAC DTM (see Fig. 51a). The size of the new area was chosen manually in a way that gaps between diverging tracks can still be interpolated reasonably well (interpolation results were validated visually). The interpolated DTM is shown in Fig. 51b. Although some parts in the DTM have substantial areas interpolated as almost flat surfaces, the co-registration method will still lead to meaningful results as seen in the final product (Fig. 52). The DTM displayed in Fig. 51b is now co-registered with all LOLA tracks that intersect the extended area (not shown). The resulting DTM, referred to as DTM_EV1 (extended version 1), is shown in Fig. 52. Note, that areas formerly interpolated as flat surfaces are now filled

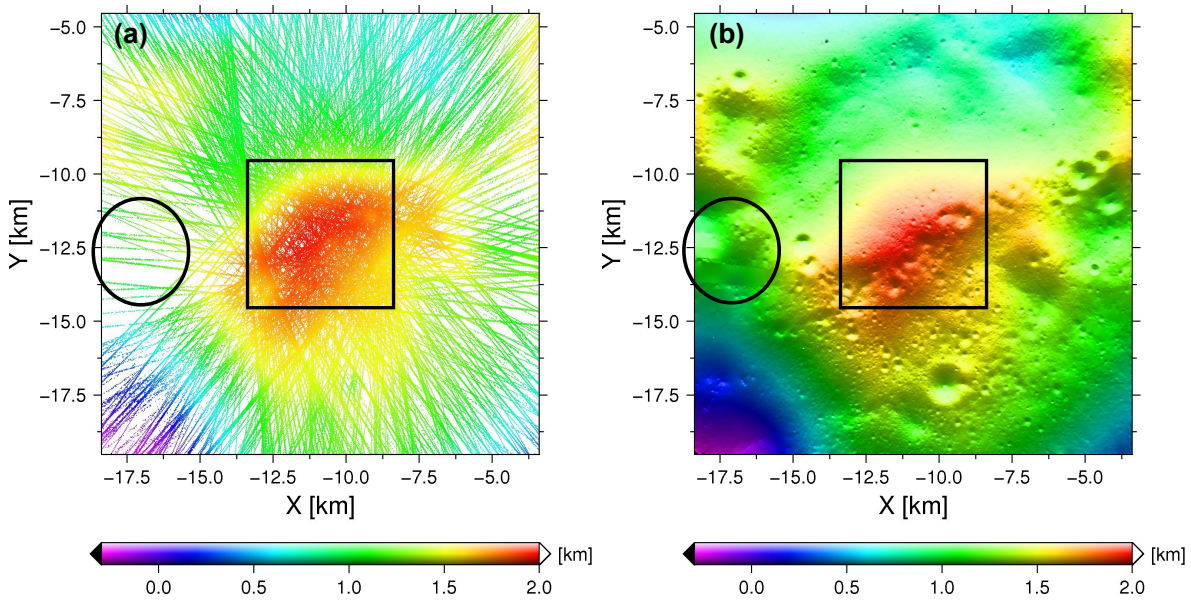

Figure 51: (a) All LOLA tracks that cover nine times the area of the NAC DTM are displayed. (b) A DTM (5 m per pixel) created out of this LOLA data set is shown. Large gaps between LOLA tracks (a), highlighted by a black ellipse, result in flat interpolated areas in the resulting DTM (b). A black rectangle indicates the size and location of the NAC DTM.

with data from intersecting LOLA tracks (compare Fig. 51b and Fig. 52).

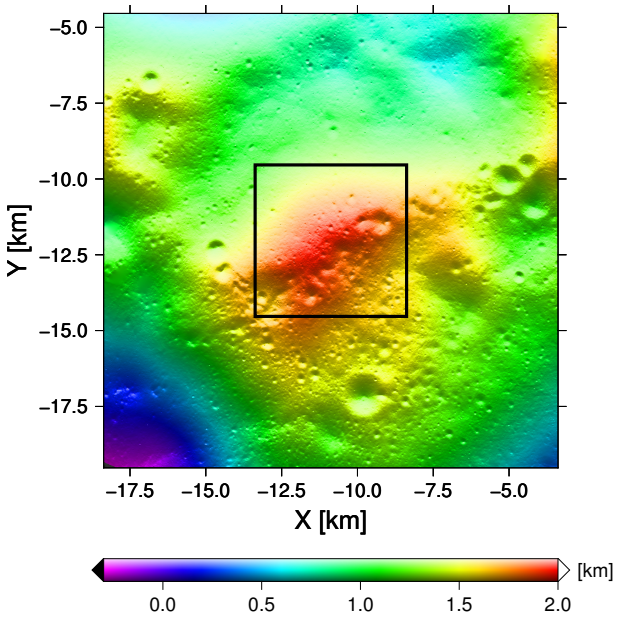

Figure 52: The final DTM_EV1 after co-registering all LOLA tracks intersecting the extended area. A black rectangle indicates the size and location of the NAC DTM.

DTM_EV1 serves now as the new base DTM and step 2 is looped. The final extended versions of several stages are displayed in Fig. 53.

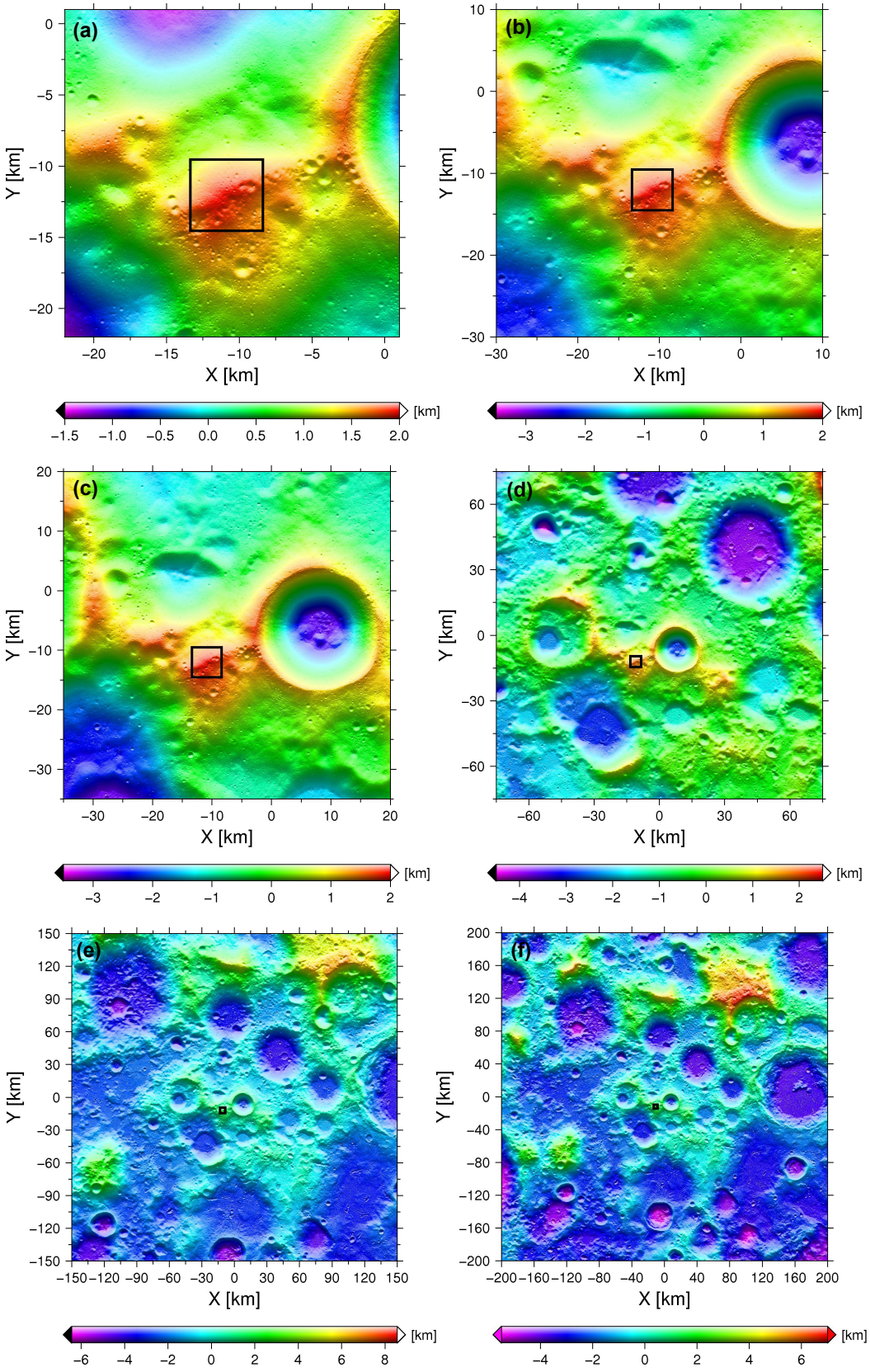

Figure 53: Several extended versions (a)-(e) and the final adjusted 400 x 400 km LOLA DTM (f) are displayed in gnomonic projection. The DTMs shown in (a)-(c) have a 5 m pixel resolution and (d)-(f) are shown in 20 m pixel resolution. The black rectangle shows the original size of the NAC DTM. Note the continuous change of the color bars, which represent height.

7.2 Illumination

The analysis concentrates on the evaluation of illumination conditions near the lunar south pole. The results provided and discussed in this chapter are taken from Gläser et al. [2014]. As will be demonstrated in this section, three confined areas clearly stand out from the analysis regarding long periods of illumination. These areas are known to be almost continuously illuminated and were targeted as landing sites for the ESA Lunar Lander mission [Carpenter et al., 2012]. Two of these sites are located on Shackleton Rim (referred to as SR1 and SR2) and one near Connecting Ridge (referred to as CR1), a ridge connecting the Shackleton and de Gerlache crater, and are investigated in more depth (Table 6). The nomenclature is taken from De Rosa et al. [2012], who previously discussed these landing sites. The three landing sites are located within an area of 20 x 20 km, which will be the size of the study region in this analysis. All results presented here are based on a calculation with a step size of 1 h (see Chapter 6.2).

Table 6: Coordinates of the three investigated landing sites SR1, SR2 and CR1.

Landing site	**Acronym**	**Location**
Shackleton Rim 1	SR1	89.7742°S, 203.4952°E
Shackleton Rim 2	SR2	89.6871°S, 197.0983°E
Connecting Ridge 1	CR1	89.4555°S, 222.6192°E

In accordance with De Rosa et al. [2012], first a time period of one year, October 22, 2018 - October 22, 2019, is evaluated. For each of the 8,783 time steps (365 days and 23 h) the percentage of the maximum possible sunlight is computed. When the entire solar disk can be observed, 100% is assigned to the associated time step, and for instance 25% is assigned if only a quarter of the solar disk can be observed. In general, it can be said that a random location on the Moon has an average illumination of 50% originating from the day and night cycle. As described in Chapter 6.2 a single accumulated map is created by stacking the 8,783 maps computed for each time step and averaging them into one map. However, a resulting average percentage of e.g. 50% does not necessarily imply that a specific area was in darkness for 50% of the considered time period or that only half of the solar disk was visible throughout the whole period. To find the longest continuous periods in sunlight and darkness all 8783 illumination maps need to be available and evaluated.

The adjusted final DTM retrieved in Chapter 7.1 (Fig. 54b, see also Fig. 53f) is displayed together with a cutout of the 20 x 20 km study region (Fig. 54a).

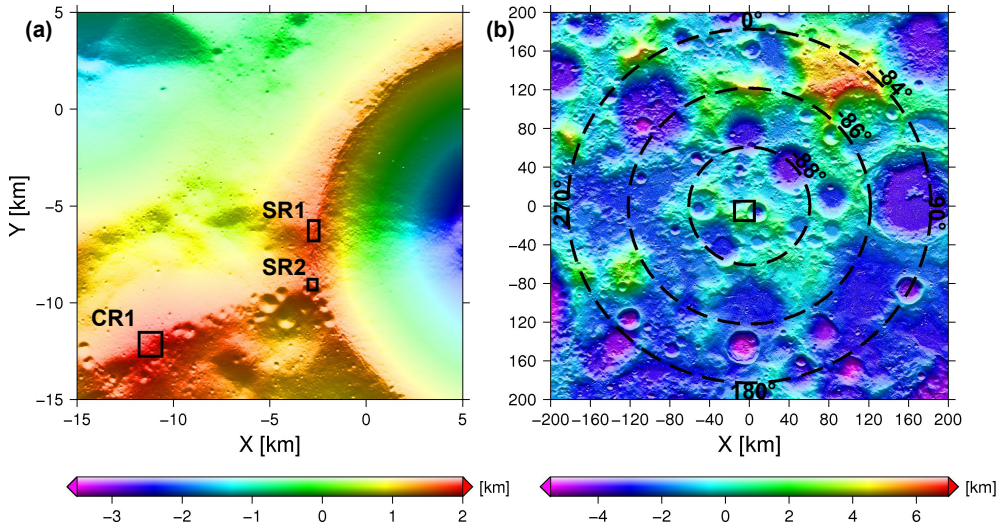

Figure 54: (a) The adjusted, 20 x 20 km study region, covering the three landing sites SR1, SR2, and CR1, which are outlined by black boxes. (b) The adjusted, 200 x 200 km NAC DTM of the lunar south pole with 20 m pixel resolution. The black square at the center of the image indicates the 20 x 20 km study region.

7.2.1 One-year analysis

Surface level The accumulated map for the 1-year time period evaluated at surface level, is shown in Fig. 55. For the 100 most illuminated spots, illumination levels ranging from 63.83% to 73.70% are found. In accordance to the results from previous studies [Bussey et al., 1999; De Rosa et al., 2012; Mazarico et al., 2011a; Noda et al., 2008], the three landing sites SR1, SR2, and CR1 are among these locations and show illumination levels of 70% and more. The three proposed stations in Speyerer and Robinson [2013] can also be found within the 100 most illuminated areas from this analysis. However, no locations of constant sunlight were found during the considered time period.

Several lines and clusters of above average illuminated small areas (>60%), further referred to as Region of Interests (RoIs), can be found along the ridge of the CR1 landing site (Fig 56a). However, only a small area of 400 m^2 (1 pixel) with an average illumination over 70% exists at this landing site.

The elongated SR1 area along the Shackleton Rim offers very good lighting conditions (Fig. 56b). An area of 1,200 m^2 (3 pixels) with illumination levels exceeding 70% exists also containing the spot with the highest overall illumination (73.70%) in the study region (Fig. 55 and 56b). Although the width of the RoI is very small, typically only 20 m (1 pixel), SR1 is an interesting landing site due to the quite large areal elongation of the RoIs of up to 3,200 m^2 (∼8 contiguous pixels), but also owing to the fact that the permanently shadowed Shackleton crater interior is right next to it [Bussey et al., 2010; Mazarico et al., 2011a].

Similar to SR1, the SR2 landing site has an elongated shape containing an area of 1,200

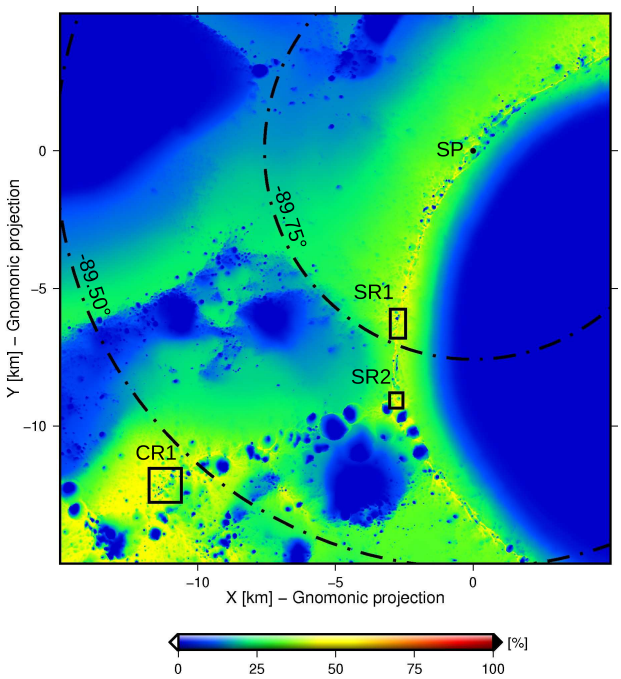

Figure 55: Accumulated illumination map at the surface level (h=0 m) from October 22nd, 2018 until October 22nd, 2019. The 3 landing sites CR1, SR1, and SR2 are bordered by a black box. The south pole (SP) and two parallels are also highlighted. The color bar indicates accumulated illumination over the considered time period.

m^2 (3 pixels) with an illumination of more than 70% (Fig. 56c).

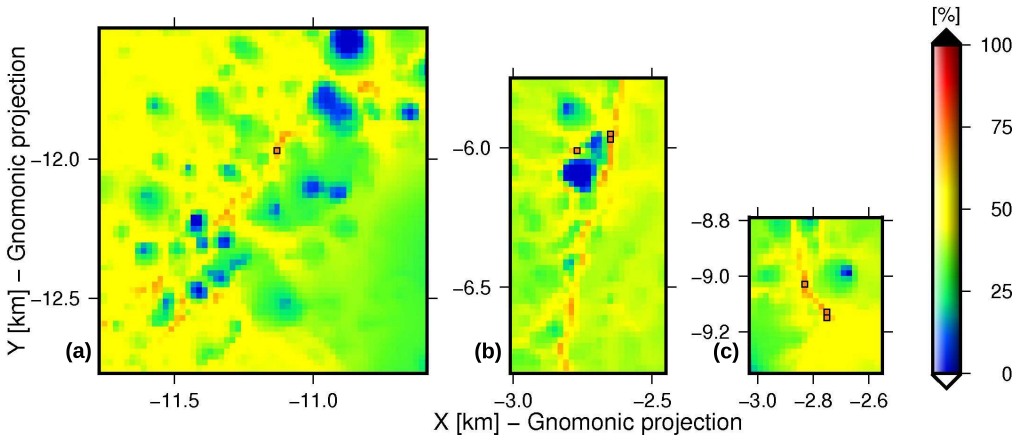

Figure 56: Accumulated illumination at surface level (h=0 m). Reddish colors indicate RoIs with outlined pixels representing spots with an average illumination higher than 70%. The color bar indicates accumulated illumination over the considered time period. (a): CR1 landing site area (89.4555°S, 222.6192°E). (b): SR1 landing site area (89.7742°S, 203.4952°E). (c): SR2 landing site area (89.6871°S, 197.0983°E).

Two meters above ground In order to simulate the received illumination of a solar panel mounted on a rover or stationary lander, the observer is elevated from surface level

to 2 m above ground. Here, the accumulated map (Fig. 57) reveals substantially higher illumination levels than at surface level. The areas of high illumination grow significantly and some of them become merged, compare Figs. 58 and 56. Contrary to the accumulated map at surface level (Fig. 55), the top-most illuminated pixels are exclusively found at the three landing sites SR1, SR2 and CR1 with an average illumination of 80.62%-86.62%. The majority of those pixels (79 pixels) are found at CR1, revealing that this area benefits the most with an elevated solar panel (2 m above ground).

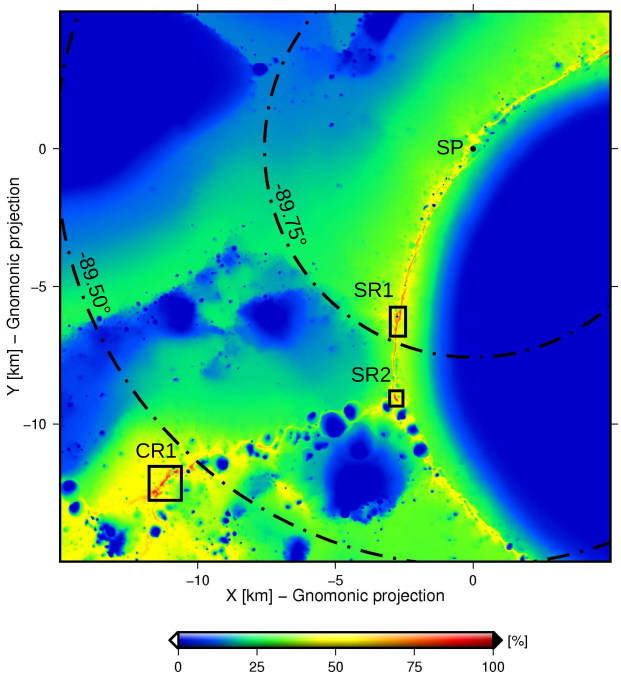

Figure 57: Accumulated illumination map at 2 m above the surface level from October 22nd, 2018 until October 22nd, 2019. The 3 landing sites CR1, SR1 and SR2 are bordered by a black box. The south pole (SP) and two parallels are also highlighted. The color bar indicates accumulated illumination over the considered time period.

In total, an area of ∼120,000 m^2 (297 pixels) receives more than 70% of average illumination at the CR1 landing site, see outlined pixels in Fig. 58a. The pixel with the highest illumination of 86.62% is also found here.

At SR1, a total area of ∼70,000 m^2 (173 pixels), which is mainly continuous, shows an average illumination of more than 70% (Fig. 58b).

SR2 has an area of ∼12,000 m^2 (49 pixels) with an average illumination of more than 70% which is completely continuous and curve-shaped (Fig. 58c).

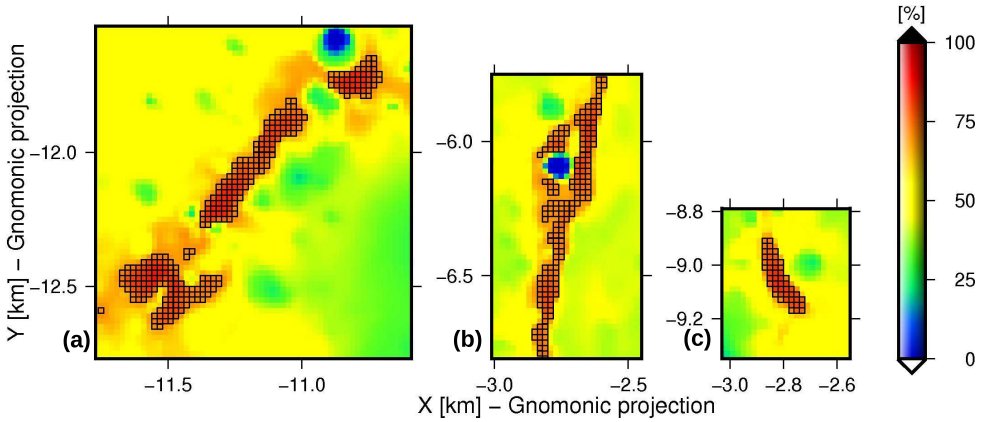

Figure 58: Accumulated illumination 2 m above surface level. Reddish colors indicate RoIs with outlined pixels representing spots with an average illumination higher than 70%. The color bar indicates accumulated illumination over the considered time period. (a): CR1 landing site area (89.4555°S, 222.6192°E). (b): SR1 landing site area (89.7742°S, 203.4952°E). (c): SR2 landing site area (89.6871°S, 197.0983°E).

7.2.2 Long-term investigation for CR1

Regarding the one-year analysis at 2 m above ground, CR1 clearly stands out from the investigated landing sites with its comparably long illumination periods for a relatively large area (Fig. 58a). However, the orientation of the lunar rotation axis in inertial space varies with the precessional cycle of 18.6 years (Fig. 59). During this cycle certain polar areas could receive high illumination levels for several years but be darker on average at other times. To investigate the long-term stability of illumination levels at CR1, illumination over a time period covering the whole precessional cycle of 18.6 years is evaluated. Illumination levels over a period of 19 years, December 24, 2015 to December 24, 2034, are shown for observers at 0 m, 2 m and 10 m above surface level (see Figs. 60, 61, 64).

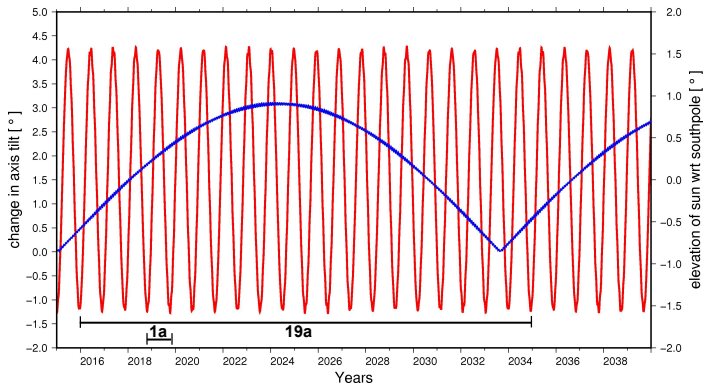

Figure 59: The elevation of the Sun as seen from an observer at the lunar south pole is shown (red curve, right scale). Negative values indicate southern winter since the Sun is below the horizon. The precessional cycle (blue curve, left scale) is shown as the change in axis tilt with respect to the axis tilt in 2015. The short horizontal bar shows the 1-year time period evaluated for the three landing sites, whereas the long bar indicates the 19-year evaluation done for CR1.

Surface level Where only one pixel of high illumination exists regarding a time period of 1 year at surface level (Fig. 56a), four pixels receive high illumination levels regarding the 19-year analysis (Fig. 60).

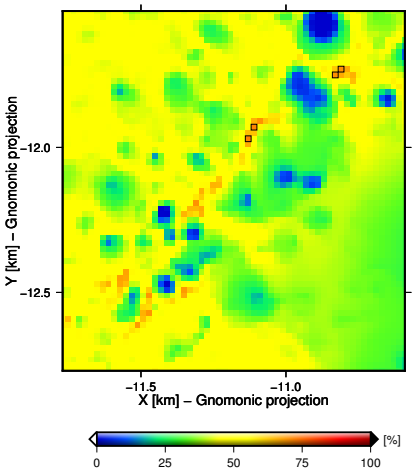

Figure 60: Accumulated illumination map of CR1 (89.4555°S, 222.6192°E) over a period of 19 years at surface level. Outlined pixels represent spots with an average illumination higher than 70%. The color bar indicates accumulated illumination over the considered time period.

Two meters above ground The same analysis at 2 m height above the surface level (Fig. 61), leads to a similar result compared to the results shown in Fig. 58a over the 1-year analysis. An increase from 297 to 358 pixels with high illumination can be observed. The highest accumulated illumination is 88.12% and occurs at 89.4395°S, 222.8066°E (referred to as spot 1, Fig. 61), where the longest continuous period in darkness is 4.58 days and the longest continuous period in light is 233.87 days. The accumulated percentage in light and in darkness over the considered period is 92.00% and 8.00%, respectively.

However, the smallest accumulated percentage in darkness is 7.73% and occurs at 89.4399°S, 222.8524°E (referred to as spot 2, Fig. 61). Consequently, spot 2 also has the highest accumulated percentage in light, which amounts to 92.27%. The longest continuous period in light and darkness at that location is 233.87 days and 4.62 days, respectively, with an accumulated illumination of 87.93%. Spot 1 and spot 2 are located right next to each other and are almost identical in their illumination properties. A plot of illumination versus time as well as a horizon plot for spot 1 are shown in Figs. 62 and 63. It can be noted, that even at lunar southern winter when the Sun is lowest over the horizon, illumination levels are still substantial.

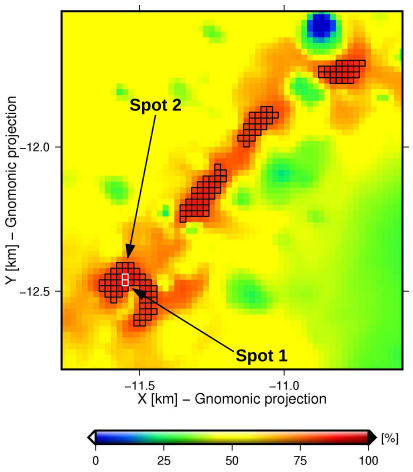

Figure 61: Accumulated illumination map of CR1 (89.4555°S, 222.6192°E) over a period of 19 years at 2 m height above the surface level. Black outlined pixels represent spots with an average illumination higher than 80%. Spot 1 and 2 are outlined in white. The color bar indicates accumulated illumination over the considered time period.

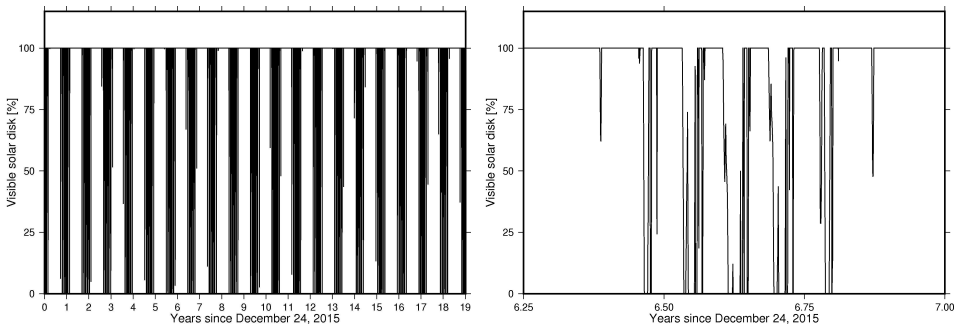

Figure 62: Plot of visible solar disk versus time for spot 1 at 2 m above surface level. Between periods of constant illumination, periods of rapidly changing lighting conditions occur (see zoom in at right hand plot). These times coincide with lunar southern winter. Spot 1 is located at 89.4395°S, 222.8066°E.

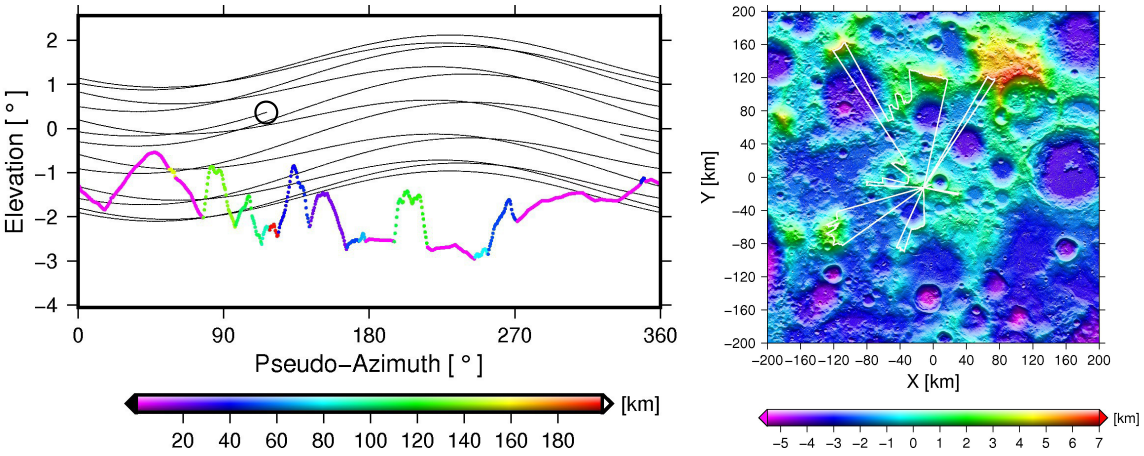

Figure 63: Plot of the horizon as seen from spot 1 (89.4395°S, 222.8066°E) at 2 m above surface level. (a) The horizon line is color-coded by the distance to the obstructing topography (horizon). The black lines show the trajectory of the center of the Sun as seen from spot 1 over 1 year (01-01-2020 to 01-01-2021). The apparent size of the solar disk is represented by a black circle (only true for the y-axis). (b) Horizon line plotted on the DTM, where the x-axis indicates 0° pseudo-azimuth counting counter-clockwise.

Ten meters above ground The accumulated illumination for an observer 10 m above ground was also investigated (Fig. 64). Although there is currently no active surface mission with a 10 m long structure nor is such mission in planning, the results presented here may be of interest for future engineers. In total 1,724 pixels (∼0.7 km^2) are now highly illuminated. The location of highest illumination, 92.55%, is located at 89.4516°S, 222.7581°E (referred to as spot 3, Fig. 64). The accumulated percentage in darkness is 4.39% and consequently 95.61% in light, with the longest continuous periods in darkness and light being 3.08 days and 262.42 days, respectively.

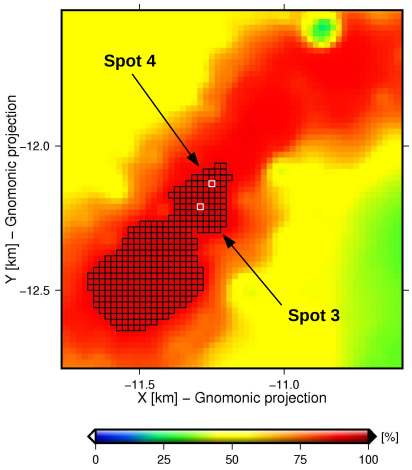

Figure 64: Accumulated illumination map of CR1 (89.4555°S, 222.6192°E) over a period of 19 years at 10 m height above the surface level. Black outlined pixels represent spots with an average illumination higher than 90%. Spot 3 and 4 are outlined in white. The color bar indicates accumulated illumination over the considered time period.

The longest accumulated period in light and therefore shortest period in darkness is found at location 89.4544°S, 222.8445°E and amounts to 4.35% for the dark period and 95.65% for the illuminated period (referred to as spot 4, Fig. 64). The average illumination is 91.94% with the longest continuous period of darkness being 3.17 days and the longest continuous period in light being 262.42 days. Spot 3 and spot 4 are located 90 m from each other and are almost identical in their illumination levels. A plot of illumination versus time and a horizon plot for spot 3 are shown in Figs. 65 and 66.

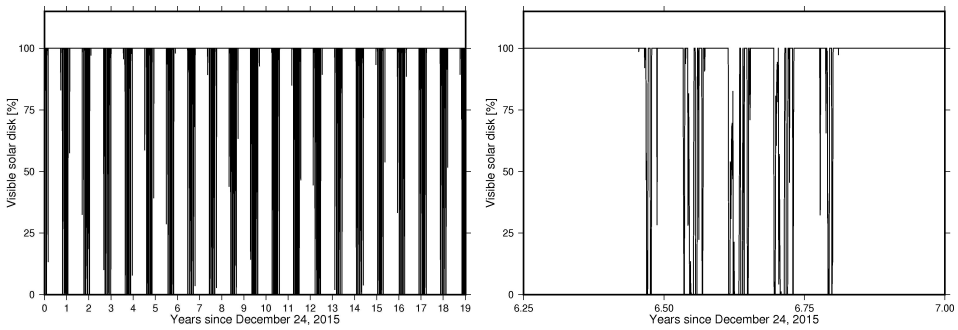

Figure 65: Plot of visible solar disk versus time for spot 3 at 10 m above surface level. Between periods of constant illumination, periods of rapidly changing lighting conditions occur (see zoom in at right hand plot). These times coincide with lunar southern winter. Spot 3 is located at 89.4516°S, 222.7581°E.

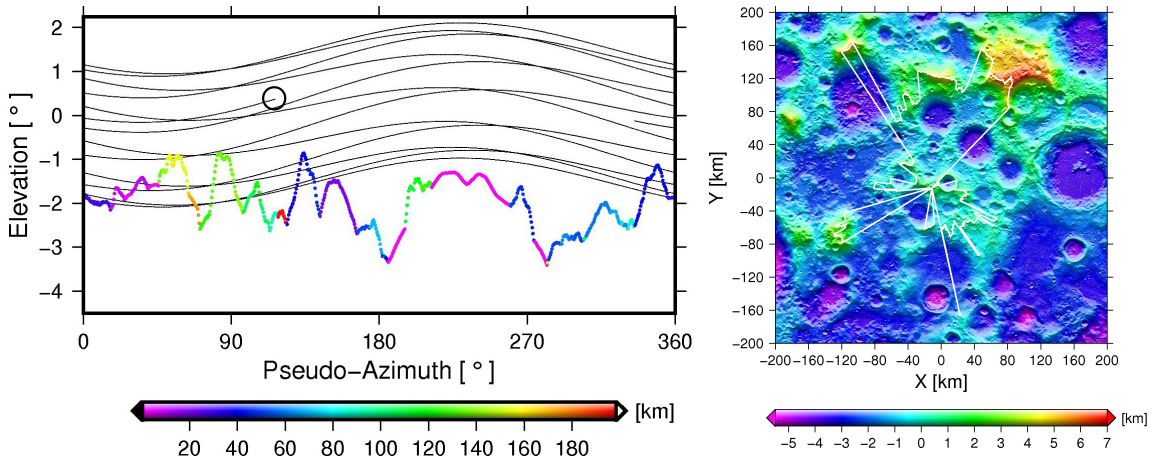

Figure 66: Plot of the horizon as seen from spot 3 (89.4516°S, 222.7581°E) at 10 m above surface level. (a) The horizon line is color-coded by the distance to the obstructing topography (horizon). The black lines show the trajectory of the center of the Sun as seen from spot 3 over 1 year (01-01-2020 to 01-01-2021). The apparent size of the solar disk is represented by a black circle (only true for the y-axis). (b) Horizon line plotted on the DTM, where the x-axis indicates 0° pseudo-azimuth counting counter-clockwise.

7.2.3 Comparison with previous studies

As already mentioned in 6.2.1, previous studies already investigated illumination conditions at the lunar south pole. Although all publications discussed in this chapter agree on the fact, that no points of eternal light exist or at least could not be identified, there are significant differences that need to be addressed. Here, results from previous studies are compared to findings in this study and are put into context.

A list of the highest illumination spots found in previous studies is shown in Table 7, see also Speyerer and Robinson [2013]. Results from different studies can only be compared when evaluated over the same time period for reasons of planetary constellation and the influence of the lunar precessional cycle. The results of the long-term study over 19 years from this work are compared with those retrieved by Mazarico et al. [2011a] for observers at 0 m and 10 m above ground. An additional 6-months analysis (March 31, 2010 to September 24, 2010) was carried out to compare the results from surface levels with those by De Rosa et al. [2012].

In an analysis evaluated over 6 months and at surface level, De Rosa et al. [2012] found the location receiving maximum illumination of 84.13% within the SR2 landing site area. Evaluating the same time period in this study, however, leads to a maximum illuminated spot within the SR1 landing site with 73.84% illumination (compare points 4 and 6 in Fig. 67 and Table 7). The two locations are a few kilometers apart from each other and differ more than 10% in illumination, which is a significant difference. The main differences in the two simulations is found in the resolution and quality of the used LOLA DTM. De Rosa et al. [2012] used an unadjusted LOLA DTM with half the pixel-resolution of this study. Although the adjustment as described in Chapter 6.1 substantially improves the quality of the DTM, the resolution has an even bigger impact on the results regarding illumination. When the original resolution of the adjusted 20 m/pixel LOLA DTM from this study is reduced to 40 m/pixel in order to resemble the DTM used by De Rosa et al. [2012], the location receiving maximum illumination jumps from the formerly 73.84% illuminated location at SR1 to a 81.30% illuminated location at SR2. The latter location is now right next to the location found by De Rosa et al. [2012] and shows a similar illumination level (compare points 4 and 5 in Fig. 67 and Table 7).

Similar to the previous comparison, Mazarico et al. [2011a] identified the maximum illuminated spot in their long-term analysis evaluated at surface level within the CR1 landing site, whereas this study finds the maximum spot at SR2 when running simulations over the 19-year period (compare points 7 and 9 in Fig. 67 and Table 7). The results can be reproduced, however, when the resolution is reduced to 240 m/pixel as used in their study (compare points 7 and 8 in Fig. 67 and Table 7). Note, that the location receiving maximum illumination in the 19-year study at surface level in this work is almost identical with the location found by De Rosa et al. [2012] and station 1 (89.685°S, 196.7°E) identified by Speyerer and Robinson [2013] in their 1-year period study (compare points 4 and 9 in Fig. 67 and Table 7).

The spot of maximum illumination found by Mazarico et al. [2011a] simulated 10 m above ground is located 52 m away from the one found in this work, corresponding to only 1/5th of the pixel resolution used in their study (240 m). Hence, the found locations can be considered identical even though vastly different resolutions were used (compare points 12 and 13 in Fig. 67 and Table 7).

The differences in the three studies at surface level can be explained by the dependency of the analysis on raw data density, the local topography and, therefore, the interpolation algorithms that are used. At surface level, topography in the near-field is dominating the amount of received illumination and resolution differences will have a great influence on the result (compare points 4, 6 and 7, 9 in Table 7). A plot of the local horizon of the same viewing point derived from a 20 m/pixel and a 40 m/pixel DTM is shown in Fig. 68a. Here, the significance of local topography can be seen, where a higher resolved horizon is generally above the lower resolved horizon, which results in lower illumination levels. The far distant topography is of greater interest for simulations carried out higher above surface level, e.g. 10 m above ground, where most of the near-field can be looked across. Here, the resolution of the DTM is of minor significance, compare points 12, 13 in Table 7 and Fig. 68b. In general, small height differences in corresponding DTM pixels can occur when using different resolutions, different interpolation methods or different LOLA spots and will have a great impact on the elevation angles calculated in the near-field but are negligible when calculating elevation angles in the far-field.

Table 7: List of points with highest illumination at the lunar south polar region of previous studies in combination with several points found in this study. The last column shows the evaluated period, where studies over the full lunar precessional cycle are marked 'lpc'. All results retrieved in this analysis, which can be compared to previous studies are highlighted.

P.	Study	Res. [m/pix]	Ill. [%]	Location Latitude, Longitude	h [m]	Period [a]	Site
1	Noda et al. 2008	474	86	-88.8, 124.1	0	lpc	-
2	Bussey et al. 2010	474	86	-88.74, 124.5	0	lpc	-
3	Speyerer and Rob. 2013	100	71.7	-89.74, 201.20	0	1.0	-
4	**De Rosa et al. 2012** [1]	**40**	**84.13**	**-89.687, 196.144**	**0**	**0.5**	**SR2**
5	**This study** [1]	**40**	**81.30**	**-89.6871, 197.2887**	**0**	**0.5**	**SR2**
6	**This study** [1]	**20**	**73.84**	**-89.7846, 203.9358**	**0**	**0.5**	**SR1**
7	**Mazarico et al. 2011a**	**240**	**89.01**	**-89.45, 222.69**	**0**	**lpc**	**CR1**
8	**This study**	**240**	**86.84**	**-89.44, 222.52**	**0**	**lpc**	**CR1**
9	**This study**	**20**	**76.23**	**-89.6856, 196.7626**	**0**	**lpc**	**SR2**
10	This study (spot 1)	20	88.12	-89.4395, 222.8066	2	lpc	CR1
11	This study (spot 2)	20	87.93	-89.4399, 222.8524	2	lpc	CR1
12	**Mazarico et al. 2011a**	**240**	**93.10**	**-89.45, 222.69**	**10**	**lpc**	**CR1**
13	**This study (spot 3)**	**20**	**92.55**	**-89.4516, 222.7581**	**10**	**lpc**	**CR1**
14	This study (spot 4)	20	91.94	-89.4544, 222.8445	10	lpc	CR1

[1] The period evaluated was 6 months, March 31, 2010 -September 24, 2010.

An overview of the distribution of points with maximum illumination retrieved by Mazarico et al. [2011a], De Rosa et al. [2012] and this study, is shown in Fig. 67.

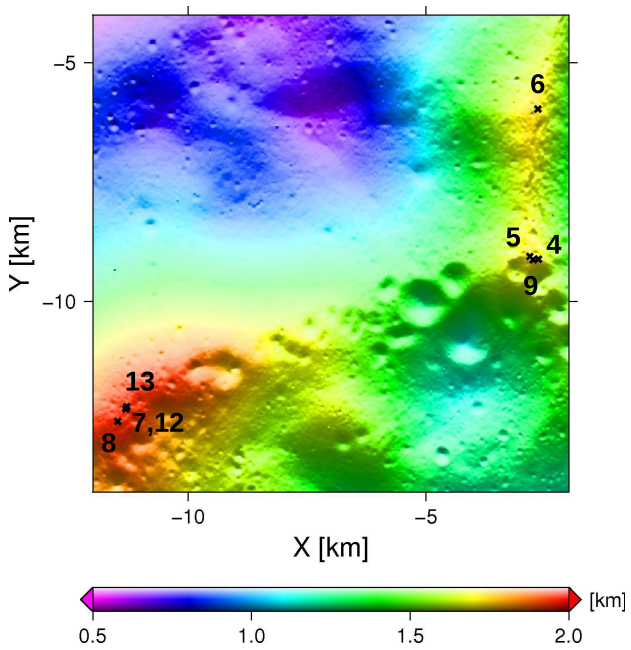

Figure 67: Overview of spots of maximum illumination found in different studies. Point numbers correspond to the first column in Table 7.

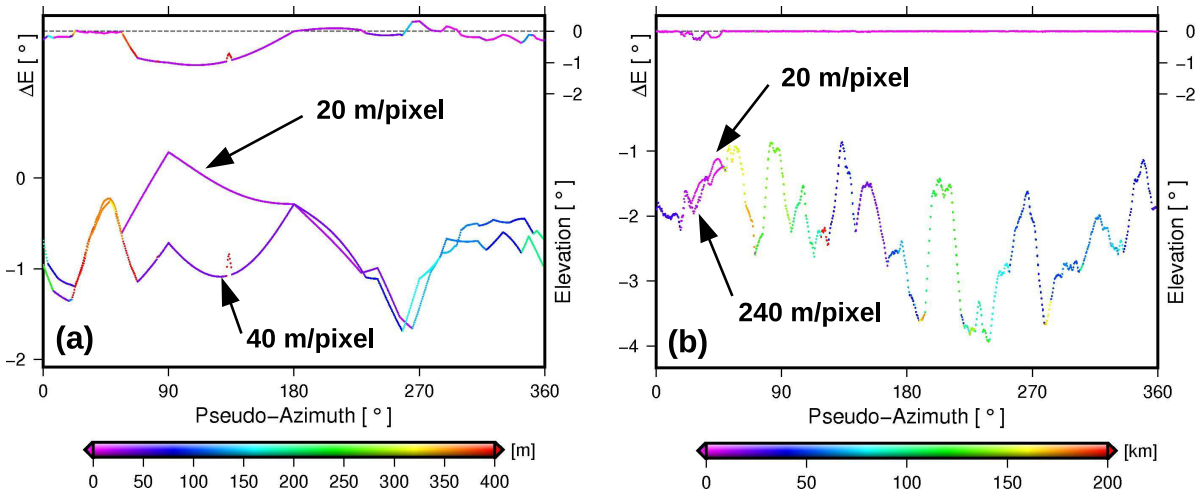

Figure 68: Horizons and differences between horizons are color coded by distance. (a) Comparison of the local horizon of spot 1 derived from a 20 m/pixel and 40 m/pixel DTM at surface level (distance scale in meter). It can be noted, that the horizon calculated from the 20 m/pixel DTM generally is higher in the near-field than the horizon from the 40 m/pixel DTM. (b) Comparison of the local horizon of spot 1 derived from a 20 m/pixel and 240 m/pixel DTM at 10 m above ground (distance scale in kilometer). In the far-field the two horizons are identical and only small differences appear in the rather short portion of the near-field, where the horizon of the 20 m/pixel lies above the horizon of the 240 m/pixel DTM.

7.2.4 Illumination - Validation

For validation purposes the distribution of light and shadow in the synthetic images is compared with selected NAC images (NAC image M139811097L/R for CR1 and M141385360L/R for SR1 and SR2), showing the CR1, SR1 and SR2 landing site (see Fig. 69 a,c). Synthetic images are computed for the same areas (as covered by the selected NAC images) using the known time of image acquisition (see Fig. 69 b,d). Note, that the resolution difference between the NAC images and the simulated images are of a factor 40 (0.5 m NAC image and 20 m LOLA synthetic image).

The comparison of simulated data with ground truth reveals that very small surface features of just a few pixels are reproduced in the simulation. Hence, accurate illumination information can be reproduced from the DTM.

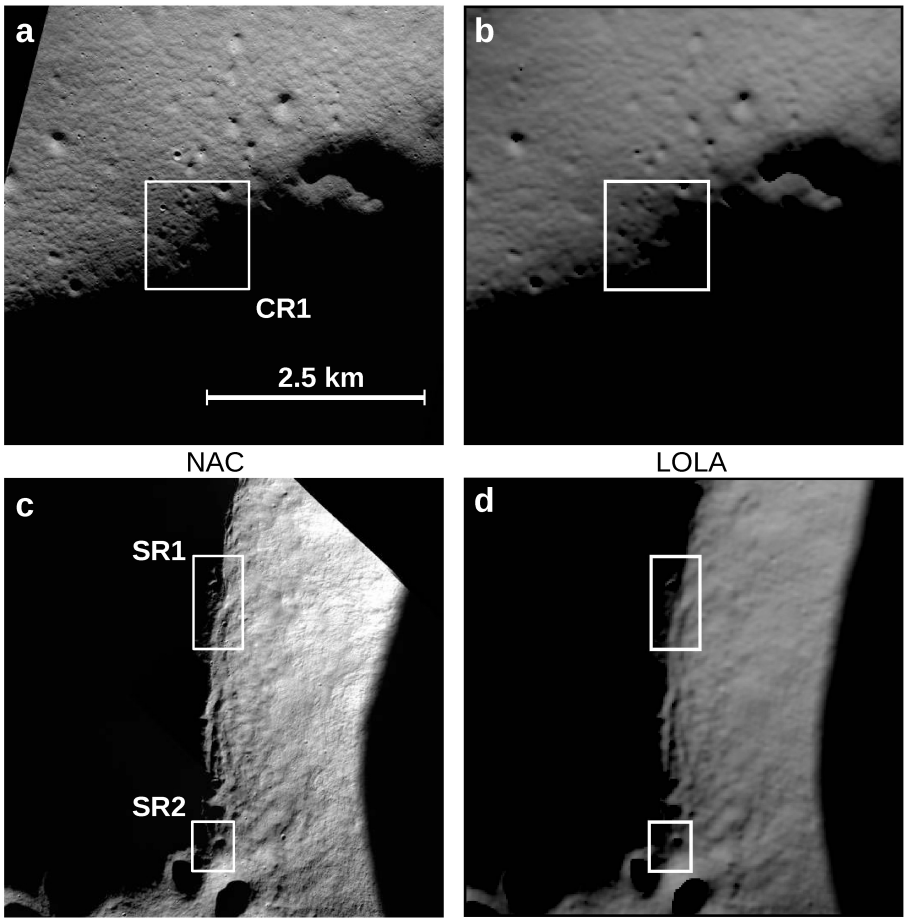

Figure 69: Comparisons of NAC images (a,c) and synthetic images (b,d) computed from the LOLA DTM at NAC image acquisition time. Difference in brightness is due to surface variations in albedo which is not accounted for in the synthetic images. Note, that the synthetic images reproduce even small morphologic details. Left: NAC images of CR1 (M139811097L/R - (a)) and SR1, SR2 (M141385360L/R - (c)) potential landing site areas. Right: Simulated illumination at CR1 (b) and SR1, SR2 (d) using LOLA data. The scale bar is valid for all images.

7.3 Earth-visibility

This chapter summarizes the results for the visibility of the Earth as seen from the lunar south pole. Similar to the previous chapter, the analysis concentrates on the Connecting Ridge landing site and in more depth on the locations referred to as spot 1-4 (see Chapter 7.2). For this analysis a time step of 1 h was chosen and the line-of-sight to 10 ESA tracking stations was determined. In Table 8 and Fig. 70 an overview of the coordinates and the distribution of the stations on the Earth are given. For characterization of a potential landing site it is of interest what the total visibility of the Earth is combined for all stations but also knowledge about periods in radio dead zones, where no data can be sent nor received is an important information. Although the Earth is rotating 15° every 1 h, the long periods evaluated and the number of stations will mostly cancel out the inaccuracies introduced by the rather low time resolution.

Table 8: The 10 core stations of the ESA tracking network 'Estrack' spanning over 7 countries.

Stations	**Latitude**	**Longitude**	**Height [m][1]**
Kiruna	67°51'25.66"	20°57'51.57"	402.2
Kourou	05°15'05.18"	-52°48'16.79"	-14.7
Maspalomas	27°45'46.40"	-15°38'01.68"	205.1
Perth	-31°48'09.08"	115°53'06.58"	22.16
Redu	50°00'01.64"	05°08'43.24"	386.6
Santa Maria	36°59'50.10"	-25°08'08.60"	276
Villafranca	40°26'33.23"	-03°57'05.70"	664.8
New Norcia - DSA 1	-31°02'53.61"	116°11'29.40"	252.26
Cebreros - DSA 2	40°27'09.68"	-04°22'03.18"	794.1
Malagüe - DSA 3	-35°46'33.63"	-69°23'53.51"	1550

[1] Heights are given with respect to the WGS-84 reference ellipsoid.

7.3.1 Results

Standing on the lunar south pole and looking towards the Earth, the longest visibility hours will be reached for Earth stations located on the southern hemisphere. The southernmost station in this work is Malagüe (see Table 8). In Fig. 71 an accumulated map (gnomonic projection) of the study area on the south pole is displayed for ESA station Malagüe in Argentina. The evaluated period is one year, corresponding to the period chosen in Chapter 7.2. Owing to the fact that the positive Y-axis of the gnomonic map projection (nearside) is always pointing towards the Earth, generally only terrain features facing towards the +Y-direction can have visibility to the ESA stations. The maximum lies at ∼98 days and occurs at the Connecting Ridge landing site. Expressed in percentage, a maximum visibility of ∼26.8% is reached for the Malagüe station, in Chapter 6.3,

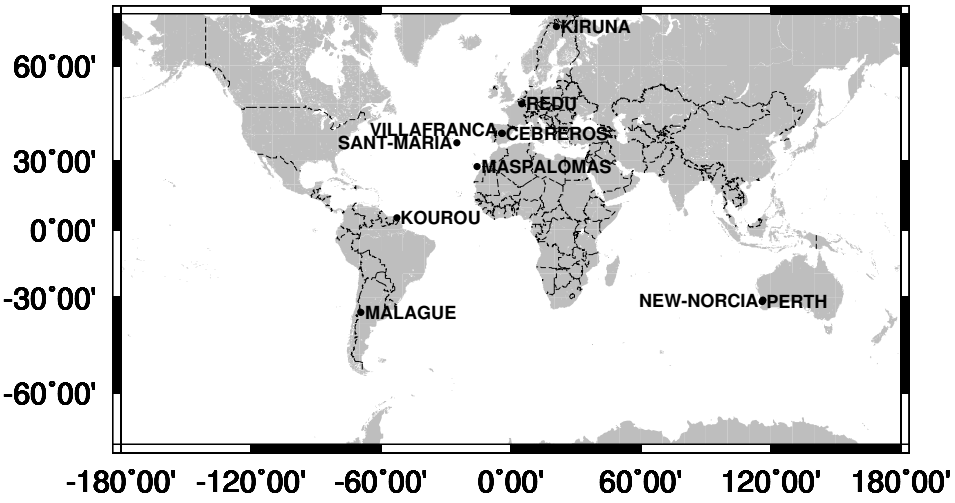

Figure 70: Map of the ten ESA tracking stations. Note, that the density on the southern hemisphere is much lower than on the northern hemisphere.

however, a theoretical visibility of the Earth of ∼55% was predicted. This is in accordance with the presented result when considering Earth rotation. Then, due to the day and night cycle, the 55% would be halved to 27.5%.

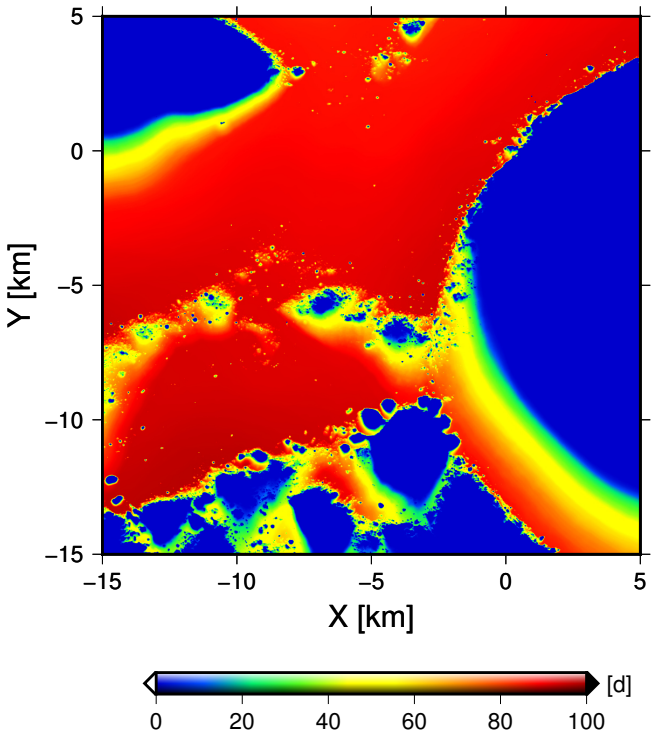

Figure 71: The accumulated visibility of the ESA station Malagüe as seen from the study area on the lunar south pole. It is the most southern ESA station and hence has the longest visibility hours. The maximum is located at the CR1 landing site and amounts to ∼98 days. The map is displayed using gnomonic map projection.

7.3.2 Long-term investigation for CR1

In Chapter 7.2 four spots were identified receiving maximum illumination at 2 m and 10 m above ground at the CR1 landing site. Regarding the visibility of the Earth, CR1 is again favorable (see Fig. 71), and therefore the four stations are revisited in this section.

Earth-visibility to the ten ESA stations was evaluated over the same 19-year period as in Chapter 7.2. A plot of the summed visibility to the radio stations over time is shown for spot 1-4 in Fig. 72. The period of almost continuous visibility of spot 4 lasts ∼14.45 days and is followed by a continuous radio dead zone of ∼12.8 days. Together this represents the period of the lunar orbit, where the percentage of the visibility is 53%. The result is in accordance to the finding in Chapter 6.3, where a maximum theoretical visibility of 55% was predicted.

As can be seen in Fig. 72, the ten stations cannot be seen simultaneously from any of the four spots. By comparing the coordinates in Table 8 and the map in Fig. 70 it can be noted, that station Malagüe and New Norcia form an angle of ∼185° when Europe is in the center of view as seen from the Moon. Therefore, one of the stations is always below the horizon when all other nine stations can be seen. When the Pacific Ocean is in the center of view as seen from the Moon, then the angle between Malagüe and New Norcia is 175° and both could possibly be observed. Due to resulting, very low elevation angles to these stations, however, the lunar horizon is preventing visibility for very short times of about 1 h (resolution limit). By adding one or two stations in the southern Pacific Ocean, the short gaps in visibility would be closed and continuous visibility for about half a lunar day could be achieved.

The longest continuous times in radio silent zones over a 19-years period are 15.42, 13.92, 13.95 and 13.04 days for spot 1-4 respectively. These gaps in radio link periods can be overcome by on-board storage systems and later downlinking or a relay satellite. Another possibility is to place a relay station on the nearside having a continuous radio link to Earth and simultaneously a direct line-of-sight to the landing site.

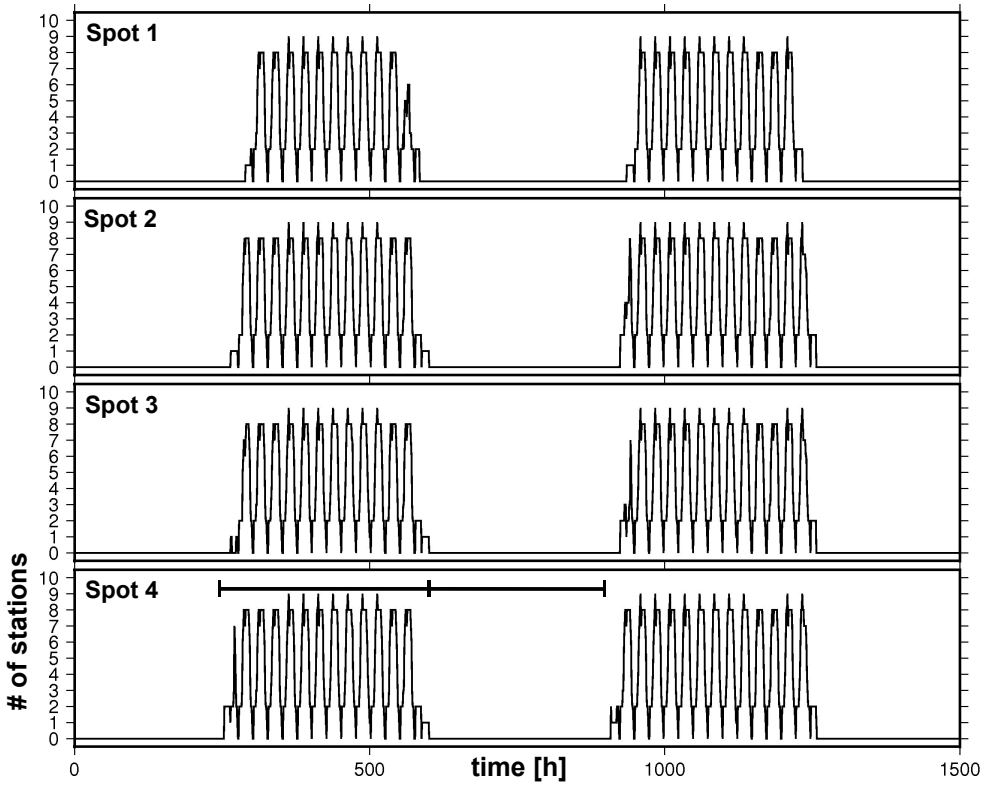

Figure 72: The visibility of the ten ESA stations on Earth as seen from the identified locations (spot 1-4) is displayed. Long continuous periods of visibility (south pole above the ecliptic) are followed by roughly the same length in a radio dead zone (south pole below the ecliptic). Both periods last for about half the lunar orbit period. A maximum visibility of nine stations simultaneously can be achieved. As indicated by a scale for spot 4, the period of Earth-visibility lasts ∼14.45 days and is followed by a period in a radio dead zone of ∼12.8 days.

7.4 Slope and Roughness Maps

To better characterize the suitability of a proposed landing site, slope and roughness maps make a significant contribution (see Chapter 6.4). These maps are indispensable when planning planetary surface missions, such as landers or rovers. Depending on the rover design, slope values higher than a predefined limit will cause the rover to slide and, in the worst case scenario, even roll over and land upside down. Stationary landers can also fall over on inclined terrain, and therefore flat surfaces are always preferable. For this reason high-resolution slope maps greatly assist during the landing site selection process and in rover traverse planning.

For the two Mars Exploration Rovers (MERs), Spirit and Opportunity, slope values on the 1 km length-scale were constrained to be less than 2°, on the 100 m length-scale less than 5° and on the 10 m length-scale less than 15° [Golombek et al., 2003a]. For the landing process of MSL slopes on the 2-5 m scale were constrained to be less than 30° [Golombek et al., 2012].

The derivation of roughness values for landing sites of previous missions were determined by means of rock statistics. When orbital images of reasonable ground resolution are available, rocks within the defined landing site area are mapped and counted. From histograms of the cumulative numbers of rocks/m^2 versus rock diameter, the possibility of encountering a rock greater than a certain diameter for a given surface area can be derived [Golombek et al., 2003b]. Another approach, however, is to use roughness values inferred from laser pulse width data as shown in Neumann et al. [2003]. Although the resolution of laser data can generally not (yet) compete with resolutions acquired by cameras, roughness derived from laser data as shown in Chapter 6.5.2 will be used in this study.

Despite the fact that the resolution of NAC images is 0.5 m, only rocks with a distinctively different gray value than the surrounding surface can be directly identified given that their size is at least in the order of 2-3 pixels. Therefore, the smallest rocks detectable in NAC images have diameters of ∼1 m. The timing resolution of LOLA, on the other hand, allows for the detection of rocks within the 5 m laser footprint of down to ∼20-30 cm [Smith et al., 2011b]. Also keep in mind, that cameras are passive sensors that are incapable of mapping terrain and boulders in shadowed areas, which are plenty regarding the lunar south pole. Standard deviations of plane fits (*Sigma-Z*) represent another estimate for surface variations within a baseline of, e.g. 150 m (3 shots, up to 15 spots), as shown in Chapter 6.5.2. *Sigma-Z* surface roughness was also determined for baselines of ∼500 m (10 shots, up to 50 spots) and ∼50 m (1 shot, up to 5 spots).

7.4.1 Slope Maps

Slope maps on the 150 m length-scale of the lunar south pole are shown in Figs. 73 a,b. In general, it can be noted that crater walls are steep in the order of 10-40° whereas intermediate terrain and crater floors typically show slopes of less than 5°. The most prominent feature is the Shackleton crater (in the center right at the south pole), where the highest slopes in the displayed region of up to ∼40° occur on its crater walls.

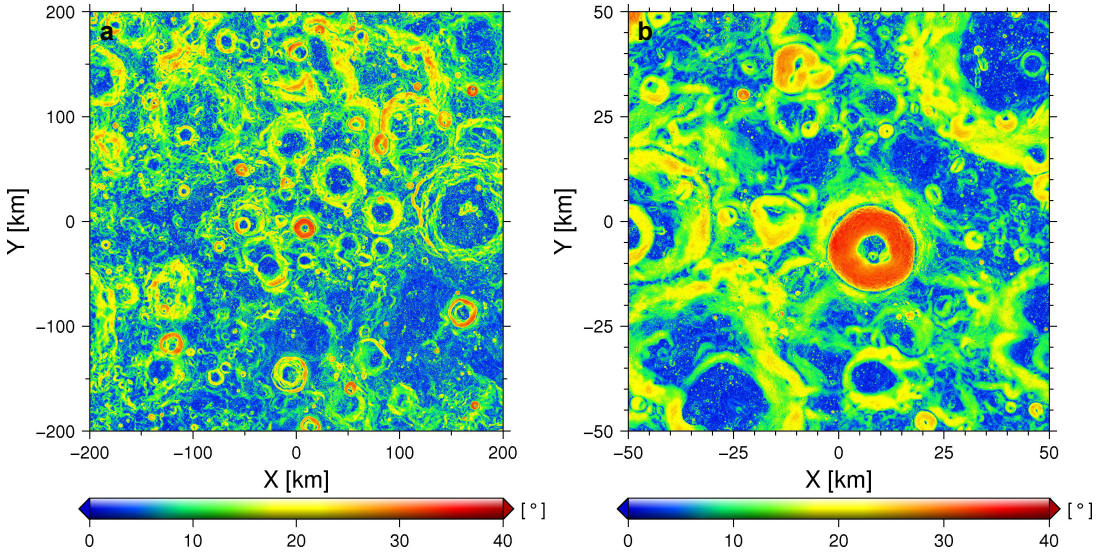

Figure 73: Slopes near the lunar south pole in gnomonic projection. (a) 200 x 200 km slope map with 20 m/pixel resolution. (b) 50 x 50 km slope map with 5 m/pixel resolution.

7.4.2 Roughness Maps

Roughness maps assembled from the standard deviations of LOLA plane fits (*Sigma-Z*) over 500, 150 and 50 m baselines and pulse width spread derived roughness on the 5 m laser footprint size are presented in this section. As can be noted, crater rims are the roughest features in the *Sigma-Z* maps, true for all baselines shown (Figs. 74 a-f). Their typical roughness values range from 5-10 m over a 500 m baseline and 2-5 m over a 150 m baseline to around 1-2 m over the shortest evaluated baseline of 50 m. Similar scaling is true for the roughness of crater floors, e.g. ∼5, ∼2 and ∼1 m for the 500, 150 and 50 m baseline, respectively. A mean *Sigma-Z* roughness value was estimated to be ∼3.2, ∼1.3 and ∼0.65 m for the three different baselines. Also note, that the walls of Shackleton appear to be rough in the 1 m scale for a 50 m baseline (Fig. 74f - crater in the center).

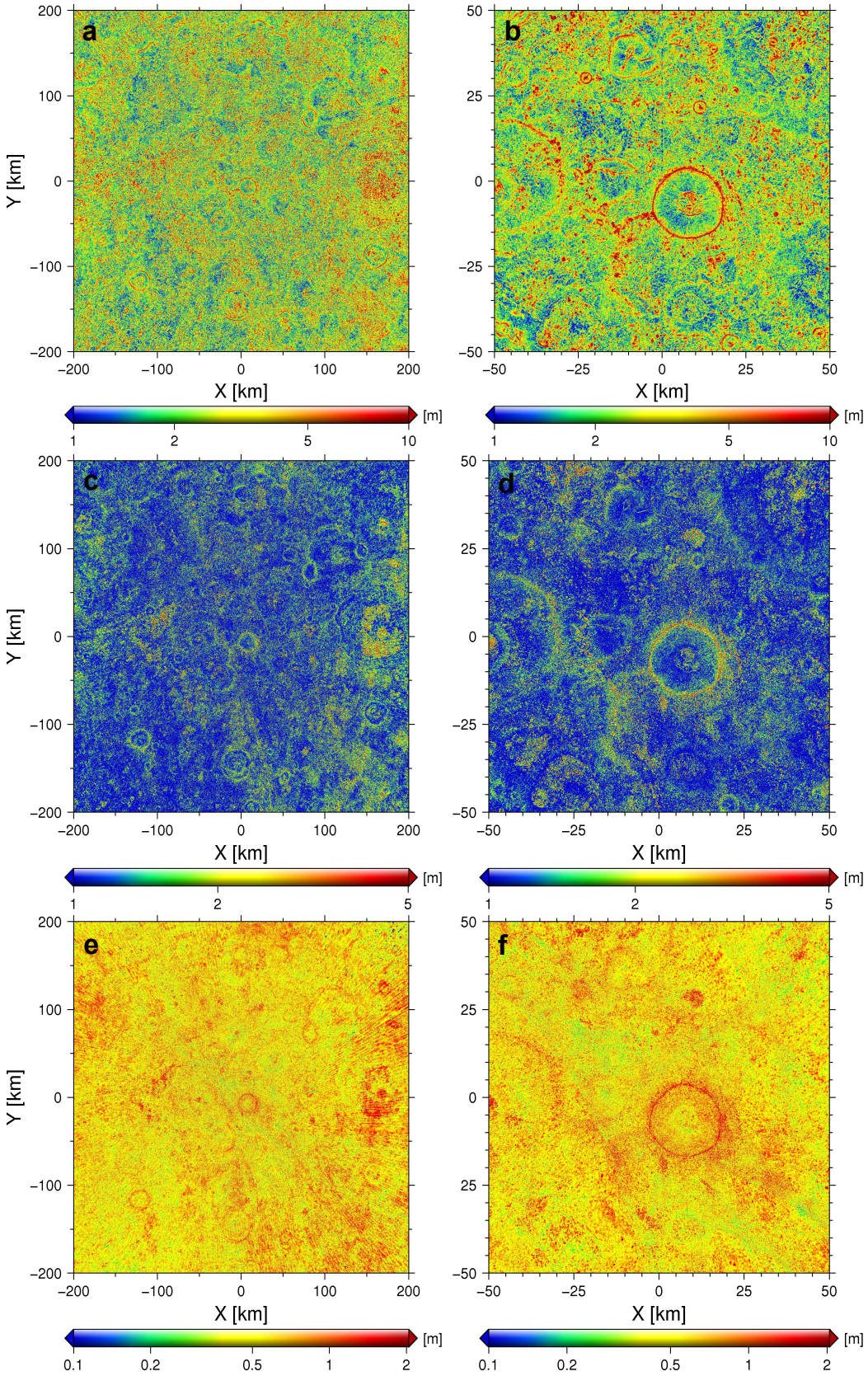

Figure 74: Shown are the color coded standard deviations of LOLA plane fits over a 500, 150 and 50 m baseline of the lunar south pole in gnomonic projection. (a,c,e) 200 x 200 km *Sigma-Z* map with 20 m/pixel resolution for a 500 (a), 150 (c) and 50 m (e) baseline. (b,d,f) 50 x 50 km *Sigma-Z* map with 5 m/pixel resolution for a 500 (b), 150 (d) and 50 m (f) baseline.

Generally, roughness maps derived from pulse width data are less reliable than *Sigma-Z* roughness maps. This is owed to the complex examination of pulse width data and the sensitivity of the derived roughness values to pulse energy measurements. The latter is especially challenging at the poles due to the described LOLA instrument anomaly and the high solar phase angle. Although extensive filtering was performed on the LOLA data set, where only pulses above 0.15 fJ energy levels, recorded at less than 5° off-nadir angle were selected, the roughness maps derived from pulse spread still suffer from some erroneous values. Nevertheless, the resulting roughness signal on a 5 m baseline is clearly visible (Figs. 75 a,b). Crater walls show pulse-width derived roughness of 50-100 cm whereas the rims are typically less rough in the order of 30-50 cm. Crater floors and intermediate terrain are almost completely flat on the 5 m baseline. An average roughness value of ∼30 cm is found for the presented maps. It can be noted, that Shackleton's crater wall appears to be rough in the sub-meter scale but smooth on the crater floors. Rough crater walls of Shackleton, e.g. boulder fields, were also assumed or indicated by other publications [Calla et al., 2014; Fa and Cai, 2014; Fa and Fang, 2013; Thomson et al., 2011, 2012]. As shown before, also the shortest baseline of 50 m reveals elevated roughness levels at Shackleton's crater walls (Fig. 74f). This finding is subject to future work and shall only be mentioned at this point.

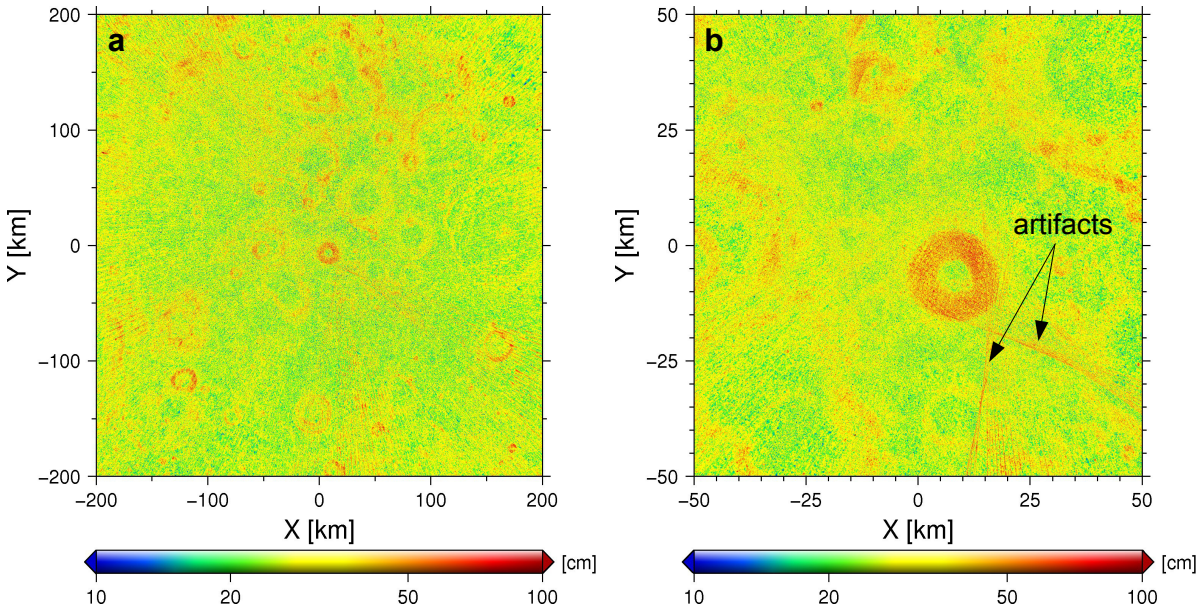

Figure 75: Shown is the color coded pulse width derived roughness over a 5 m baseline of the lunar south pole in gnomonic projection. (a) 200 x 200 km roughness map with 20 m/pixel resolution. (b) 50 x 50 km roughness map with 5 m/pixel resolution.

Where other roughness calculations are rather difficult to compare or interpret due to the nature of their derivation, the two methods introduced here are directly related to each other and can be compared. Although the derivation of the roughness values are quite different, both techniques determine the width of the Gaussian function about the mean surface over different baselines. The pulse width approach determines the leading and trailing edge of a pulse, which can be converted into a metric unit and interpreted as the RMS height difference within the laser footprint (Fig. 76a). The Sigma-Z approach on the other hand determines the standard deviation of a plane fit through several LOLA spots, which is basically the same physical meaning as in the pulse width approach (Fig. 76b).

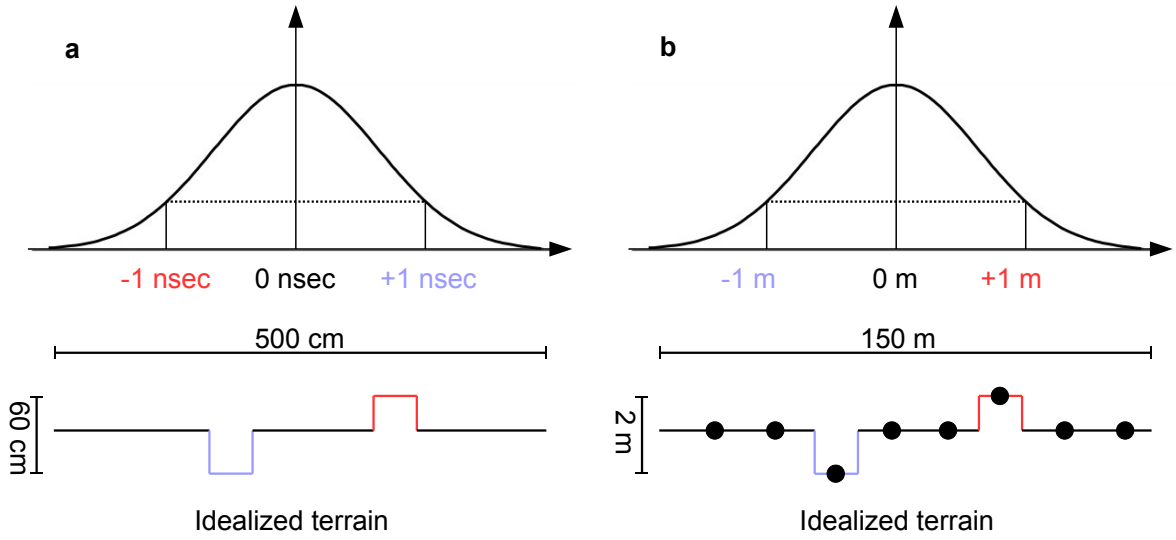

Figure 76: The physical meaning of pulse width derived roughness (a) and the Sigma-Z roughness (e.g. 150 m baseline) based on standard deviations of plane fits (b) are compared. Both techniques determine the width of the Gaussian function about a mean surface.

7.5 Connecting Ridge - Landing Site overview

The purpose of this chapter is to summarize all results retrieved for the Connecting Ridge landing site and to define a potential landing area within CR1. In Fig. 77 all maps derived for the CR1 site are displayed.

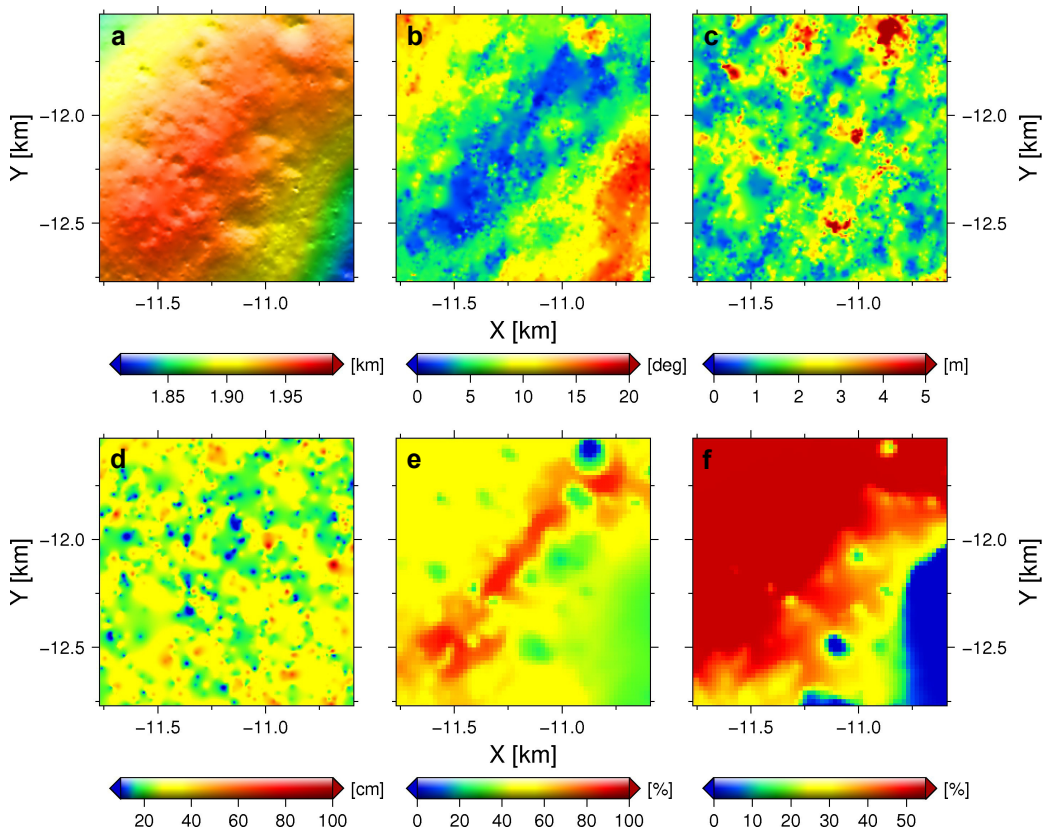

Figure 77: A collection of all maps derived in this work is displayed at the CR1 landing site. (a) DTM, (b) Slope map, (c) *Sigma-Z* roughness on a 150 m baseline, (d) Pulse width derived roughness, (e) Illumination condition (20 years average and 2 m above ground), (f) Earth-visibility.

One possibility to define the desired landing area within the landing site is to filter each map according to the mission dependent, constraining parameters. In this study three levels of constraints are introduced for each parameter, best (blue) - good (white) - critical (red).

A mission with the following fictional, very simplified constraints was assumed; the critical value for slope, that the lander can handle, is set to be 10°. A maximum *Sigma-Z* roughness on the 150 m baseline of 8 m and a maximum pulse width derived roughness on a 5 m baseline of 80 cm are chosen. To ensure sufficient electrical powering of the lander/rover to survive the cold nights, the solar arrays (at 2 m above ground) need to be in sunlight for more than 40% of the time. For downlink of science data and uplink of commands, Earth stations need to be visible for more than 20% of the time (see Fig. 78b,c,d,e,f). The DTM itself is not constrained, e.g. for the MER spacecraft which relied

on aero-braking techniques the landing site had to reside below -1.3 km, with respect to the MOLA sphere [Golombek et al., 2003a; Smith and Zuber, 1998]. Since the Moon has no atmosphere, this constraint does not apply.

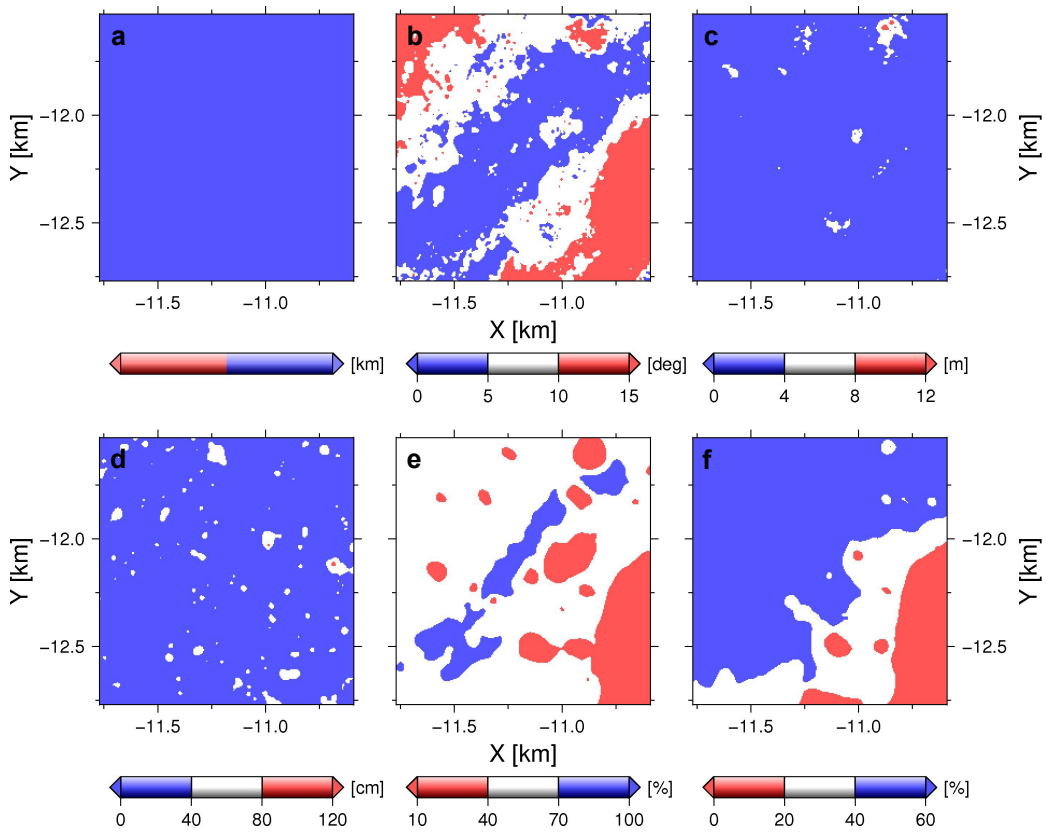

Figure 78: A collection of all maps derived in this work is displayed at the CR1 landing site. Each map is colored according to the classification, best (blue) - good (white) - critical (red). (a) DTM (no constraints), (b) Slope map ($< 10°$), (c) *Sigma-Z* roughness on a 150 m baseline (< 8 m), (d) Pulse width derived roughness (< 80 cm), (e) Illumination condition (20 years average and 2 m above ground) ($> 40\%$), (f) Earth-visibility (> 20 %).

Combining all maps from Fig. 78 and finding areas common to all maps, the final landing area within CR1 can be identified. At the dark blue and outlined area in Fig. 79, all implied constraints on the landing site were satisfied. The resulting area at CR1 which is preferable for landing covers 129,825 m^2. Although the constraints were chosen freely, they resemble a realistic mission design since rather strict constraints were adopted.

A landing dispersion of ∼200 m diameter is envisaged in this fictional study, using autonomous and precision landing technologies relying on hazard detection and avoidance strategies [Johnson and Ivanov, 2011]. Johnson and Ivanov [2011] and Epp and Smith [2007] have shown, that landing within 90 m of a predetermined location is feasible using laser altimeters at the landing procedure. Landing dispersion areas for spot 1 and 3 show an average of 97.82% and 94.59% safety derived from Fig. 79, receptively. Note, that spot 3 was originally found for solar arrays at 10 m above ground and is evaluated here based on an illumination and Earth communication map at 2 m height.

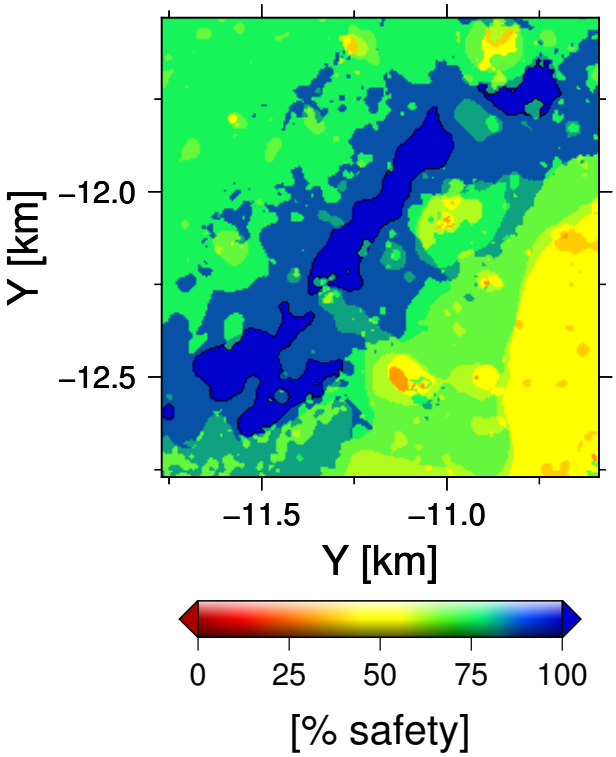

Figure 79: The intersection of all maps with applied constraints (Fig. 78) leads to the final landing site map, revealing areas for preferred landing. The dark blue and outlined area best satisfies all constraints and amounts to an area of 129,825 m^2.

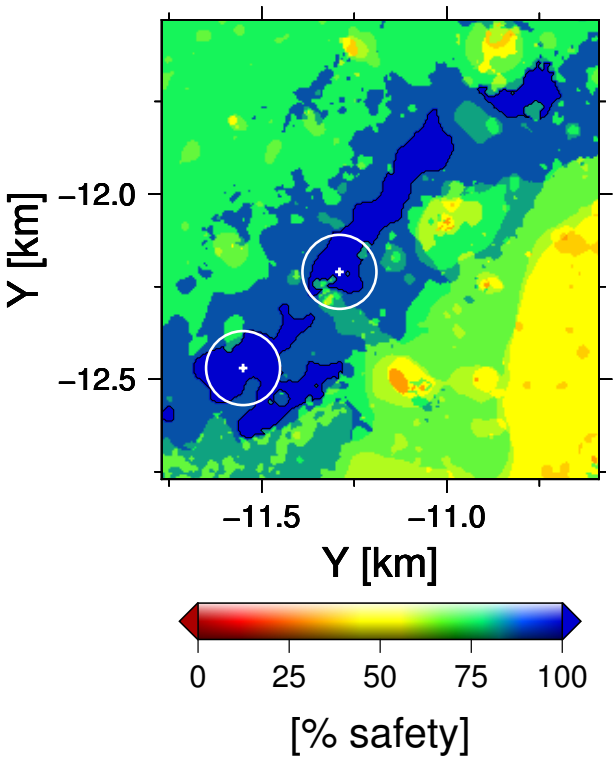

Figure 80: A 200 m diameter landing dispersion around spot 1 and 3 is shown. The average safety within these circles are 97.82% for spot 1 and 94.59% for spot 3 (although spot 3 was found for solar arrays at 10 m above ground).

8 Discussion and future work

During the course of this work various insights have been gained and are discussed in detail here. The motivation for this study was to identify and precisely map landing sites located near the lunar south pole owing to the fact that this region will most probably be the next target area for future lunar missions. Apart from the scientific goals and constraints of such a mission, the key requirements for the characterization of a south polar landing site were identified to be topography, slopes, illumination, roughness and communication to Earth. Another important aspect is the expected temperature of the lander/rover and the lunar soil at the landing site. This aspect was not covered here but precise surface temperature maps can, for instance, be derived from results of the simulation of illumination conditions as shown in this work. This analysis is subject to future work. Also, results from LRO's DIVINER instrument [Paige and Greenhagen, 2013] could additionally be consulted to conduct thermal studies for such a mission.

The derivation of high-resolution topography from LOLA tracks showed expected inconsistencies, which needed to be clarified. A new approach to identify and adjust displaced LOLA tracks was developed. The derived co-registration algorithm can be applied to various problems and is already used by other groups, e.g. by Stark et al. [2012] to determine the physical librations of Mercury. A 200 x 200 km south polar DTM with 20 m/pixel was successfully derived using this method.

Based on this DTM, illumination conditions are determined for the south polar region and various landing sites have been identified. Although these landing sites have previously been identified and investigated by other authors, the results presented in this work are novel. The quality of the DTM used in this analysis supersedes all previous studies, not only due to the applied adjustment but also due to the steadily growing and improving LOLA data set. Secondly, a DTM with a resolution improved by a factor of 2 to 12 times of previous DTMs was used in this study, which lead to significantly different results. Maximum illuminated spots on the lunar surface were sometimes found kilometers apart from the ones found in previous studies. This work also provides more accurate maximum illumination results that accounts for a 10% difference with previous findings. Although different findings in terms of identified maximum illuminated locations and illumination levels existed prior to this study, the cause for these variations was not identified and described in literature. The root of the problem was found in the representation of the close-range topography, and therefore, is directly dependent on the resolution of the DTM. Future work should heavily concentrate on the resolution and quality of the topography in the near-field.

This study has also uniquely contributed to the determination of periods of a direct line-of-sight from the south polar region to ten ESA tracking stations. Detailed work on the visibility of distinct tracking stations on Earth as seen from an observer near the lunar south pole could not be found in the literature and is a novel finding. The periods of communication links from a potential landing site at the lunar south pole can be widely

improved by installing or having access to at least two more stations in the southern hemisphere, preferably in the pacific ocean between Australia and South America and one in South Africa. When the lunar south pole is below the ecliptic, no communication link is feasible due to the orbit geometry. A detailed study on a possible lunar radio station located on the nearside of the Moon, as suggested by Mazarico et al. [2011a], establishing a permanent radio link to the landing site and to Earth is subject of future work.

A minor contribution of this study is the derivation of slope and surface roughness maps. Although the derivation of such data products is explained and results are shown, they were primarily used to constrain the landing site area and less time was spent on the interpretation. Extensive work on this topic was carried out on a global level by various authors (e.g. [Kreslavsky et al., 2013; Rosenburg et al., 2011]), but future work should concentrate on specific sites and try to connect surface roughness derived by laser pulse width with rock statistics derived from surface images like those obtained by NAC.

9 Abbreviations

APD	Avalanche Photodiode
ASU	Arizona State University
CCD	Charged-Coupled Device
CLTM-s01	Chang'E-1 Lunar Topography Model s01
CO	Commissioning Orbit
COM	Center of Mass
CPR	Circular Polarization Ratio
CRaTER	Cosmic Ray Telescope for the Effects of Radiation
CTX	Context Camera
DLR	Deutsches Zentrum für Luft- und Raumfahrt
DLRE	Diviner Lunar Radiometer Experiment
DOE	Diffractive Optical Element
DTM	Digital Terrain Model
EDR	Experiment Data Record
ESA	European Space Agency
ESM1	First Extended Science Mission
ESM2	Second Extended Science Mission
EVA	Extra-Vehicular Activity
FDF	Flight Dynamics Facility
FoV	Field of View
GDR	Gridded Data Record
GLXP	Google Lunar X Prize
GMT	Generic Mapping Tool
GSFC	Goddard Space Flight Center
HGA	High Gain Antenna
HiRISE	High Resolution Imaging Science Experiment

HRSC	High Resolution Stereo Camera
IAA RAS	Institute for Applied Astronomy of the Russian Academy of Sciences
IFoV	Instantaneous Field Of View
ILN	International Lunar Network
IMCCE	Institut de Mécanique Céleste et de Calcul des Éphémérides
ISRO	Indian Space Research Organization
JPL	Jet Propulsion Laboratory
LALT	Laser Altimeter
LAM	Laser Altimeter
LAMP	Lyman-Alpha Mapping Project
LEND	Lunar Exploration Neutron Detector
LIDAR	Laser Image Detection and Ranging
LLR	Lunar Laser Ranging
LLRI	Lunar Laser Ranging Instrument
LOI	Lunar Orbit Insertion
LOLA	Lunar Orbiter Laser Altimeter
LPRP	Lunar Precursor Robotic Program
LRO	Lunar Reconnaissance Orbiter
LROC	Lunar Reconnaissance Orbiter Camera
LRO-LR	LRO Laser Ranging
LRO-MOC	LRO Mission Operations Center
LRO-SOC	LRO Science Operations Center
LRV	Lunar Roving Vehicle
ME	Mean Earth/Polar Axis
MER	Mars Exploration Rover
MGS	Mars Global Surveyor
MLI	Multilayer Insulation

MOC	Mars Orbiter Camera
MOLA	Mars Orbiter Laser Altimeter
MSFC	Marshall Space Flight Center
MSL	Mars Science Laboratory
NAC	Narrow Angle Camera
NAIF	Navigation and Ancillary Information Facility
NASA	National Aeronautics and Space Administration
NCC	Normalized Cross Correlation
Nd:YAG	Neodymium-Doped Yttrium Aluminum Garnet
NGSLR	Next Generation Satellite Laser Ranging System
NO	Nominal Exploration Mission
NSSDC	National Space Science Data Center
PA	Principal Axis
PDS	Planetary Data System
POD	Precise Orbit Determination
PSA	Permanently Shadowed Area
RDR	Reduced Data Record
RMS	Root Mean Square
RoI	Region of Interest
ROSCOSMOS	Russian Federal Space Agency
SHADR	Spherical Harmonic Analysis Data Record
SIM	Scientific Instrumentation Module
SM	Science Mission
TMC	Terrain Mapping Camera
TOF	Time Of Flight
USA	United States of America
USN	Universal Space Network

UV	Ultraviolet
VGA	Variable Gain Amplifier
VIS	Visible
WAC	Wide Angle Camera

A Software

GMT In this work the Generic Mapping Tool (GMT) is used to generate maps and plots [Wessel and Smith, 1991]. GMT is an open source program released under the GNU Lesser General Public License[4] and is widespread among the planetary and Earth science community. Consisting of about 80 functions, mainly for manipulating Cartesian and geographic data sets, maps in any common map projection can be produced. Supported by the National Science Foundation[5], Paul Wessel, Walter H. F. Smith, Remko Scharroo, Joaquim Luis and Florian Wobbe developed and maintain GMT.

SPICE NASA's Navigation and Ancillary Information Facility (NAIF) provides a space geometry information system named SPICE [Acton, 1996], giving scientists a powerful tool to derive positions, velocities, orientations, sizes etc. of planetary bodies and spacecraft in a chosen coordinate frame at any given time. It is widespread and appreciated throughout the planetary science community. SPICE helps planning space missions and observations but also in science data analysis of past and current missions. SPICE consists of the SPICE Toolkit software itself and the SPICE data files, referred to as kernels. To derive geometries in space and time for a specific observer or object the appropriate kernels need to be loaded.

The set of kernels consists of:

- Spacecraft Clock kernels (SCLK)
- Leapseconds kernel (LSK)
- Text-style (most) Physical Constants kernels (PCK)
- Instrument parameter kernels (IK)
- Frame definition kernels (FK)
- E-kernels (EK, although EKs are now rarely used)
- Meta-kernels (MK, also called 'furnsh kernels')
- SP-kernels (SPK)
- Binary-style PC-kernels (PCK)
- C-kernels (CK)
- Spacecraft events kernels (EK/ESP)

[4] http://www.gnu.org/licenses/lgpl.html
[5] http://www.nsf.gov/

Fig. 81 shows a typical situation planetary scientists are confronted with and emphasizes the key advantages when using SPICE. The relative geometries, distances and orientations of the illustrated problem can easily be solved using the SPICE Toolkit and data files.

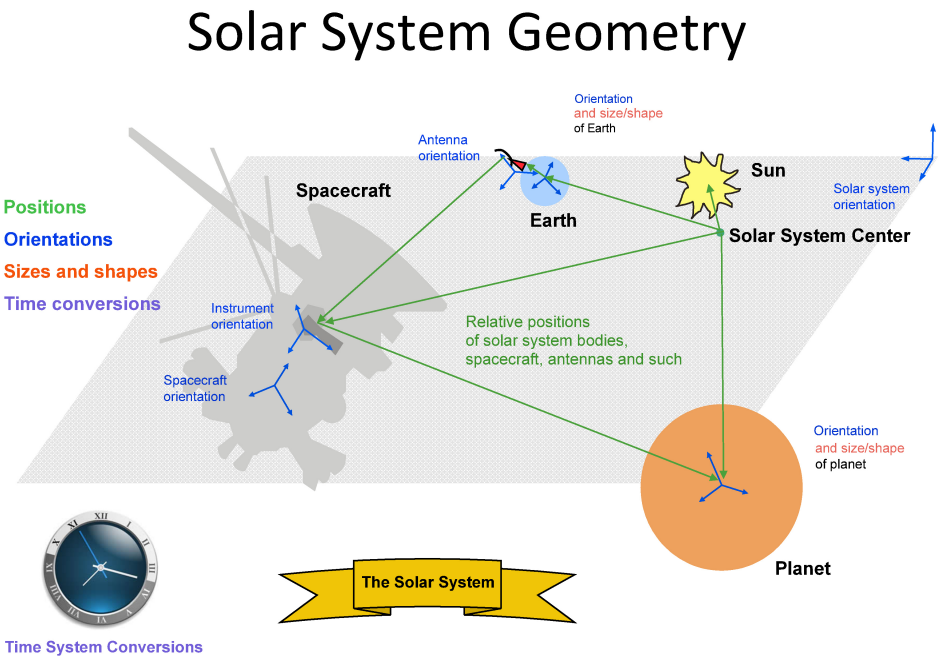

Figure 81: This plot illustrates which quantities can be determined by built-in functions of the SPICE Toolkit, e.g. helping scientist to navigate a spacecraft. ©[NASA/JPL]

B Least-Squares

Here, a more detailed description of the least-squares approach is given, which was introduced in Chapter 6.1. The equations and notation as given in Niemeier [2001] are adopted in the following, where l, L typically describe parameters associated with observations and x, X are associated variables for the unknown parameters. Bold letters represent vectors. Further important notations are:

$\widetilde{L}, \widetilde{X}$:	true values (theoretical)
L^0, X^0 :	initial, approximated values
$\widehat{L}, \widehat{X}$:	estimated values

In the widely-used parametric least-squares approach, each observation can be written as a function of the unknown parameters.

$$\tilde{\boldsymbol{L}} = \boldsymbol{F}(\tilde{\boldsymbol{X}}) \tag{43}$$

In the least-squares approach, however, several observations and unknowns can occur in each equation. The functional model in the least-squares approach is given in Eq. 44, which is true for theoretical values of observations and unknowns. According to the postulation of the least-squares approach, Eq. 44 must also be true for the estimated values, see Eq. 45.

$$\boldsymbol{F}(\tilde{\boldsymbol{L}}, \tilde{\boldsymbol{X}}) = 0 \tag{44}$$

$$\boldsymbol{F}(\hat{\boldsymbol{L}}, \hat{\boldsymbol{X}}) = 0 \tag{45}$$

The functional model as introduced in Chapter 6.1 is

$$\boldsymbol{F}(\boldsymbol{L}, \boldsymbol{X_0}) = \boldsymbol{H} - \boldsymbol{f}(x + \Delta x_0, y + \Delta y_0) - (z + \Delta z_0) = \boldsymbol{0} \tag{46}$$

The vector $\boldsymbol{H}$ contains the laser heights, $\boldsymbol{f}(x + \Delta x_0, y + \Delta y_0)$ is a vector of height values retrieved by the bilinear interpolation of the DTM at the laser position and $z + \Delta z_0$ is the scalar, vertical offset between the two data sets. Eq. 46 describes the difference of a laser height value and the DTM height resulting from a bilinear interpolation corrected for a vertical offset. The bilinear interpolation uses four DTM points surrounding the position of the laser spot, which is exemplarily shown for three laser spots in Fig. 82. The following equations will exemplarily be given for a DTM with nine pixels and a laser track containing three spots (Fig. 82). In general, the number of laser spots is much greater than three, approximately in the range of hundreds to thousands of spots.
Inserting the equation of bilinear interpolation (see Eq. 10) into Eq. 46 and using the nomenclature for the three laser spots and nine DTM pixels as indicated in Fig. 82, yields

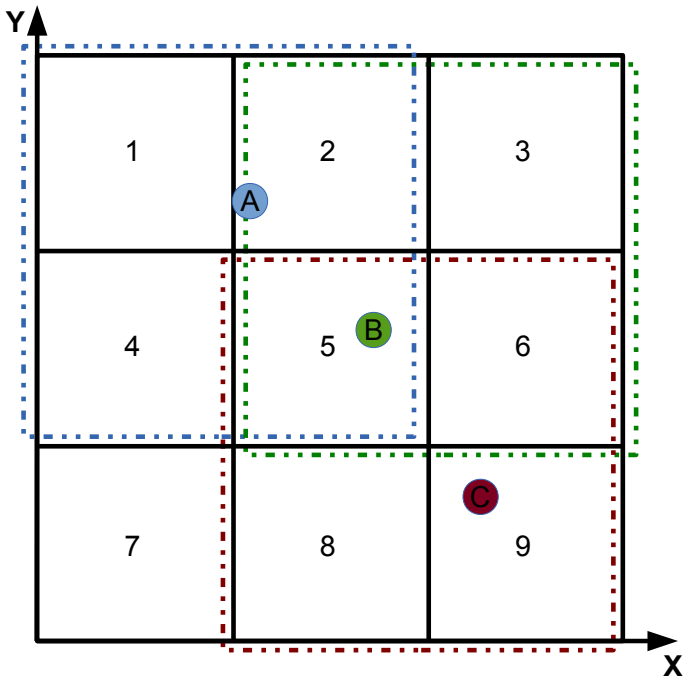

Figure 82: Three laser spots A,B,C on a DTM with nine pixels 1-9. The colored squares surround the four DTM pixels which are used to derive a height value at the laser spot position, displayed in the same color.

the vector of misclosure $\boldsymbol{w}$:

$$\boldsymbol{w} = \boldsymbol{F}(\boldsymbol{L}, \boldsymbol{X_0}) = \begin{pmatrix} h_A - (z + \Delta z_0) - \\ \frac{h_1}{(x_5 - x_4)(y_2 - y_5)}(x_5 - (x_A + \Delta x_0))((y_A + \Delta y_0) - y_5) - \\ \frac{h_2}{(x_5 - x_4)(y_2 - y_5)}((x_A + \Delta x_0) - x_4)((y_A + \Delta y_0) - y_5) - \\ \frac{h_4}{(x_5 - x_4)(y_2 - y_5)}(x_5 - (x_A + \Delta x_0))(y_2 - (y_A + \Delta y_0)) - \\ \frac{h_5}{(x_5 - x_4)(y_2 - y_5)}((x_A + \Delta x_0) - x_4)(y_2 - (y_A + \Delta y_0)) \\ \\ h_B - (z + \Delta z_0) - \\ \frac{h_2}{(x_6 - x_5)(y_3 - y_6)}(x_6 - (x_B + \Delta x_0))((y_B + \Delta y_0) - y_6) - \\ \frac{h_3}{(x_6 - x_5)(y_3 - y_6)}((x_B + \Delta x_0) - x_5)((y_B + \Delta y_0) - y_6) - \\ \frac{h_4}{(x_6 - x_5)(y_3 - y_6)}(x_6 - (x_B + \Delta x_0))(y_3 - (y_B + \Delta y_0)) - \\ \frac{h_6}{(x_6 - x_5)(y_3 - y_6)}((x_B + \Delta x_0) - x_5)(y_3 - (y_B + \Delta y_0)) \\ \\ h_C - (z + \Delta z_0) - \\ \frac{h_5}{(x_9 - x_8)(y_6 - y_9)}(x_9 - (x_C + \Delta x_0))((y_C + \Delta y_0) - y_9) - \\ \frac{h_6}{(x_9 - x_8)(y_6 - y_9)}((x_C + \Delta x_0) - x_8)((y_C + \Delta y_0) - y_9) - \\ \frac{h_8}{(x_9 - x_8)(y_6 - y_9)}(x_9 - (x_C + \Delta x_0))(y_6 - (y_C + \Delta y_0)) - \\ \frac{h_9}{(x_9 - x_8)(y_6 - y_9)}((x_C + \Delta x_0) - x_8)(y_6 - (y_C + \Delta y_0)) - \end{pmatrix} = \mathbf{0} \quad (47)$$

The vector of unknown parameters $\boldsymbol{X^0}$ has three initial values, which are all set to 0 since the positions $(x_{A-C}, y_{A-C}, z_{A-C})$ derived by the grid search algorithm (Chapter 6.1.3) are

close to the final solution.

$$\boldsymbol{X_0} = \begin{pmatrix} \Delta x_0 \\ \Delta y_0 \\ \Delta z_0 \end{pmatrix} = \mathbf{0} \tag{48}$$

The Taylor expansion of Eq. 45 yields to

$$\boldsymbol{F}(\hat{\boldsymbol{L}}, \hat{\boldsymbol{X}}) = \boldsymbol{F}(\boldsymbol{L}, \boldsymbol{X^0}) + \frac{\partial \boldsymbol{F}(\boldsymbol{L}, \boldsymbol{X^0})}{\partial \boldsymbol{L}}(\hat{\boldsymbol{L}} - \boldsymbol{L}) + \frac{\partial \boldsymbol{F}(\boldsymbol{L}, \boldsymbol{X^0})}{\partial \boldsymbol{X^0}}(\hat{\boldsymbol{X}} - \boldsymbol{X^0}) = \mathbf{0} \tag{49}$$

The partial derivatives of the functional model to the observations are summarized in the design matrix $\boldsymbol{B}$

$$\boldsymbol{B} = \frac{\partial \boldsymbol{F}(\boldsymbol{L}, \boldsymbol{X^0})}{\partial \boldsymbol{L}} = \tag{50}$$

$$\begin{array}{c} \\ A \\ B \\ C \end{array} \begin{array}{c} \begin{array}{ccccccccccc} \frac{\partial \boldsymbol{F_i}}{\partial h_A} & \frac{\partial \boldsymbol{F_i}}{\partial h_B} & \frac{\partial \boldsymbol{F}}{\partial h_C} & \frac{\partial \boldsymbol{F_i}}{\partial h_1} & \frac{\partial \boldsymbol{F_i}}{\partial h_2} & \frac{\partial \boldsymbol{F_i}}{\partial h_3} & \frac{\partial \boldsymbol{F_i}}{\partial h_4} & \frac{\partial \boldsymbol{F_i}}{\partial h_5} & \frac{\partial \boldsymbol{F_i}}{\partial h_6} & \frac{\partial \boldsymbol{F_i}}{\partial h_8} & \frac{\partial \boldsymbol{F_i}}{\partial h_9} \end{array} \\ \begin{pmatrix} 1 & 0 & 0 & \boldsymbol{B_{1,4}} & \boldsymbol{B_{1,5}} & 0 & \boldsymbol{B_{1,7}} & \boldsymbol{B_{1,8}} & 0 & 0 & 0 \\ 0 & 1 & 0 & 0 & \boldsymbol{B_{2,5}} & \boldsymbol{B_{2,6}} & 0 & \boldsymbol{B_{2,8}} & \boldsymbol{B_{2,9}} & 0 & 0 \\ 0 & 0 & 1 & 0 & 0 & 0 & 0 & \boldsymbol{B_{3,8}} & \boldsymbol{B_{3,9}} & \boldsymbol{B_{3,10}} & \boldsymbol{B_{3,11}} \end{pmatrix} \end{array}$$

with

$$\begin{aligned}
\boldsymbol{B_{1,4}} &= -\frac{(x_5 - (x_A + \Delta x_0))((y_A + \Delta y_0) - y_5)}{(x_5 - x_4)(y_2 - y_5)} \\
\boldsymbol{B_{1,5}} &= -\frac{((x_A + \Delta x_0) - x_4)((y_A + \Delta y_0) - y_5)}{(x_5 - x_4)(y_2 - y_5)} \\
\boldsymbol{B_{1,7}} &= -\frac{(x_5 - (x_A + \Delta x_0))(y_2 - (y_A + \Delta y_0))}{(x_5 - x_4)(y_2 - y_5)} \\
\boldsymbol{B_{1,8}} &= -\frac{((x_A + \Delta x_0) - x_4)(y_2 - (y_A + \Delta y_0))}{(x_5 - x_4)(y_2 - y_5)} \\
\boldsymbol{B_{2,5}} &= -\frac{(x_6 - (x_B + \Delta x_0))((y_B + \Delta y_0) - y_6)}{(x_6 - x_5)(y_3 - y_6)} \\
\boldsymbol{B_{2,6}} &= -\frac{((x_B + \Delta x_0) - x_5)((y_B + \Delta y_0) - y_6)}{(x_6 - x_5)(y_3 - y_6)} \\
\boldsymbol{B_{2,8}} &= -\frac{(x_6 - (x_B + \Delta x_0))(y_3 - (y_B + \Delta y_0))}{(x_6 - x_5)(y_3 - y_6)} \\
\boldsymbol{B_{2,9}} &= -\frac{((x_B + \Delta x_0) - x_5)(y_3 - (y_B + \Delta y_0))}{(x_6 - x_5)(y_3 - y_6)} \\
\boldsymbol{B_{3,8}} &= -\frac{(x_9 - (x_C + \Delta x_0))((y_C + \Delta y_0) - y_9)}{(x_9 - x_8)(y_6 - y_9)} \\
\boldsymbol{B_{3,9}} &= -\frac{((x_C + \Delta x_0) - x_8)((y_C + \Delta y_0) - y_9)}{(x_9 - x_8)(y_6 - y_9)} \\
\boldsymbol{B_{3,10}} &= -\frac{(x_9 - (x_C + \Delta x_0))(y_6 - (y_C + \Delta y_0))}{(x_9 - x_8)(y_6 - y_9)} \\
\boldsymbol{B_{3,11}} &= -\frac{((x_C + \Delta x_0) - x_8)(y_6 - (y_C + \Delta y_0))}{(x_9 - x_8)(y_6 - y_9)}
\end{aligned}$$

Note, that in the given example the DTM pixel marked with number 7 (Fig. 82) does not occur in Eq. 50 since it is never used in the bilinear interpolation. On the other hand, a DTM pixel can be used several times in the bilinear interpolation for different laser spots, e.g. DTM pixel number 5 is used for every interpolation. This circumstance introduces correlations and heavily complicates the initialization of the matrix due to the fact that the size of the matrix is unknown at the time of creation and cannot be inferred from the number of laser points. However, if laser points are sparse and widely spread over the DTM or the DTM pixel size is much smaller than the distance of two successive laser spots, then four different DTM points are used for each laser spot position. In the case of LOLA and NAC DTMs, no correlations occur because the typical DTM resolution of 2 m per pixel is much smaller than the distance of two successive LOLA spots (10-12 m). Here, the number of columns of matrix $\boldsymbol{B}$ can be calculated by the simple relation $n+4n$, where n is the number of observations, here laser spots on the DTM.
Design matrix $\boldsymbol{A}$ contains the partial derivatives of the functional model to the unknown parameters

$$\boldsymbol{A} = \frac{\partial \boldsymbol{F}(\boldsymbol{L}, \boldsymbol{X^0})}{\partial \boldsymbol{X^0}} = \begin{array}{c} \\ A \\ B \\ C \end{array} \begin{array}{c} \begin{array}{ccc} \frac{\partial \boldsymbol{F_i}}{\partial \Delta x_0} & \frac{\partial \boldsymbol{F_i}}{\partial \Delta y_0} & \frac{\partial \boldsymbol{F}}{\partial \Delta z_0} \end{array} \\ \begin{pmatrix} \boldsymbol{A_{1,1}} & \boldsymbol{A_{1,2}} & -1 \\ \boldsymbol{A_{2,1}} & \boldsymbol{A_{2,2}} & -1 \\ \boldsymbol{A_{3,1}} & \boldsymbol{A_{3,2}} & -1 \end{pmatrix} \end{array} \tag{51}$$

with

$$\begin{aligned}
\boldsymbol{A_{1,1}} &= \frac{((y_A + \Delta y_0) - y_5)(h_1 - h_2) + (y_2 - (y_A + \Delta y_0))(h_4 - h_5)}{(x_5 - x_4)(y_2 - y_5)} \\
\boldsymbol{A_{1,2}} &= \frac{(x_5 - (x_A + \Delta x_0))(h_4 - h_1) + ((x_A + \Delta x_0) - x_4)(h_5 - h_2)}{(x_5 - x_4)(y_2 - y_5)} \\
\boldsymbol{A_{2,1}} &= \frac{((y_B + \Delta y_0) - y_6)(h_2 - h_3) + (y_3 - (y_B + \Delta y_0))(h_5 - h_6)}{(x_6 - x_5)(y_3 - y_6)} \\
\boldsymbol{A_{2,2}} &= \frac{(x_6 - (x_B + \Delta x_0))(h_5 - h_2) + ((x_B + \Delta x_0) - x_5)(h_6 - h_3)}{(x_6 - x_5)(y_3 - y_6)} \\
\boldsymbol{A_{3,1}} &= \frac{((y_C + \Delta y_0) - y_9)(h_5 - h_6) + (y_6 - (y_C + \Delta y_0))(h_8 - h_9)}{(x_9 - x_8)(y_6 - y_9)} \\
\boldsymbol{A_{3,2}} &= \frac{(x_9 - (x_C + \Delta x_0))(h_8 - h_5) + ((x_C + \Delta x_0) - x_8)(h_9 - h_6)}{(x_9 - x_8)(y_6 - y_9)}
\end{aligned}$$

The size of matrix $\boldsymbol{A}$ is known prior to the creation, its dimensions are $n \cdot u$ with n being the number of observations (here three laser spots) and u being the number of unknown parameters, which is always 3 (Eq. 48). Rewriting Eq. 46 with $\boldsymbol{A}, \boldsymbol{B}, \boldsymbol{w}$ and introducing $\boldsymbol{v} = \hat{\boldsymbol{L}} - \boldsymbol{L}$, $\hat{\boldsymbol{x}} = \hat{\boldsymbol{X}} - \boldsymbol{X^0}$ leads to

$$\boldsymbol{B}\boldsymbol{v} + \boldsymbol{A}\hat{\boldsymbol{x}} + \boldsymbol{w} = 0 \tag{52}$$

The variance covariance matrix of the observations, $\boldsymbol{\Sigma_{ll}}$, is composed by the product of the a priori variance factor σ_0^2 (here $\sigma_0 = 1$) and the cofactor matrix $\boldsymbol{Q_{ll}}$. $\boldsymbol{\Sigma_{ll}}$ contains the squares of the standard deviations of the observations. Although the values for the standard deviations for LOLA and NAC are known, the dimension of $\boldsymbol{\Sigma_{ll}}$ depends on the correlations as described for the $\boldsymbol{B}$-matrix. In this particular example the $\boldsymbol{\Sigma_{ll}}$-matrix is

$$\boldsymbol{\Sigma_{ll}} = \begin{pmatrix} \sigma_A^2 & & & & & & & & & \\ & \sigma_B^2 & & & & & & & & \\ & & \sigma_C^2 & & & & & & & \\ & & & \sigma_1^2 & & & & & & \\ & & & & \sigma_2^2 & & & & & \\ & & & & & \sigma_3^2 & & & & \\ & & & & & & \sigma_4^2 & & & \\ & & & & & & & \sigma_5^2 & & \\ & & & & & & & & \sigma_6^2 & \\ & & & & & & & & & \sigma_8^2 \\ & & & & & & & & & & \sigma_9^2 \end{pmatrix} \tag{53}$$

Typically a σ_{LOLA} =10 cm and σ_{NAC} =30 cm is used.
The normal equations are (with $\boldsymbol{k}$ being the Lagrangian multipliers)

$$\begin{pmatrix} \boldsymbol{BQ_{ll}B^T} & \boldsymbol{A} \\ \boldsymbol{A^T} & \boldsymbol{0} \end{pmatrix} \cdot \begin{pmatrix} \boldsymbol{k} \\ \hat{\boldsymbol{x}} \end{pmatrix} = \begin{pmatrix} \boldsymbol{-w} \\ \boldsymbol{0} \end{pmatrix} \tag{54}$$

which lead to the solution

$$\hat{\boldsymbol{x}} = -(-(\boldsymbol{BQ_{ll}B^T})^{-1}\boldsymbol{A}(-(\boldsymbol{A^T}(\boldsymbol{BQ_{ll}B^T})^{-1}\boldsymbol{A})^{-1})^T\boldsymbol{w} \tag{55}$$

The vector of the adjusted unknown paramters is $\hat{\boldsymbol{X}} = \boldsymbol{X^0} + \hat{\boldsymbol{x}}$.
The cofactor matrix of the adjusted unknown parameters, $\boldsymbol{Q_{\hat{x}\hat{x}}}$ reads as

$$\boldsymbol{Q_{\hat{x}\hat{x}}} = (\boldsymbol{A^T}(\boldsymbol{BQ_{ll}B^T})^{-1}\boldsymbol{A})^{-1} \tag{56}$$

The standard deviations of the found translational shift are on the diagonal of the variance covariance matrix of the adjusted unknowns $\boldsymbol{S_{\hat{x}\hat{x}}}$

$$\boldsymbol{S_{\hat{x}\hat{x}}} = s_0^2\boldsymbol{Q_{\hat{x}\hat{x}}} \tag{57}$$

$$s_0 = \sqrt{\frac{\boldsymbol{v^T Q_{ll}^{-1} v}}{n-u}} \tag{58}$$

$$\boldsymbol{v} = \boldsymbol{Q_{ll}B^T k} \tag{59}$$

Note, that in our minimal example $n - u = 0$ since adjustment is only feasible when the number of observations exceed the number of unknown parameters.
In this work, a convergence limit of 1/10th of a DTM pixel was defined, meaning the norm of the vector of the adjusted unknown parameters must be smaller than 1/10th of a DTM pixel, $\|\hat{\boldsymbol{x}}\| < 0.1 \cdot pixelsize$. If the adjusted unknown parameters are within this limit the final solution was found, otherwise the process is iterated with the calculated adjusted unknown parameters until the convergence limit is reached.

References

Abshire, J. B., Sun, X., and Afzal, R. S. (2000). Mars Orbiter Laser Altimeter: Receiver Model and Performance Analysis. *Applied Optics*, 39:2449–2460.

Acton, C. H. (1996). Ancillary data services of NASA's Navigation and Ancillary Information Facility. *Planetary and Space Science*, 44:65–70.

Araki, H., Tazawa, S., Noda, H., Ishihara, Y., Goossens, S., Kawano, N., Sasaki, S., Kamiya, I., Otake, H., Oberst, J., and Shum, C. K. (2009). The Lunar Global Topography by the Laser Altimeter (LALT) Onboard Kaguya (SELENE): Results from the One Year Observation. In *Lunar and Planetary Institute Science Conference Abstracts*, volume 40 of *Lunar and Planetary Institute Science Conference Abstracts*, page 1432.

Bae, S. and Schutz, B. (2002). ICESAT/GLAS Laser Pointing Determination. *Advances In The Astronautical Sciences*, 112:359–370.

Bauch, K. E. and Hiesinger, H. (2012). Rock Concentration and Thermal Inertia of Selected Lunar Study Regions. In Abbasi, A. and Giesen, N., editors, *EGU General Assembly Conference Abstracts*, volume 14 of *EGU General Assembly Conference Abstracts*, page 12540.

Bell, J. F., Malin, M. C., Caplinger, M. A., Ravine, M. A., Godber, A. S., Jungers, M. C., Rice, M. S., and Anderson, R. B. (2012). Mastcam Multispectral Imaging on the Mars Science Laboratory Rover: Wavelength Coverage and Imaging Strategies at the Gale Crater Field Site. In *Lunar and Planetary Science Conference*, volume 43 of *Lunar and Planetary Science Conference*, page 2541.

Bills, B. G. and Ferrari, A. J. (1977). A harmonic analysis of lunar topography. *Icarus*, 31:244–259.

Bussey, D. B. J., McGovern, J. A., Spudis, P. D., Neish, C. D., Noda, H., Ishihara, Y., and Sørensen, S.-A. (2010). Illumination conditions of the south pole of the Moon derived using Kaguya topography. *Icarus*, 208:558–564.

Bussey, D. B. J., McGovern, J. A., Spudis, P. D., Neish, C. D., and Sörensen, S.-A. (2009). Lunar Polar Illumination Conditions Derived Using Kaguya Laser Data. *LPI Contributions*, 1515:5.

Bussey, D. B. J., Patterson, G. W., Turner, F. S., Schulze, R., Wahl, D. E., Erteza, I., Nolan, M., Jensen, J. R., Yocky, D. A., Stickle, A. M., Carter, L., Jakowatz, C. V., Spudis, P. D., and Mini-RF Team (2014). Bistatic Radar Observations of the Moon Using the Arecibo Observatory and Mini-RF on LRO. In *Lunar and Planetary Science Conference*, volume 45 of *Lunar and Planetary Inst. Technical Report*, page 2704.

Bussey, D. B. J., Robinson, M. S., and Spudis, P. D. (1999). Illumination Conditions at the Lunar Poles. In *Lunar and Planetary Institute Science Conference Abstracts*, volume 30 of *Lunar and Planetary Institute Science Conference Abstracts*, page 1731.

Calla, O. P. N., Jangid, M., and Mathur, S. (2014). Study of Shackleton Crater: Integration of Monostatic and Bistatic Observation from Mini-RF and Arecibo. In *Lunar and Planetary Science Conference*, volume 45 of *Lunar and Planetary Science Conference*, page 1803.

Carpenter, J. D., Fisackerly, R., De Rosa, D., and Houdou, B. (2012). Scientific preparations for lunar exploration with the European Lunar Lander. *Planetary and Space Science*, 74:208–223.

Chakraborty, S. (2011). The co-alignment of planetary laser altimeters and their use for surface roughness investigations. *Inauguraldissertation der Philosophisch-naturwissenschaftlichen Fakultät der Universität Bern*.

Chin, G., Brylow, S., Foote, M., Garvin, J., Kasper, J., Keller, J., Litvak, M., Mitrofanov, I., Paige, D., Raney, K., Robinson, M., Sanin, A., Smith, D., Spence, H., Spudis, P., Stern, S. A., and Zuber, M. (2007). Lunar Reconnaissance Orbiter Overview: The Instrument Suite and Mission. *Space Science Reviews*, 129:391–419.

Colombo, G. (1966). Cassini's Second and Third Laws. *SAO Special Report*, 203.

Cox, A. N. (2000). Book Review: Allen's astrophysical quantities. - 4th ed. / Springer, 2000. *Sky and telescope*, 100(1):010000.

De Rosa, D., Bussey, B., Cahill, J. T., Lutz, T., Crawford, I. A., Hackwill, T., van Gasselt, S., Neukum, G., Witte, L., McGovern, A., Grindrod, P. M., and Carpenter, J. D. (2012). Characterisation of potential landing sites for the European Space Agency's Lunar Lander project. *Planetary and Space Science*, 74:224–246.

Di, K., Hu, W., Liu, Y., and Peng, M. (2012). Co-registration of Chang'E-1 stereo images and laser altimeter data with crossover adjustment and image sensor model refinement. *Advances in Space Research*, 50:1615–1628.

Epp, C. and Smith, T. (2007). Autonomous precision landing and hazard detection and avoidance technology (alhat). In *Aerospace Conference, 2007 IEEE*, pages 1–7.

Fa, W. and Cai, Y. (2014). An Explanation of Anomalous Craters over the Lunar Polar Regions in Mini-RF Images Other than Water Ice. In *Lunar and Planetary Science Conference*, volume 45 of *Lunar and Planetary Science Conference*, page 1345.

Fa, W. and Fang, T. (2013). Analysis of High-Frequency Brightness Temperature of Lunar Surface from Chang'e-2 Microwave Radiometer and Investigations of Mean Diurnal Temperature of Regolith Layer. In *Lunar and Planetary Science Conference*, volume 44 of *Lunar and Planetary Science Conference*, page 1472.

Fienga, A., Manche, H., Kuchynka, P., Laskar, J., and Gastineau, M. (2010). Planetary and Lunar ephemerides, INPOP10A. *ArXiv e-prints*.

Folkner, W. M., Williams, J. G., and Boggs, D. H. (2009). The Planetary and Lunar Ephemeris DE 421. *Interplanetary Network Progress Report*, 178:C1.

Folkner, W. M., Williams, J. G., Boggs, D. H., Park, R. S., and Kuchynka, P. (2014). The Planetary and Lunar Ephemerides DE430 and DE431. *Interplanetary Network Progress Report*, 196:C1.

Gardner, C. S. (1982). Target signatures for laser altimeters: an analysis. *Appl. Opt.*, 21(3):448–453.

Garrick-Bethell, I., Nimmo, F., and Wieczorek, M. A. (2010). Structure and Formation of the Lunar Farside Highlands. *Science*, 330:949–.

Gläser, P., Haase, I., Oberst, J., and Neumann, G. A. (2013a). Co-registration of laser altimeter tracks with digital terrain models and applications in planetary science. *Planetary and Space Science*, 89:111–117.

Gläser, P., Haase, I., Scholten, F., and Oberst, J. (2010). Precision Registration of LRO Altimeter Tracks and Stereo Terrain Models - Implications for Surface Slopes and Roughness. In *European Planetary Science Congress 2010, held 20-24 September in Rome, Italy. , p.296*, pages 296–+.

Gläser, P., Scholten, F., Haase, I., Oberst, J., De Rosa, D., Robinson, M. S., Neumann, G. A., Mazarico, E., Smith, D. E., and Zuber, M. T. (2013b). Improvement of Local LOLA DTMs using LROC NAC DTMs - Example for an ESA Lunar Lander Candidate Landing Site. In *Lunar and Planetary Science Conference*, volume 44 of *Lunar and Planetary Inst. Technical Report*, page 1967.

Gläser, P., Scholten, F., Rosa, D. D., Figuera, R. M., Oberst, J., Mazarico, E., Neumann, G., and Robinson, M. (2014). Illumination conditions at the lunar south pole using high resolution digital terrain models from lola. *Icarus*, 243(0):78 – 90.

Golombek, M., Grant, J., Kipp, D., Vasavada, A., Kirk, R., Fergason, R., Bellutta, P., Calef, F., Larsen, K., Katayama, Y., Huertas, A., Beyer, R., Chen, A., Parker, T., Pollard, B., Lee, S., Sun, Y., Hoover, R., Sladek, H., Grotzinger, J., Welch, R., Noe Dobrea, E., Michalski, J., and Watkins, M. (2012). Selection of the Mars Science Laboratory Landing Site. *Space Science Reviews*, 170:641–737.

Golombek, M. P., Grant, J. A., Parker, T. J., Kass, D. M., Crisp, J. A., Squyres, S. W., Haldemann, A. F. C., Adler, M., Lee, W. J., Bridges, N. T., Arvidson, R. E., Carr, M. H., Kirk, R. L., Knocke, P. C., Roncoli, R. B., Weitz, C. M., Schofield, J. T., Zurek, R. W., Christensen, P. R., Fergason, R. L., Anderson, F. S., and Rice, J. W. (2003a). Selection of the Mars Exploration Rover landing sites. *Journal of Geophysical Research (Planets)*, 108:8072.

Golombek, M. P., Haldemann, A. F. C., Forsberg-Taylor, N. K., DiMaggio, E. N., Schroeder, R. D., Jakosky, B. M., Mellon, M. T., and Matijevic, J. R. (2003b). Rock size-frequency distributions on Mars and implications for Mars Exploration Rover landing safety and operations. *Journal of Geophysical Research (Planets)*, 108:8086.

Goswami, J. N. and Annadurai, M. (2009). Chandrayaan-1: India's First Planetary Science Mission to the Moon. In *Lunar and Planetary Institute Science Conference Abstracts*, volume 40 of *Lunar and Planetary Institute Science Conference Abstracts*, page 2571.

Goswami, J. N., Thyagarajan, K., and Annadurai, M. (2006). Chandrayaan-1: Indian Mission to Moon. In S. Mackwell & E. Stansbery, editor, *37th Annual Lunar and Planetary Science Conference*, volume 37 of *Lunar and Planetary Institute Science Conference Abstracts*, page 1704.

Haase, I., Oberst, J., Scholten, F., Wählisch, M., Gläser, P., Karachevtseva, I., and Robinson, M. S. (2012). Mapping the Apollo 17 landing site area based on Lunar Reconnaissance Orbiter Camera images and Apollo surface photography. *Journal of Geophysical Research (Planets)*, 117(16):0.

Hayne, P. O., Aharonson, O., Bandfield, J. L., Greenhagen, B. T., and Paige, D. A. (2012). The Surface Roughness of the Moon from Diviner Infrared Observations. In *Lunar and Planetary Science Conference*, volume 43 of *Lunar and Planetary Inst. Technical Report*, page 2829.

Huang, Q., Ping, J. S., Wieczorek, M. A., Yan, J. G., and Su, X. L. (2010). Improved Global Lunar Topographic Model by Chang'E-1 Laser Altimetry Data. In *Lunar and Planetary Institute Science Conference Abstracts*, volume 41 of *Lunar and Planetary Inst. Technical Report*, page 1265.

Jacobson, S. A., Morbidelli, A., Raymond, S. N., O'Brien, D. P., Walsh, K. J., and Rubie, D. C. (2014). Highly siderophile elements in Earth's mantle as a clock for the Moon-forming impact. *Nature*, 508:84–87.

Johnson, A. E. and Ivanov, T. I. (2011). Analysis and testing of a lidar-based approach to terrain relative navigation for precise lunar landing. In *Proc. AIAA Guidance Navigation and Control Conference (AIAA-GNC 2011)*.

Jutzi, M. and Asphaug, E. (2011). Forming the lunar farside highlands by accretion of a companion moon. *Nature*, 476:69–72.

Kaula, W. M., Schubert, G., Lingenfelter, R. E., Sjogren, W. L., and Wollenhaupt, W. R. (1973). Lunar topography from Apollo 15 and 16 laser altimetry. In *Lunar and Planetary Science Conference Proceedings*, volume 4 of *Lunar and Planetary Science Conference Proceedings*, page 2811.

Kaula, W. M., Schubert, G., Lingenfelter, R. E., Sjogren, W. L., and Wollenhaupt, W. R. (1974). Apollo Laser Altimetry and Inferences as to Lunar Structure. In *Lunar and Planetary Institute Science Conference Abstracts*, volume 5 of *Lunar and Planetary Inst. Technical Report*, page 399.

Keller, J. W., Petro, N. E., McLanahan, T. P., Vondrak, R. R., and Garvin, J. B. (2014). Recent Results from the Lunar Reconnaissance Orbiter Mission and Plans for a Second Extended Science Mission. In *Lunar and Planetary Science Conference*, volume 45 of *Lunar and Planetary Science Conference*, page 2294.

Kim, J., Muller, J.-P., and Morley, J. (2000). Automated MOLA track registration in MOC and VIKING images and it's application for the establishment of new 3-D control points on Mars. *ISPRS Archives - Volume XXXIII Part B4*, 33.

Kolb, K. J. and Okubo, C. H. (2009). Coregistration of Mars Orbiter Laser Altimeter (MOLA) topography with high-resolution Mars images. *Computers and Geosciences*, 35:2304–2313.

Kreslavsky, M. A. and Head, J. W. (2000). Kilometer-scale roughness of Mars: Results from MOLA data analysis. *Journal of Geophysics Research*, 105:26695–26712.

Kreslavsky, M. A., Head, J. W., Neumann, G. A., Rosenburg, M. A., Aharonson, O., Smith, D. E., and Zuber, M. T. (2013). Lunar topographic roughness maps from Lunar Orbiter Laser Altimeter (LOLA) data: Scale dependence and correlation with geologic features and units. *Icarus*, 226:52–66.

Lee, S., Ortiz, G. G., and Alexander, J. W. (2005). Star Tracker-Based Acquisition, Tracking, and Pointing Technology for Deep-Space Optical Communications. *Interplanetary Network Progress Report*, 161:L1.

Lin, S.-Y., Muller, J.-P., Mills, J. P., and Miller, P. E. (2010). An assessment of surface matching for the automated co-registration of MOLA, HRSC and HiRISE DTMs. *Earth and Planetary Science Letters*, 294:520–533.

LRO Project (2008). A Standardized Lunar Coordinate System for the Lunar Reconnaissance orbiter and Lunar Datasets. *LRO Project and LGCWG White Paper*.

Marakushev, A. A. and Chaplygin, O. V. (2002). Origin of the Earth and Moon. In *Lunar and Planetary Institute Science Conference Abstracts*, volume 33 of *Lunar and Planetary Institute Science Conference Abstracts*, pages 1185–+.

Margot, J. L., Campbell, D. B., Jurgens, R. F., and Slade, M. A. (1999). Topography of the Lunar Poles from Radar Interferometry: A Survey of Cold Trap Locations. *Science*, 284:1658.

Mazarico, E., Goossens, S. J., Lemoine, F. G., Neumann, G. A., Torrence, M. H., Rowlands, D. D., Smith, D. E., and Zuber, M. T. (2013). Improved Orbit Determination

of Lunar Orbiters with Lunar Gravity Fields Obtained by the GRAIL Mission. In *Lunar and Planetary Institute Science Conference Abstracts*, volume 44 of *Lunar and Planetary Institute Science Conference Abstracts*, page 2414.

Mazarico, E., Lemoine, F. G., Han, S.-C., and Smith, D. E. (2010). GLGM-3: A degree-150 lunar gravity model from the historical tracking data of NASA Moon orbiters. *Journal of Geophysical Research (Planets)*, 115:5001.

Mazarico, E., Neumann, G. A., Rowlands, D. D., Lemoine, F. G., Smith, D. E., and Zuber, M. T. (2009). Multi-Beam Altimetric Crossovers for the Precision Orbit Determination of the Lunar Reconnaissance Orbiter. In *Lunar and Planetary Science Conference*, volume 40 of *Lunar and Planetary Science Conference*, page 2244.

Mazarico, E., Neumann, G. A., Rowlands, D. D., Smith, D. E., and Zuber, M. T. (2012a). Topography of the Lunar Poles and Application to Geodesy with the Lunar Reconnaissance Orbiter. In *Lunar and Planetary Institute Science Conference Abstracts*, volume 43 of *Lunar and Planetary Institute Science Conference Abstracts*, page 2423.

Mazarico, E., Neumann, G. A., Smith, D. E., Zuber, M. T., and Torrence, M. H. (2011a). Illumination conditions of the lunar polar regions using LOLA topography. *Icarus*, 211:1066–1081.

Mazarico, E., Rowlands, D. D., Neumann, G. A., Smith, D. E., Torrence, M. H., Lemoine, F. G., and Zuber, M. T. (2012b). Orbit determination of the Lunar Reconnaissance Orbiter. *Journal of Geodesy*, 86:193–207.

Mazarico, E., Rowlands, D. D., Neumann, G. A., Torrence, M. H., Smith, D. E., and Zuber, M. T. (2011b). Selenodesy with LRO: Radio Tracking and Altimetric Crossovers to Improve Orbit Knowledge and Gravity Field Estimation. In *Lunar and Planetary Science Conference*, volume 42 of *Lunar and Planetary Science Conference*, page 2215.

Mitrofanov, I., Dolgopolov, V., Khartov, V., Lukjanchikov, A., Tret'yakov, V., and Zelenyi, L. (2014). "Luna-Glob" and "Luna-Resurs": science goals, payload and status. In *EGU General Assembly Conference Abstracts*, volume 16 of *EGU General Assembly Conference Abstracts*, page 6696.

Mitrofanov, I. G., Zelenyi, L. M., Tret'yakov, V. I., and Dolgopolov, V. P. (2011). Science Program of Lunar Landers of "Luna-Glob" and "Luna-Resource" Missions. In *Lunar and Planetary Institute Science Conference Abstracts*, volume 42 of *Lunar and Planetary Institute Science Conference Abstracts*, page 1798.

NASA (2004). The Vision for Space Exploration. *NASA*.

Neumann, G. (2009a). Lunar orbiter laser altimeter raw data set, lro-l-lola-2-edr-v1.0, nasa planetary data system,. Technical report, NASA.

Neumann, G. (2009b). Lunar orbiter laser altimeter raw data set, lro-l-lola-3-rdr-v1.0, nasa planetary data system,. Technical report, NASA.

Neumann, G. (2009c). Lunar orbiter laser altimeter raw data set, lro-l-lola-4-gdr-v1.0, nasa planetary data system,. Technical report, NASA.

Neumann, G. (2009d). Lunar orbiter laser altimeter raw data set, lro-l-lola-5-shadr-v1.0, nasa planetary data system,. Technical report, NASA.

Neumann, G. A., Abshire, J. B., Aharonson, O., Garvin, J. B., Sun, X., and Zuber, M. T. (2003). Mars Orbiter Laser Altimeter pulse width measurements and footprint-scale roughness. *Geophysics Research Letters*, 30(11):1561.

Neumann, G. A., Mazarico, E., Smith, D. E., Zuber, M. T., and Gläser, P. (2011). Lunar Orbiter Laser Altimeter Measures of Slope and Roughness. In *Lunar and Planetary Science Conference*, volume 42 of *Lunar and Planetary Inst. Technical Report*, page 2313.

Neumann, G. A., Smith, D. E., Zuber, M. T., Mazarico, E., Torrence, M. H., Cavanaugh, J. F., and Lola Science Team (2009). Meter-Scale Roughness on the Moon from Lunar Orbiter Laser Altimeter (LOLA) Pulse Spreading: Implications for Exploration. *LPI Contributions*, 1515:47.

Niemeier, W. (2001). *Ausgleichungsrechnung* -. Walter De Gruyter Incorporated, Berlin, New York.

Noda, H., Araki, H., Goossens, S., Ishihara, Y., Matsumoto, K., Tazawa, S., Kawano, N., and Sasaki, S. (2008). Illumination conditions at the lunar polar regions by KAGUYA(SELENE) laser altimeter. *Geophysical Research Letters*, 35:24203.

Oberst, J., Scholten, F., Matz, K.-D., Roatsch, T., Wählisch, M., Haase, I., Gläser, P., Gwinner, K., Robinson, M. S., and Lroc Team (2010). Apollo 17 Landing Site Topography from LROC NAC Stereo Data - First Analysis and Results. In *Lunar and Planetary Institute Science Conference Abstracts*, volume 41 of *Lunar and Planetary Institute Science Conference Abstracts*, pages 2051–+.

Paige, D. A. and Greenhagen, B. T. (2013). Diviner Lunar Radiometer Experiment Extended Mission Results: Thermal, Thermophysical and Compositional Properties. In *Lunar and Planetary Science Conference*, volume 44 of *Lunar and Planetary Science Conference*, page 2492.

Patterson, G. W., Stickle, A. M., Bussey, D. B. J., Cahill, J. T. S., and Mini-RF Team (2014). Mini-RF Observations of the Radar Scattering Properties of Young Lunar Crater Ejecta Blankets. In *Lunar and Planetary Science Conference*, volume 45 of *Lunar and Planetary Inst. Technical Report*, page 2720.

Pavlis, D. E., Poulose S.G., A., and McCarthy, J. J. (2006). Geodyn operations manuals, contractor report. *SGT Inc., Greenbelt, Md.s*.

Peale, S. J. (1969). Generalized Cassini's Laws. *Astronomical Journal*, 74:483.

Ping, J., Huang, Q., Yan, J., Cao, J., Tang, G., and Shu, R. (2009). Lunar topographic model CLTM-s01 from Chang'E-1 laser altimeter. *Science in China G: Physics and Astronomy*, 52:1105–1114.

Pitjeva, E. V. (2010). EPM ephemerides and relativity. In Klioner, S. A., Seidelmann, P. K., and Soffel, M. H., editors, *IAU Symposium*, volume 261 of *IAU Symposium*, pages 170–178.

Preusker, F., Oberst, J., Phillips, J., Watters, T. R., Head, J. W., Zuber, M. T., Turner, F. S., and Solomon, S. C. (2010). Digital Terrain Models of Mercury from MESSENGER Stereo Images. In *Lunar and Planetary Institute Science Conference Abstracts*, volume 41 of *Lunar and Planetary Institute Science Conference Abstracts*, page 1789.

Rambaux, N. and Williams, J. G. (2011). The Moon's physical librations and determination of their free modes. *Celestial Mechanics and Dynamical Astronomy*, 109:85–100.

Riris, H., Cavanaugh, J., and Neumann, G. A. (2010). Calibration Document for the Lunar Orbiter Laser Altimeter (LOLA) Instrument - Revision 2. *NASA*.

Robinson, M. S., Brylow, S. M., Tschimmel, M., Humm, D., Lawrence, S. J., Thomas, P. C., Denevi, B. W., Bowman-Cisneros, E., Zerr, J., Ravine, M. A., Caplinger, M. A., Ghaemi, F. T., Schaffner, J. A., Malin, M. C., Mahanti, P., Bartels, A., Anderson, J., Tran, T. N., Eliason, E. M., McEwen, A. S., Turtle, E., Jolliff, B. L., and Hiesinger, H. (2010). Lunar Reconnaissance Orbiter Camera (LROC) Instrument Overview. *Space Science Reviews*, 150:81–124.

Rosenburg, M. A., Aharonson, O., Head, J. W., Kreslavsky, M. A., Mazarico, E., Neumann, G. A., Smith, D. E., Torrence, M. H., and Zuber, M. T. (2011). Global surface slopes and roughness of the Moon from the Lunar Orbiter Laser Altimeter. *Journal of Geophysical Research (Planets)*, 116:2001.

Roy, A., Wright, J. T., and Sigurðsson, S. (2014). Earthshine on a young moon: Explaining the lunar farside highlands. *The Astrophysical Journal Letters*, 788(2):L42.

Sasaki, S., Goossens, S., Ishihara, Y., Araki, H., Hanada, H., Matsumoto, K., Noda, H., Kikuchi, F., and Iwata, T. (2012). Kaguya Selenodesy and the South Pole Aitken Basin. In *Lunar and Planetary Institute Science Conference Abstracts*, volume 43 of *Lunar and Planetary Institute Science Conference Abstracts*, page 1838.

Schmitt, H. H. (2000). Contrary Views on the Origin and Thermal Evolution of the Moon. In *Lunar and Planetary Institute Science Conference Abstracts*, volume 31 of *Lunar and Planetary Institute Science Conference Abstracts*, pages 1691–+.

Scholten, F., Oberst, J., Matz, K.-D., Roatsch, T., Wählisch, M., Speyerer, E. J., and Robinson, M. S. (2012). GLD100: The near-global lunar 100 m raster DTM from LROC WAC stereo image data. *Journal of Geophysical Research (Planets)*, 117:0.

Seidelmann, P. K., Archinal, B. A., A'Hearn, M. F., Conrad, A., Consolmagno, G. J., Hestroffer, D., Hilton, J. L., Krasinsky, G. A., Neumann, G., Oberst, J., Stooke, P., Tedesco, E. F., Tholen, D. J., Thomas, P. C., and Williams, I. P. (2007). Report of the IAU/IAG Working Group on cartographic coordinates and rotational elements: 2006. *Celestial Mechanics and Dynamical Astronomy*, 98:155–180.

Shi, X., Willner, K., Oberst, J., Ping, J., and Ye, S. (2012). Working models for the gravitational field of phobos. *Science China Physics, Mechanics and Astronomy*, 55(2):358–364.

Shoemaker, E. M., Robinson, M. S., and Eliason, E. M. (1994). The South Pole Region of the Moon as Seen by Clementine. *Science*, 266:1851–1854.

Smith, D. E. and Zuber, M. T. (1998). The relationship between MOLA northern hemisphere topography and the 6.1-Mbar atmospheric pressure surface of Mars. *Geophysical Research Letters*, 25:4397–4400.

Smith, D. E. and Zuber, M. T. (2000). An Overview of the Topography of Mars from the Mars Orbiter Laser Altimeter (MOLA). In *Second International Conference on Mars Polar Science and Exploration*, page 159.

Smith, D. E., Zuber, M. T., and Albee, A. L. (2000). The Shape and Topography of Mars from the Mars Orbiter Laser Altimeter (MOLA). In *IAU Joint Discussion*, volume 12 of *IAU Joint Discussion*.

Smith, D. E., Zuber, M. T., Jackson, G. B., Cavanaugh, J. F., Neumann, G. A., Riris, H., Sun, X., Zellar, R. S., Coltharp, C., Connelly, J., Katz, R. B., Kleyner, I., Liiva, P., Matuszeski, A., Mazarico, E. M., McGarry, J. F., Novo-Gradac, A.-M., Ott, M. N., Peters, C., Ramos-Izquierdo, L. A., Ramsey, L., Rowlands, D. D., Schmidt, S., Scott, V. S., Shaw, G. B., Smith, J. C., Swinski, J.-P., Torrence, M. H., Unger, G., Yu, A. W., and Zagwodzki, T. W. (2010a). The Lunar Orbiter Laser Altimeter Investigation on the Lunar Reconnaissance Orbiter Mission. *Space Science Reviews*, 150:209–241.

Smith, D. E., Zuber, M. T., Neumann, G. A., and Lemoine, F. G. (1997). Topography of the Moon from the Clementine LIDAR. *Journal of Geophysical Research*, 102:1591.

Smith, D. E., Zuber, M. T., Neumann, G. A., Lemoine, F. G., Mazarico, E., Torrence, M. H., McGarry, J. F., Rowlands, D. D., Head, J. W., Duxbury, T. H., Aharonson, O., Lucey, P. G., Robinson, M. S., Barnouin, O. S., Cavanaugh, J. F., Sun, X., Liiva, P., Mao, D.-d., Smith, J. C., and Bartels, A. E. (2010b). Initial observations from the Lunar Orbiter Laser Altimeter (LOLA). *Geophysics Research Letters*, 371:18204.

Smith, D. E., Zuber, M. T., Neumann, G. A., Mazarico, E., Head, J., Torrence, M. H., and Lola Science Team (2011a). Results from the Lunar Orbiter Laser Altimeter (LOLA): Global, High Resolution Topographic Mapping of the Moon. In *Lunar and Planetary Institute Science Conference Abstracts*, volume 42 of *Lunar and Planetary Institute Science Conference Abstracts*, page 2350.

Smith, D. E., Zuber, M. T., Neumann, G. A., Mazarico, E., Head, J. W., and Lola Science Team (2011b). Surface Roughness and Slopes on the Moon at 5-Meter Scale. *LPI Contributions*, 1646:79.

Smith, D. E., Zuber, M. T., Neumann, G. A., and Mazarico, E. M. (2012). Bi-directional reflectance, surface roughness, and shadowing over the lunar south pole. In *European Planetary Science Congress 2012*, page 720.

Snyder, J. P. (1987). Map Projections: A Working Manual. *Geological Survey (U.S)*.

Speyerer, E. J. and Robinson, M. S. (2013). Persistently illuminated regions at the lunar poles: Ideal sites for future exploration. *Icarus*, 222:122–136.

Spohn, T. (2000). Origin, Structure and Evolution of the Moon. In B. H. Foing & M. Perry, editor, *Exploration and Utilisation of the Moon*, volume 462 of *ESA Special Publication*, pages 359–+.

Stacy, N. J. S., Campbell, D. B., and Ford, P. G. (1997). Arecibo radar mapping of the lunar poles: A search for ice deposits. *Science*, 276:1527–1530.

Stark, A., Oberst, J., Preusker, F., Gwinner, K., Peale, S. J., Margot, J.-L., Zuber, M. T., and Solomon, S. C. (2012). In-Situ Measurement of Mercury's Physical Librations Using Image and Laser Altimeter Data from MESSENGER: General Approach and Sensitivity Analysis. In *Lunar and Planetary Institute Science Conference Abstracts*, volume 43 of *Lunar and Planetary Institute Science Conference Abstracts*, page 1389.

Thomson, B. J., Bussey, D. B. J., Cahill, J. T. S., Neish, C., Patterson, G. W., and Spudis, P. D. (2011). The Interior of Shackleton Crater as Revealed by Mini-RF Orbital Radar. In *Lunar and Planetary Science Conference*, volume 42 of *Lunar and Planetary Science Conference*, page 1626.

Thomson, B. J., Bussey, D. B. J., Neish, C. D., Cahill, J. T. S., Heggy, E., Kirk, R. L., Patterson, G. W., Raney, R. K., Spudis, P. D., Thompson, T. W., and Ustinov, E. A. (2012). An upper limit for ice in Shackleton crater as revealed by LRO Mini-RF orbital radar. *Geophysical Research Letters*, 39:14201.

Tooley, C. R., Houghton, M. B., Saylor, R. S., Peddie, C., Everett, D. F., Baker, C. L., and Safdie, K. N. (2010). Lunar Reconnaissance Orbiter Mission and Spacecraft Design. *Space Science Reviews*, 150:23–62.

U. S. Naval Observatory and Royal Greenwich Observatory (2000). *The Astronomical Almanac for the year 2001*. U. S. Naval Observatory & Royal Greenwich Observatory.

Vondrak, R., Keller, J., Chin, G., and Garvin, J. (2010). Lunar Reconnaissance Orbiter (LRO): Observations for Lunar Exploration and Science. *Space Science Reviews*, 150:7–22.

Watson, K., Murray, B., and Brown, H. (1961). On the Possible Presence of Ice on the Moon. *Journal of Geophysical Research*, 66:1598–1600.

Wessel, P. and Smith, W. H. F. (1991). Free software helps map and display data. *Eos, Transactions American Geophysical Union*, 72(41):441–446.

Williams, J., Boggs, D., and Folkner, W. (2008). DE421 Lunar Orbit, Physical Librations, and Surface Coordinates. *JPL Memorandum IOM 335-JW,DB,WF-20080314-001*.

Williams, J. G., Boggs, D. H., and Ratcliff, J. T. (2013). Lunar Science from Lunar Laser Ranging. In *Lunar and Planetary Science Conference*, volume 44 of *Lunar and Planetary Science Conference*, page 2377.

Williams, J. G., Konopliv, A. S., Boggs, D. H., Park, R. S., Yuan, D.-N., Lemoine, F. G., Goossens, S., Mazarico, E., Nimmo, F., Weber, R. C., Asmar, S. W., Melosh, H. J., Neumann, G. A., Phillips, R. J., Smith, D. E., Solomon, S. C., Watkins, M. M., Wieczorek, M. A., Andrews-Hanna, J. C., Head, J. W., Kiefer, W. S., Matsuyama, I., McGovern, P. J., Taylor, G. J., and Zuber, M. T. (2014). Lunar interior properties from the GRAIL mission. *Journal of Geophysical Research (Planets)*, 119:1546–1578.

Winn, J. N. and Holman, M. J. (2005). Obliquity Tides on Hot Jupiters. *The Astrophysical Journal*, 628:L159–L162.

Yoon, J.-S. and Shan, J. (2005). Combined adjustment of moc stereo imagery and mola altimetry data, photogrammetric engineering and remote. *Sensing*, pages 1179–1186.

Zuber, M. T., Smith, D. E., Lehman, D. H., Hoffman, T. L., Asmar, S. W., and Watkins, M. M. (2013). Gravity Recovery and Interior Laboratory (GRAIL): Mapping the Lunar Interior from Crust to Core. *Space Science Reviews*, 178:3–24.